TOWARD RELIABLE IMPLANTABLE DEVICES: ADDRESSING BIOTIC AND ABIOTIC FAILURE MODES IN MICROSCALE MEDICAL DEVICES

by

Hyunsu Park

A Dissertation

Submitted to the Faculty of Purdue University

In Partial Fulfillment of the Requirements for the degree of

Doctor of Philosophy

Weldon School of Biomedical Engineering

West Lafayette, Indiana

May 2020

THE PURDUE UNIVERSITY GRADUATE SCHOOL
STATEMENT OF COMMITTEE APPROVAL

Dr. Hyowon Lee, Chair
Weldon School of Biomedical Engineering

Dr. Pedro Irazoqui
Weldon School of Biomedical Engineering

Dr. Chi Hwan Lee
Weldon School of Biomedical Engineering

Dr. Arezoo Motavalizadeh Ardekani
School of Mechanical Engineering

Approved by:
Dr. Andrew O. Brightman

To my loving wife and son for always leaving the light on for me.

ACKNOWLEDGMENTS

First and foremost, I would like to thank my advisor, Dr. Hyowon Lee, for always supporting me to be the best and for showing me what it takes to be a successful engineer. He is an excellent mentor, and his enthusiasm for research is truly contagious. I am grateful to have him as an advisor and mentor.

I would like to extend my thanks to my colleagues in the Laboratory of Implantable Microsystems Research: Qi Yang, Tran Nguyen, Jongcheon Lim, Jim Nolan, Angel Enriquez, Haesoo Moon, Michael MacLean, Dr. Jian Xu, and Dr. Jinjia Xu. Special appreciation goes to my friend and lab mate Tran Nguyen who has shared with me the entire experience of graduate school, and who has encouraged me at every step. I would also like to say thanks to Jim Nolan and Angel Enriquez for their useful help and constructive suggestions of my research. Discussion with Jongcheon Lim helped me shape the research on the neurostimulation devices. I also would like to thank my committee members for taking the time to understand and appreciate my research. I give special thanks to Dr. Simon John in the Jackson Laboratory, who provided insights into my glaucoma drainage device research. It was so memorable work with talented young undergrads, Haritha Ramadorai, Yong Gyun Cho, Amanda Maples during the SURF program in the summer.

I want to thank to Dr. Yi Xuan and Dr. Joon Hyeong Park for providing me with useful MEMS fab recipes. Many thanks to Amanda Maples for her electrochemical characterizations of my samples. I would also like to thank Shengjiao Zhang for her monolayer graphene transfer to fabricate anti-corrosion neurostimulation electrodes. Research work of Dr. Zhihong Chen and Dr. Luis Solorio also provided insights into my research.

I am grateful to my parents for their constant support of my decisions, and always encouraging me to pursue the best during my life. My deepest gratitude goes to my wife, Dr. Jihye

Park, for her unconditional love and support. Although separated by a long distance for last 5 years, her understanding has always been my firmest backbone giving me faith to proceed on and eventually fulfill the Ph.D. degree. Finally, I would like to thank my son, Taejune Park, who always cheers me up by his smile.

Thank you everyone who has given me helps in this doctoral journey. This thesis would not have been possible without your support.

TABLE OF CONTENTS

LIST OF TABLES

LIST OF FIGURES

ABSTRACT

Implantable devices are widely used for a large number of sensing and stimulating applications. However, majority of implantable devices are faced with reliability issues that limit their long-term usability. For example, in implantable glaucoma drainage devices (GDD) that remove excess aqueous humor (AH) from the anterior chamber, the microscale channel of GDDs often gets obstructed due to biofouling and requires additional surgical intervention. Moreover, Platinum (Pt)-based microscale neurostimulation electrodes often corrode during its usage due to irreversible electrochemical reactions, which can diminish their long-term charge-injection performance and damage the surrounding neural substrate. In this work, I will demonstrate methods to mitigate these major challenges of biotic and abiotic nature towards highly reliable and superior implantable transducers. As a proof-of-concept, I will share our latest attempts to develop a smart "self-clearing" GDD by integrating magnetically-powered microactuators inside the drainage tube of GDD to combat biological occlusions. The magnetic microactuators can be controlled using externally applied magnetic fields to mechanically clear biofouling-based obstruction, thereby eliminating the need for additional surgical intervention. I will show that the microactuators are effective in removing proteinaceous film deposited on device surface as well as on the inner surface of the microchannel, which supports our hypothesis that a smart self-clearing GDD may be possible. As a second example, I will demonstrate that a monolayer of graphene can be used to virtually suppress Pt dissolution while maintaining excellent electrochemical functionality. The results of our work to date suggest that graphene can serve as an excellent diffusion barrier that can ameliorate the concerns for Pt dissolution in chronically implanted neurostimulation microelectrodes. In the future, I plan to evaluate the performance of our devices *in vivo* to demonstrate that our smart self-clearing GDD and graphene-coated Pt microelectrodes can be chronically and reliably implanted while maintaining their superior functional performance.

1. INTRODUCTION

1.1 Implantable Devices

An implantable device is defined as a device or tissue, which is intended to be partially or completely inserted into the human body and remain after the procedure. Implantable devices have been developed for treating variety of diseases, replacing damaged or missing biological structures. As early as 4,000 years ago, ancient Egyptians and Romans used linen for sutures, iron and gold as dental implants, and wood for toe replacement [1]. In the past six decades, the number of advanced implantable medical devices exploded with a series of significant developments including the first implantable cardiac pacemaker developed in 1952 [2]. Although the first implantable pacemaker was made possible with the development transistors, it was not clinically successful due to low battery life that only lasted for less than 3 h. The designing of implantable devices is driven by three main participants: the patient, the medical staff, and the engineer. The development of the implantable medical devices is highly affected by the demands of patients, the preferences of medical doctors, and the technical feasibility of the device determined by the engineer. The development of the implantable medical devices requires an abundant amount of information gathered from mathematical simulations, benchtop testing, manufacturability, and animal and clinical studies.

With advancements in microelectronics, batteries, and biomaterials, there are currently many different implantable biomedical devices in clinical use. Advanced implantable devices such as the implantable cardiac defibrillator, cochlear implant, pressure sensors have all become valuable tools to monitor physiological responses or to provide therapy. In recent years, significant efforts have been made to miniaturize the implantable devices to minimize the invasiveness of implants to improve patient recovery and quality of life [3].

The invention and subsequent advancement of microfabrication techniques, specifically in the area of microelectromechanical systems (MEMS) and microfluidics, have allowed engineers to produce well-controlled medical devices that range in size from millimeters to nanometers. Even a cursory review of literature will reveal that there are hundreds of microscale implantable devices being developed all around the world. One of the most commercially successful implants is a miniaturized blood glucose sensor for the management of diabetes mellitus. Now there are

continuous blood glucose-monitoring (CGM) systems that can fully implanted (Eversense, Senseonics, Inc.) [4]. This CGM system utilizes a fluorescent, boronic-acid based glucose indicating polymer to enable more stability over time *in vivo* [5]. Microfabricated capacitance-based pressure sensors have the potential for measuring blood pressure from a small region during studies of cardiovascular physiology. The EndoSensor/CardioMEMS HF system from CardioMEMS is the first FDA approved implantable blood pressure monitoring device for detection of heart failure within the pulmonary artery [6], [7]. Similar capacitance-based pressure sensors have also been developed for intraocular pressure measurements in glaucoma patient [8]. CMOS image sensors could replace damaged photoreceptors in the back of the eye for those that are visually impaired. MEMS piezoresistive shear stress sensors have been developed to detect shear stress at the interface between join implants and the human body to prevent tissue damage by notifying the information to patients.

1.2 Biotic Failures: Biofouling

Biofouling on implantable devices remains a critical issue that can limit the device reliability and functionality. Biofouling refers to the formation of biological layers on the surface of a foreign materials [9]. When an implant is inserted into the body, a conditioning layer composed of lipids and glycoproteins immediately and spontaneously coat the device's surface [10]. The conformation of the layer is dependent on material properties, size, surface chemistry, design, morphology, and degradation of the device. The interaction of adsorbed proteins such as albumin, fibronectin, vitronectin, globulin, and fibrinogen with receptors expressed on inflammatory cells are related to the cellular recognition process and subsequent inflammation [11]. The foreign body response leads to the formation of a dense and collagen-rich capsule around the devices (Fig 1.2) [10]. At the end stage of the foreign body reaction, the implanted device gets covered by a vascular, collagenous fibrous capsule 50 – 200 mm thick [12]. The fibrous wall prevents functional motions of implants and interaction between the device and the surrounding tissues. Depending on the situation, bacteria could adhere to the surface and proliferate into biofilms.

The implantation of synthetic materials used for pacemakers [13], drug delivery platforms [14], hydrocephalus catheters [15], glaucoma implants [16]–[18], and stents [19] all trigger the foreign body response (Fig 1.3). The adhesion of foreign body cells or biofilms leads to

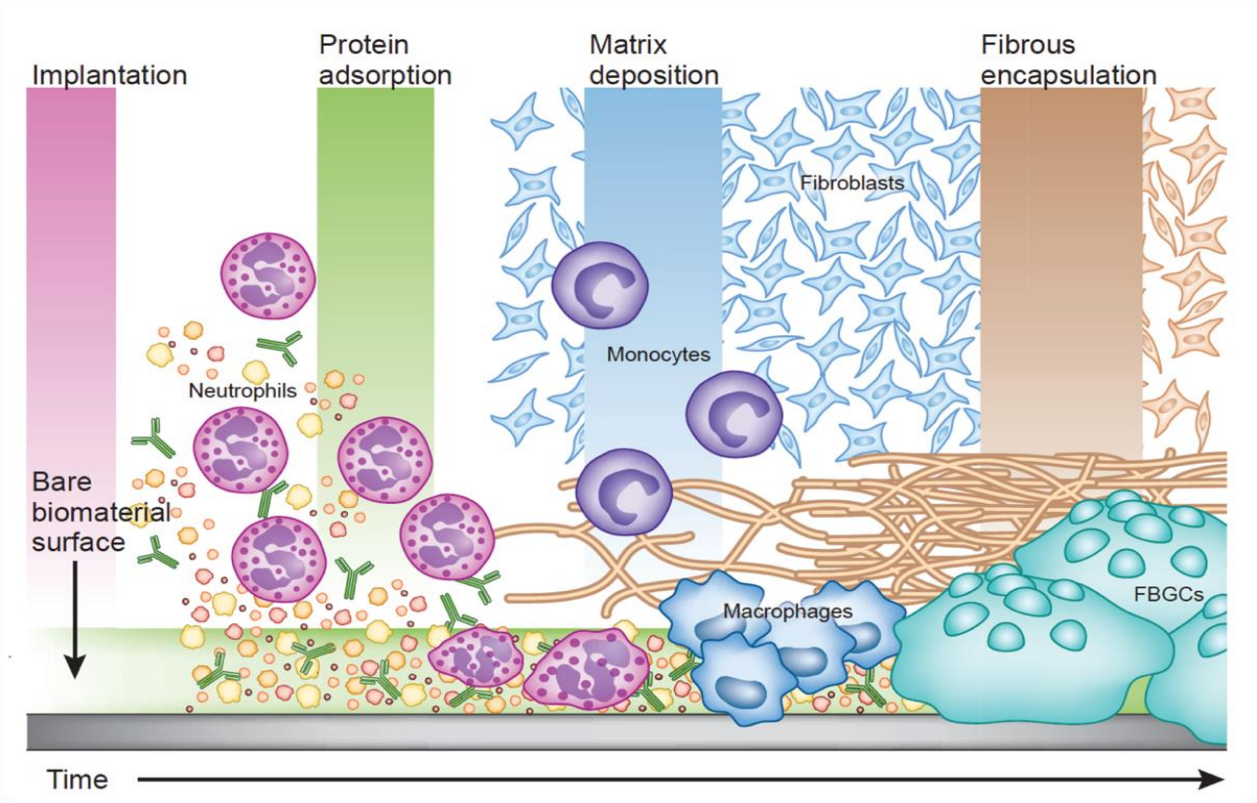

Figure 1.1: Temporal representation of the foreign body response leading to encapsulation of an implanted material. After immune response cells encounter unusual adsorbed protein coating, fibroblasts produce excess collagen correlated with formation of foreign-body giant cells (FBGCs) [10].

malfunctions of clinical implantable devices. For example, the adherent macrophages and foreign body giant cells crack the leads of a pacemaker because it can cause areas of stress concentration [20]. Furthermore, α2-macroglobulin, a protein locally synthesized by macrophages, catalyzes oxidation and chain cleavage of polyurethane parts in a pacemakers [21].

Most functional loss of biosensors is related to the foreign body reaction, especially the inflammatory response and the fibrous encapsulation [22]. That is, the adsorbed protein and the fibrous capsule can physically hinder the diffusion of biomarkers to the sensor surface [23], [24]. One of the critical malfunctions in medical shunt systems, such as hydrocephalus catheter and glaucoma drainage devices, is tube occlusion by biofoulings. A blockage of medical shunts can occur in any part of the device by blood cells, tissues or bacteria [19], [25]. Shunt obstruction for cerebrospinal fluid management accounts for more than 50% of shunt failures in the pediatric

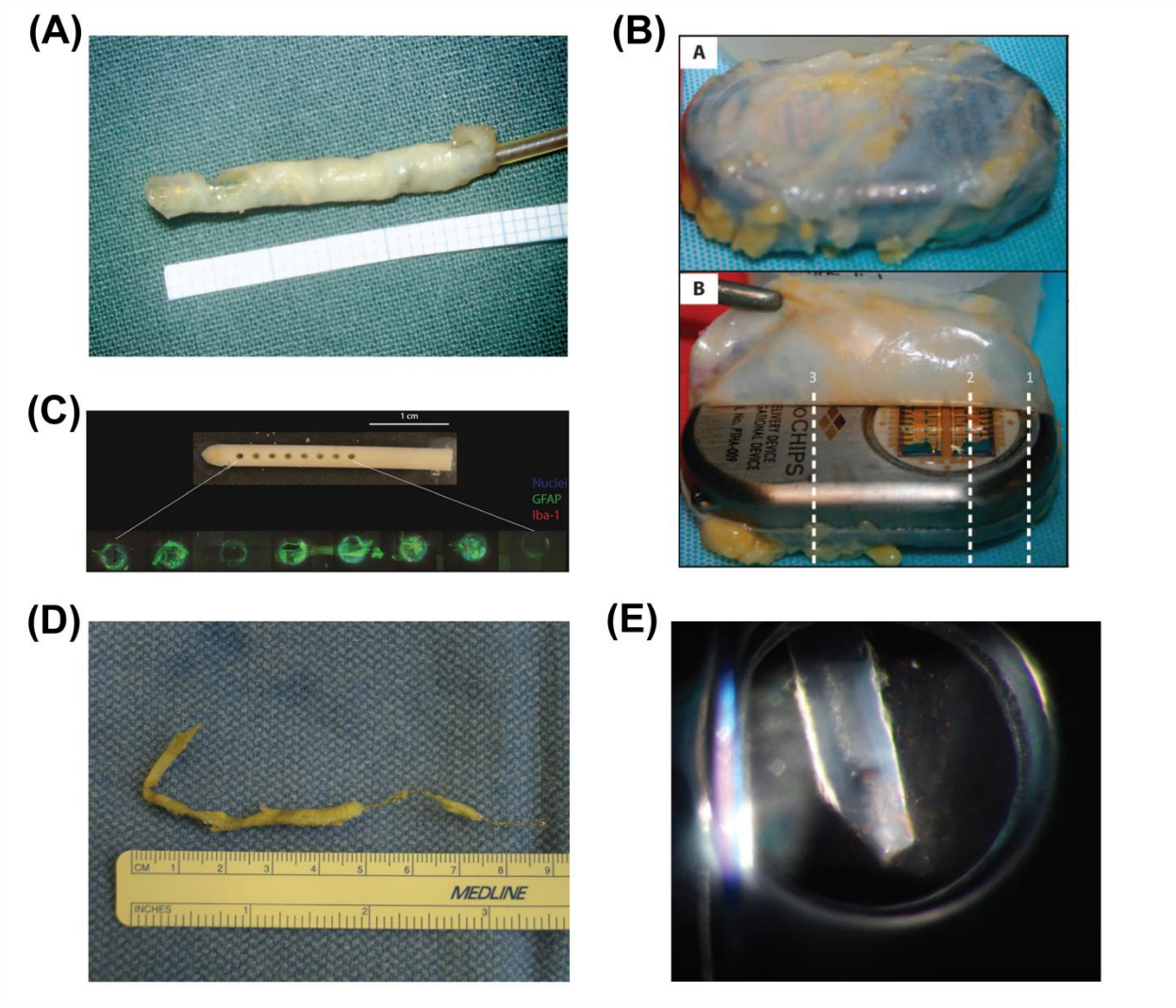

Figure 1.2: Biotic failures of implantable devices due to biofoulings. (A) A pacemaker lead surrounded by fibrous capsule [13]. (Open square = 1 mm) (B) Macroscopic images of the tissue capsule surrounding the wirelessly controlled drug delivery microchip device after explantation (A and B) [14]. (C) Attached cells on the surfaces between the fluid intake holes in a hydrocephalus shunt [15]. (D) A thrombotic occlusion of a multiple overlapping stents [19]. (E) The end of glaucoma shunt tube blocked by a translucent vitreous gel with pigment deposition [16].

population [26]. Tube occlusion in glaucoma drainage devices directly results in failure of intraocular pressure control by inflammatory deposits or debris [17], [27].

1.3 Current Strategies for Resisting Biofouling

To inhibit surface biofouling, several anti-biofouling materials have been designed by the manipulation of physical and chemical surface properties. Hydrophilic surfaces can prevent the adhesion of biofouling agents by the formation of a hydration layer [28]. For example, polyethylene glycol (PEG) is widely used in biomedical devices as a hydrophilic anti-biofouling coating [29]. The use of superhydrophobic surfaces is another promising anti-biofouling strategy. Superhydrophobic surfaces with fluorinated functional materials are designed to repel the water and microbe attachments, which can significantly reduce bacterial adhesion [30], [31].

Zwitterionic materials such as poly(sulfobetaine) and poly(carboxybetaine) adhere to methacrylate backbones to prevent non-specific adhesion of biofouling by maintaining charge neutrality of the surface and surface hydration [32]. Proteins can adsorb zwitterionic surfaces because they randomly have positively and negatively charged residues [33]. Therefore, a homogenous mixture of balanced charge groups from zwitterionic materials can tune anti-biofouling properties. Positively charged surfaces disrupt anti-microbial activity, which can reduce biofilm formation or kill bacterial cells [34], [35]. Cationic charged coatings composed of polysaccharide materials such as chitosan suppress antimicrobial activity against bacteria and fungi without adverse effects on mammalian cells [36].

Although these anti-fouling strategies using surface functionalization with different materials have been used to reduce the progression of biological attachments, they are not reliable enough for a prolonged exposure in a biological environment. Moreover, these strategies usually target a specific type of biofouling agent and its associated surroundings, but they often fail to inhibit the adsorption of others [37]. Furthermore, the surface modification strategies often require chemical or physical treatments such as oxygen plasma treatment or metal deposition, which can affect characteristics and functionalities of the resulting devices. Thus, the anti-biofouling materials may be degraded during the device fabrication procedure with high temperature and pressure environments.

1.4 Mechanical Anti-Biofouling Strategies

Passive surface treatment methods described above can reduce the amount of adsorption of the biofoulings, but they often fail in the body after an extended period of time. Furthermore,

the anti-biofouling capability depends on the density and chain length of the chemicals for passivation coatings [38]. To solve the issues, mechanical anti-biofouling techniques including vibration, fluid flow, and shear stress have been researched.

Vibration is a main technique used as a mechanical protein removing method in MEMS-based devices for locally inducing fluidic shear stress. Yeh et al. developed the vibrating piezoelectric plate to decrease protein adsorption for MEMS-based devices [39]. The silver coated lead zirconate titanite (PZT) generated vibration at 16 kHz, which results in removing up to 50% of BSA and IgG from the device surfaces. Acoustic streaming generated by the vibration desorbed the protein away. Authors also claimed that the electrostatic repulsion from the device assisted the protein desorption by overcoming Van Der Waals and hydrophobic adhesion interactions.

Pepakayala et al. reported that magnetoelastic resonators can limit the cellular adhesion on the GDDs [40]. They designed a paddle circumscribing the posterior portion of the plate body in a GDD. The paddle consists of magnetoelastic material, which can wirelessly oscillate due to externally applied magnetic field. The vibration from the paddle at resonant frequency varying from 520 Hz to 4.7 kHz and the average flow velocity of up to 266 $\mu m\ s^{-1}$ generated around the device to mitigate fibrosis in GDDs.

Pan et al. developed a microfabricated hypersonic resonator with 2.5 gigahertz resonant frequency to remove the nonspecific binding on biosensors [41]. The cleaning forces were investigated using the FEM simulation identified that the vortex induced by the vibration hydrodynamically removes the nonspecifically found proteins on the resonator and on other substrates contacting the vortexes.

Johnson et al. fabricated electrochemical piezoelectric millimeter-sized cantilevers to release nonspecifically adsorbed proteins by vibration [42]. The transverse resonant vibration of the cantilever released adsorbed bovine and human serum albumin proteins. They examined the release of nonspecifically adsorbed protein by electrochemical sensing, mass-change sensing, and fluorescence assays, which results in removal of 63.2% of the adsorbed proteins. The release of the proteins resulted from acoustic streaming and body force effects by the vibration.

These mechanical actuation strategies provide efficient way to decrease or remove biofoulings on bioMEMS or implantable devices. However, they cannot be easily integrated with microscale implantable devices such as micro invasive glaucoma shunt because they often require external circuits and battery.

1.5 Abiotic Failures in Implantable Devices

Despite the increasing demand for more advanced implantable medical devices, the modern implantable devices are faced with several challenges. Active implantable devices with integrated circuits and sensors are often faced with challenges including packaging and limited battery lifetime [43]. Implantable medical devices are generally operated by electrical connections between electronic components. To protect the electronic parts from the body fluid, the packaging of the device should perfectly isolate the inner systems. The packaging is done by using various materials such as quartz, polymer, metals, ceramics, and fused silica. However, the device packaging is often large compared to the electronics inside, which results in a larger wound [44]. Furthermore, packaging materials induce a foreign body response that could initiates device degradation and malfunctions.

Engineering an electric power supplier with a high capacity for implantable devices is one of the main challenges in the design scheme of the devices. Cochlear implants and retinal prostheses have rechargeable batteries. However, pacemakers and deep brain stimulators use one-time-use batteries, which should be changed by operation when the electrical power of the device is not properly working. Recently, energy harvesting using physical, chemical, and mechanical phenomena of the body has been developed to solve the battery issue of implantable devices. However, the energy harvesting techniques still need to be improved because they can only produce low levels of energy with poor efficiency.

The human body is a chemically harsh environment, which leads to implant degradation. Corrosion, the gradual degradation of materials, is induced by an electrochemical attack of the body fluid composed of water, dissolved oxygen, sodium, chlorine, proteins, plasma, and amino acids [45]. Electrochemical reactions can be accelerated by applying voltage or current flow through the device's surface thus consuming the products. Proteins also can bind to metal ions on the implant's surface and transport them to a medium for maintaining chemical equilibrium in the solution. Device implantation leads electrochemical variation in the equilibrium state to accelerate corrosion rate by changing reaction constants. In addition, the pH of the body fluid can drop from 7 to 4 during recover phase or by bacterial infection, which can also influence the corrosion rate.

Corrosion of metal components can make parts of implants brittle and fractured. Corrosion is the most common failures in biomedical implants (Fig 1.1) [46]–[48]. Although the surface oxide layer that forms on metallic materials may act as a protective film against corrosion, the

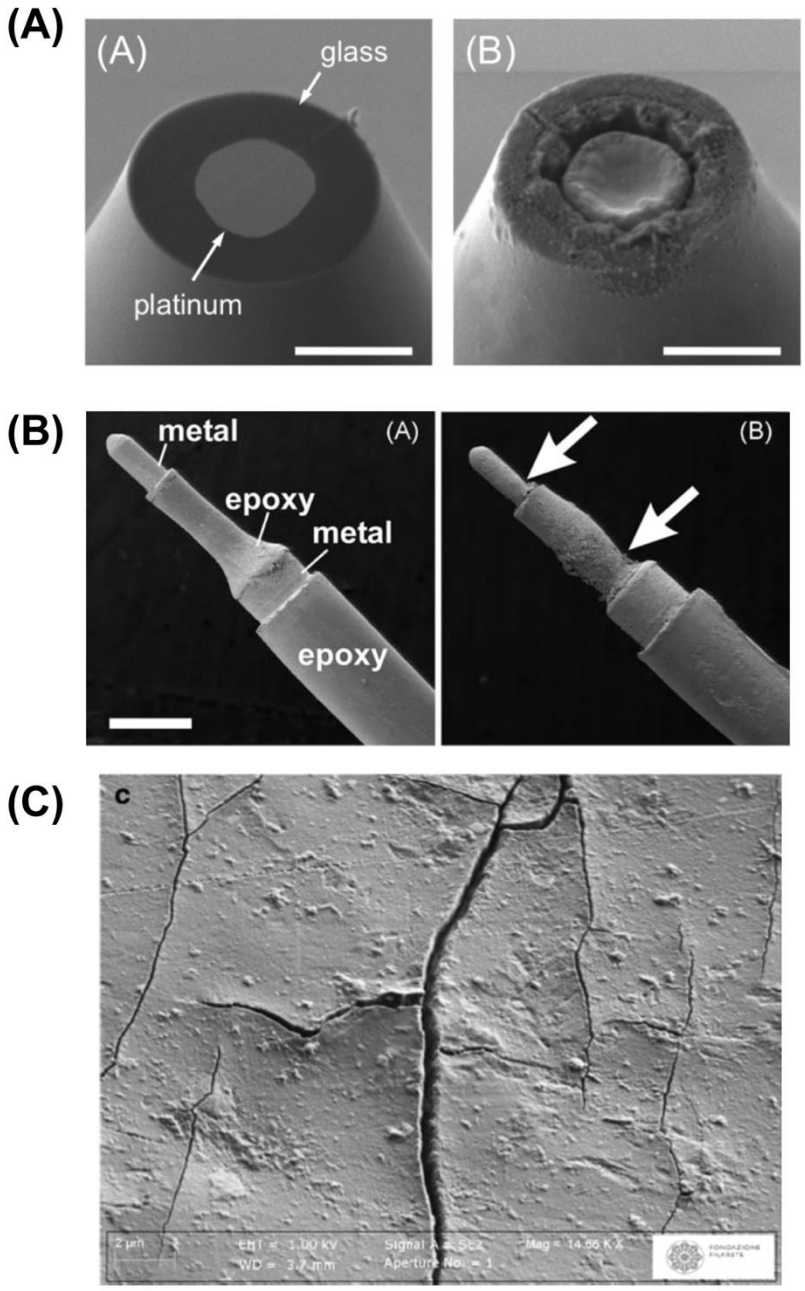

Figure 1.3: Abiotic Failures in Implantable Medical Devices. (A) SEM images of a Pt microelectrode before (Left) and after (Right) electrical discharge [46]. Scaler bar = 1 μm. (B) Electrode corrosion and epoxy erosion of stainless-steel electrodes after continuous 8 hrs stimulation [47]. Scale bar = 300 μm. (C) SEM image of the explanted DBS lead [48].

layer can be dissolved by active oxygen species in body fluid. Once the metal parts fracture, corrosion accelerates causing an increase of metal-body fluid interface area without protective oxide layer. The release of corroded metals from implants can lead to adverse biological effects in

the tissue near the implantable devices and as well as other parts of the body. For example, cobalt-chromium alloy which is a commonly used in dental or orthopedic implants releases carcinogenic toxins. The corroded titanium-aluminum-vanadium alloy used in joint replacements, bone fixation, and heart pacemakers could lead to long-term ill effects such as osteomalacia, Alzheimer's disease, and peripheral neuropathy due to the release of metal.

1.6 Current Strategies for Abiotic Failures

There been several attempts to improve the reliability of implantable devices against the failure owing to corrosion. Various protection coatings such as plasma immersion ion implantation and polymer passivation coating were applied to prevent corrosion of active implants [49], [50]. Diamond films have been gaining attention as an ideal candidate for corrosion resistance coatings on implantable devices due to their mechanical properties, chemical inertness, and biocompatibility [51]–[53]. Hydroxy-apatite, a natural composite material for bone tissues, coatings on implants showed good corrosion protection by preventing ion release from the metallic surface [54]. In the case of titanium (Ti) and Ti alloys, which are generally used in dental and orthopedic implants, corrosion can be prevented by biocompatible and biodegradable coatings [55], [56]. Laser-induced surface modifications have also been utilized to improve surface properties of Ti-based medical implant devices. By laser surface treatment in nitrogen gas, Ti surface is passivated by titanium nitride (TiN) which has significantly improved corrosion resistance [57], [58].

However, the application of aforementioned methods is limited in neurostimulation devices, which operate in high electrical potential and current. Implantable devices for electrical stimulation such as deep brain stimulation, peripheral nerve stimulation, and pacemakers transfer electrical charge to activate or block the electrophysiological signals of neurons. The electrolytic corrosion rate is even more increased in micro-scaled electrodes due to their increased current density. The passivation layer or anti-corrosion coatings must be carefully considered because additional layers on stimulating electrodes can negatively affect the performance of the device. Although capacitive charge-injection materials such as TiN and tantalum/tantalum oxide could be used as an electrode material because of their chemical inertness, their charge transfer efficiency is lower than conventional Faradaic charge transfer materials including platinum (Pt), Pt-iridium alloy, and iridium oxide. Corrosion rates may be controlled by adjusting the stimulation parameters

such as pulse width, frequency, and inter-pulse delay, however, the broad range of adjustment parameters must be optimized to achieve therapeutic effects for each patient.

1.7 Scope of Study

The objective of this study is the development of strategies for increasing reliability of implantable devices against biotic and abiotic failures. More specifically, the primary goal is to: 1) Develop a self-clearing implantable microshunt featuring magnetic microactuators; 2) Design a new microelectrode that efficiently transfers electric charge on a small scale and is robust against electrochemical corrosion. In order to achieve these goals, the primary strategy was microfabrication of the magnetic actuator using a flexible polymer substrate, and construction of platinum-based neurostimulation electrode on silicon substrate.

In Chapter 2, I will discuss the development of rapid prototyping of a magnetic microactuator using a copper cladded liquid crystal polymer. The device was designed by finite element modeling to achieve threshold shear stress for removing non-specifically binding proteins. To fabricate the device with low-cost and reduced fabrication steps, maskless photolithography setup was constructed. Device integration, mechanical characterization, and protein removal capabilities were accomplished. In Chapter 3, a fractal geometry is proposed to improve charge injection limit of a Pt-based neurostimulation electrode. Before electrode fabrication, charge transfer efficiency of electrode designs with high perimeter-to-surface area ratios was calculated using numerical modeling. Electrodes were fabricated through conventional MEMS process. Electrochemical characterization of the different electrode designs is presented. In Chapter 4, a graphene protection layer is used to prevent electrochemical corrosion of the fractal electrode. The corrosion rates of bare Pt and graphene coated fractal microelectrode were compared. Chapter 5 will conclude this dissertation with closing remarks and future research direction.

2. SMART SELF-CLEARING GLAUCOMA DRAINAGE DEVICE

2.1 Introduction

The main function of the eyes is to receive and transmit of the light signal from the environment to the optic nerve. As such, unlike other tissues of the body, the structures of the eye must be transparent without blood interference. The eye also must maintain global structure with an optimum pressure to provide rigid optical alignment of the cornea, lens, and the retina. The eye achieves this by aqueous humor (AH) with controlled production and drainage flow rate.

The AH is produced by three mechanisms: diffusion, ultrafiltration, and active secretion in the ciliary body (Fig. 2.1). Diffusion transfers solutes and water of the AH by concentration gradient between the ciliary capillaries and the posterior chamber [59], [60]. An ultrafiltrate is passed through the fenestrated ciliary capillaries into the ciliary stroma by a pressure gradient. Active secretion is responsible for approximately 80 % to 90 % of the total AH production. The non-pigmented epithelial cells in the ciliary body are the main site for active transport of the AH. In active secretion, ions are transported into the posterior chamber against a concentration gradient by protein transporters abundantly distributed in non-pigmented epithelial cells in the ciliary body. Furthermore, aquaporins in the cellular membrane rapidly transfer fluid against an insufficient osmotic pressure gap. The energy required for the protein transporters is derived from hydrolysis

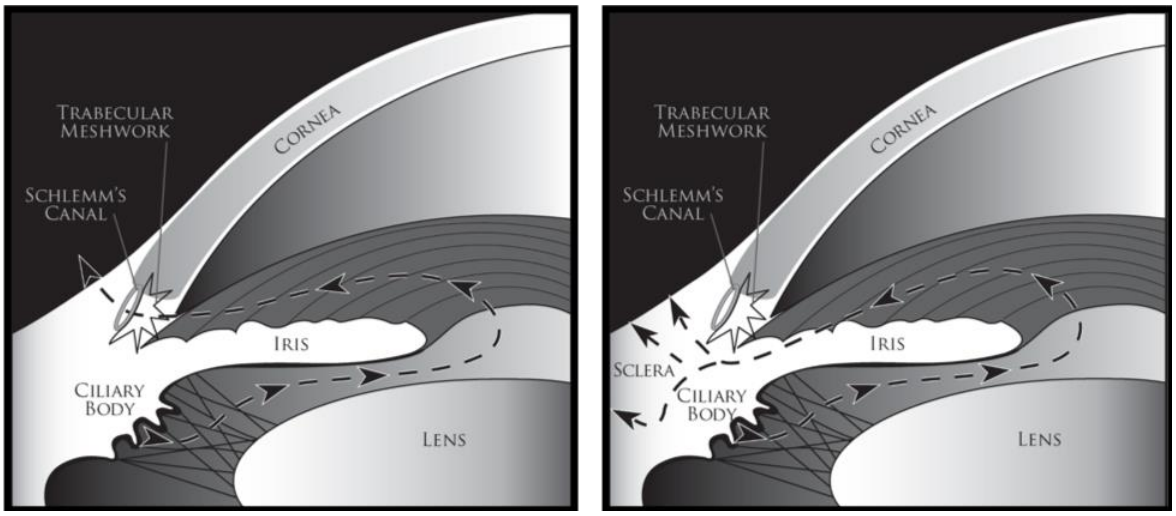

Figure 2.1: Schematic diagram illustration of the trabecular meshwork conventional outflow pathway (Left) and the uveoscleral outflow pathway (Right) [74]

of adenosine triphosphate. The production rate of AH is approximately 2.5 μL min^{-1}, which is estimated to be approximately 1 – 1.5 % of the anterior chamber volume per minute.

Glaucoma is a group of eye diseases that causes progressive damage to optic nerve. Typically, glaucoma patients experience poor drainage of aqueous humor (AH) through the natural outflow pathways (i.e., trabecular meshwork and Schlemm's canal) [61]. The imbalance between the rate of production and the outflow of AH from the eye causes an increased intraocular pressure (IOP), which is a major risk factor that leads to subsequent damage to optic nerve and the loss of eyesight [62], [63]. It is commonly known as "the silent thief of sight" due to the lack of symptoms during the early stages [64]. Because of this difficulty in early diagnosis, glaucoma remains as one of the leading causes of blindness and visual impairments in the world [65]. It currently affects around 64.3 million people in the world and this number is expected to double by 2040 [66], [67]. In the United States, there are more than 3 million patients with glaucoma and it disproportionally affects African Americans and Hispanics [68]–[72]. Glaucoma is a major healthcare issue with the annual cost for treatment in the US that exceeds $2.9 billion.

Unfortunately, there is no cure for glaucoma. However, the progression of disease can significantly be delayed using pharmaceutical and surgical interventions that maintain the IOP in a safe range to minimize optic nerve damage [73]. Glaucoma drugs are typically designed to decrease the production of AH or to increasing its outflow through trabecular meshwork or uveoscleral pathway [74]–[76]. As with most pharmaceutical interventions, however, these drugs have several undesirable side effects including bitter taste, headache, conjunctivitis, visual blurring, eyelid inflammation, and eye pain [77]–[79]. Surgical treatments such as trabeculectomy and laser trabeculoplasty can also be used to increase AH outflow but these invasive procedures often lead to serious post-operative complications such as hypotony, cataract, and bleb-related infections [80]–[83]. Moreover, the surgical ablation of trabecular meshwork often results in coagulative necrotic tissue, which can cause difficulty in chronic management of optimal AH outflow [84].

2.2 Glaucoma Drainage Devices

For patients with refractory or inflammatory glaucoma who are unresponsive to conventional pharmacological or surgical procedures, glaucoma drainage device (GDD) are often implanted (Fig. 2.2). These devices offer several advantages over conventional trabeculectomy

including better IOP control, ease of surgery, and minimum post-surgical complications [85]–[87]. Traditional GDDs consists of a short polymeric microscale tube that connects the anterior chamber to a thin silicone plate for drainage of excess AH [88]–[90]. While GDDs have been used to manage IOP for glaucoma patients for the past 40 years, 15.1% of implanted devices fail within 3 years and more than 29.8% fail within 5 years post-implantation [91], [92]. Clinical studies have shown that up to 10% of glaucoma patients require additional medications and surgical intervention because of the tube blockage [93]. The hydrophobic polymer materials from which GDDs are constructed (e.g., polypropylene, polymethylmethacrylate, and polydimethylsiloxane) typically have high affinity for interstitial proteins such as fibrinogen, immunoglobulin, and albumin that adsorbs onto the device surface within minutes after the implantation [94]–[96]. Once it forms, the proteinaceous layer triggers the inflammatory response that can lead to premature implantable device failure [97]. Since GDDs generally have a drainage tube with an inner diameter

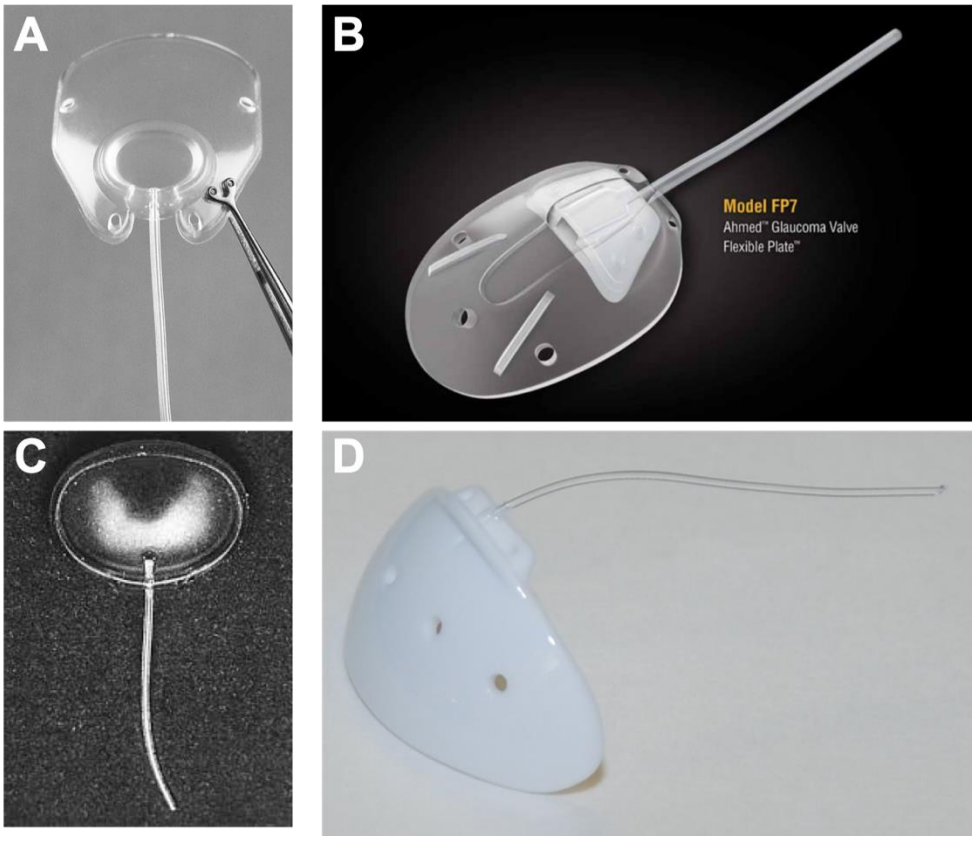

Figure 2.2: Glaucoma drainage implants with a tube and an explant plate. **(A)** Molteno implants with single-plate. (B) Ahmed glaucoma valve. (C) Krupin slit valve (D) Baerveldt glaucoma implants.

that ranges from 50 to 600 μm, the microscale channel can easily be occluded by various biofouling materials including vitreous, fibrin, or blood clot [98]–[101].

One promising approach that can remove adsorbed biofouling material is to ablate occlusion using neodymium-doped yttrium aluminum garnet (Nd:YAG) laser. However, there are several potential risks associated with laser treatments including focal cataracts, prolonged elevation of the intraocular pressure, posterior capsule rupture, retinal injury, and laser injury [102]–[108]. Tissue plasminogen activator (tPA), which is a serine protease involved in the breakdown of fibrin or blood clots, has also been used to clear occluded glaucoma shunts [109], [110]. However, tPA may cause additional undesirable complications such as hyphema, active bleeding, and vitreous hemorrhage [111]–[113]. Establishing a method to non-invasively remove biofouling without causing side effects can significantly improve the reliability and functionality of many chronically implanted devices.

Here we report on the design, fabrication, and testing of anti-biofouling micro- tube integrated with an array of magnetic microactuators as a part of a self-clearing GDD that can actively combat against proteinaceous biofouling in situ without the need for additional surgical or pharmaceutical interventions. We believe our strategy to remove bioaccumulation on-demand using externally applied magnetic field is a way to significantly improve the functional lifetime of implantable devices that suffer from biofouling-related performance degradation. By integrating thin-film magnetic microactuators fabricated out of liquid crystal polymer (LCP) using maskless lithography, here we demonstrate a low-cost prototype of self-clearing GDD drainage tube (Fig.2. 3). Using fluorescent-tagged bovine serum albumin (BSA-FITC), we show the protein-clearing

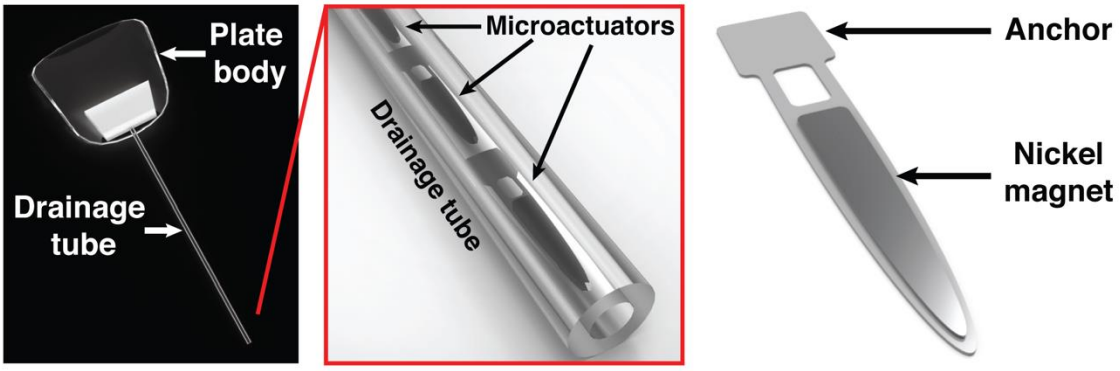

Figure 2.3: 3D schematics of self-clearing GDD

capabilities of these prototype GDD microtubes using time-varying magnetic fields, which may eliminate the need for additional surgical or pharmaceutical interventions for glaucoma patients.

2.3 Device Design using Finite Element Modeling

We designed the microactuator as a semi-ellipsoidal shape to maximize the volume of the magnet element on the actuator. To determine the shear stress generated by the actuation based on the design, we used a finite volume method to simulate shear stress on the surface of microactuator and the lumen of the microtube by numerically solving Navier–Stokes equations. We discretized the computational domain using a uniform, staggered, cartesian grid. We used Euler explicit method for time discretization and spatial derivatives in convective and computed diffusive terms using the quadratic upstream interpolation for convective kinematics and central difference schemes, respectively [114]. Furthermore, we coupled the pressure and velocity using a projection method [115]. We implemented a distributed Lagrange multiplier method to simulate the motion of microactuator in a viscous fluid, which allowed us to accurately capture the hydrodynamic interaction between the microactuator and a surrounding fluid and evaluate the shear stress acting on the surface [116].

We evaluated the shear stress distribution generated by the microactuation motion using finite element modeling. The simulation results showed that the maximum shear stress is generated near the perimeter of the actuator (Fig. 2.4A). When the device is integrated into the microtube, the actuation leads to a larger shear stress as the microactuator approaches the tube wall (Fig. 2.4 C). During the actuation, the maximum shear stress of ~ 8 and ~ 10 dyn cm^{-2} are generated periodically on the surface of the actuator and the tube, respectively (Fig. 2.4B and D).

2.4 Device Fabrication

The cantilever and the magnetic element patterns were made using a maskless photolithography as described in Fig. 2.5. The computer is connected to a projector (HD 141X, Optoma, Fremont, CA, USA) with a digital micromirror device (DMD) to project and expose a desired pattern (Fig 2.5A). Projector was vertically fixed on a stereo-microscope using a custom machined bracket. To improve the resolution and reduce the size of the image, lens and microscope were aligned between the sample stage and the projector. The mask pattern was designed using

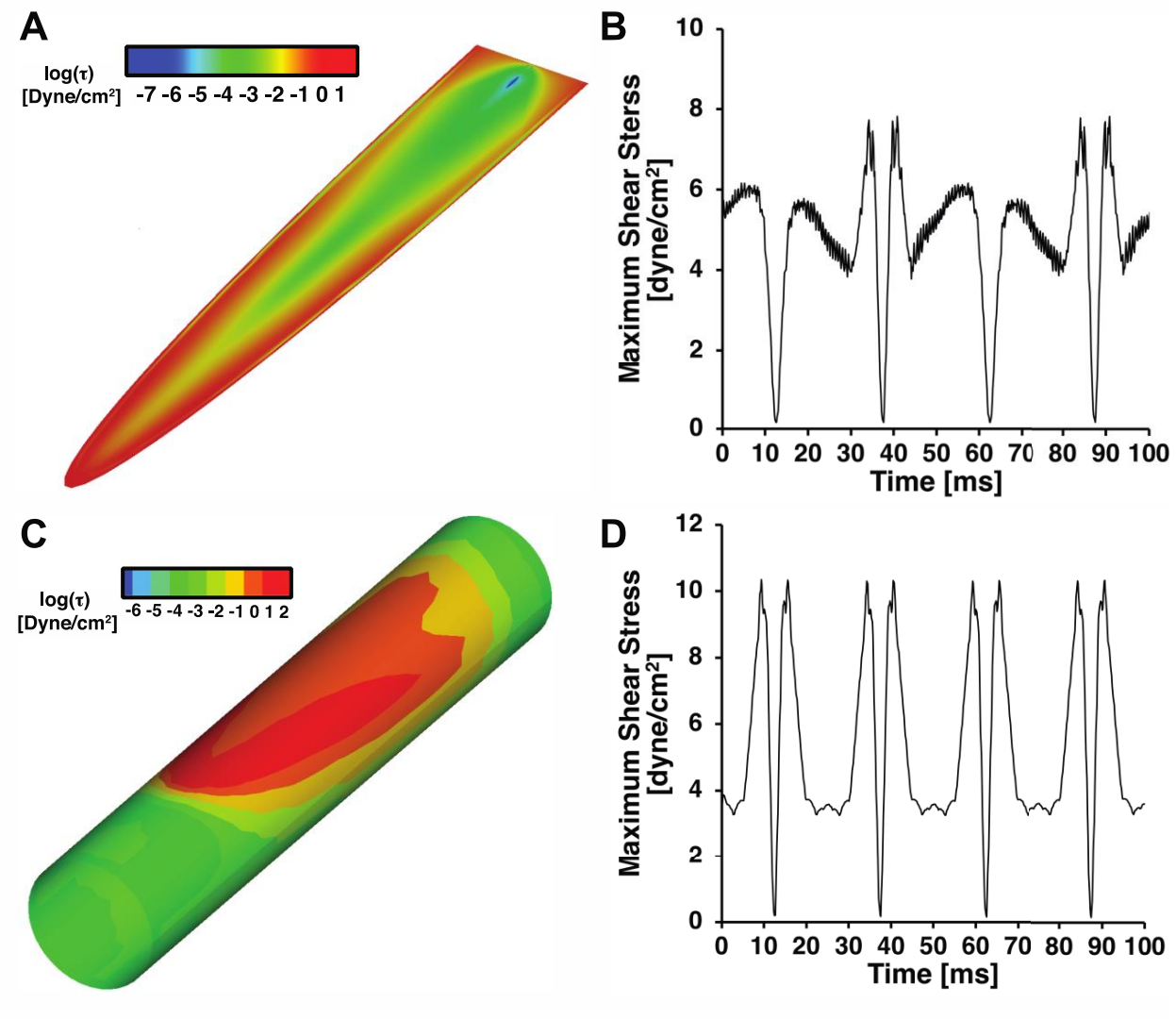

Figure 2.4: Numerical analysis of shear stress distribution. (A) Shear stress distribution generated on the surface of the actuators. (B) Maximum shear stress on the actuator surface as a function of time. (C) Shear stress distribution generated on the tube. (D) Maximum shear stress from the internal surface of the microtube as a function of time.

Microsoft PowerPoint. The exposure intensity was optimized by adjusting the pattern color in the software. Figure 2.5B shows the overall process flow for the device fabrication. The commercially available LCP sheet (Ultralam 3850, Rogers corporation, Chandler, AZ, USA) has a thickness of 25 μm. To improve compliance of the cantilevers, we reduced the LCP thickness to 8 μm using a reactive ion etcher (RIE, PlasmaPro80, Oxford Instruments plc, Abingdon, Oxfordshire, United Kingdom) after removing Cu from one side using a wet Cu etchant (CE-100, Transene, Danvers,

MA, USA). We then mounted the 8-µm-thick single clad LCP sheet onto a carrier wafer using a positive photoresist (PR) (AZ9260, Microchem, Westborough, MA, USA) with the Cu on top. We

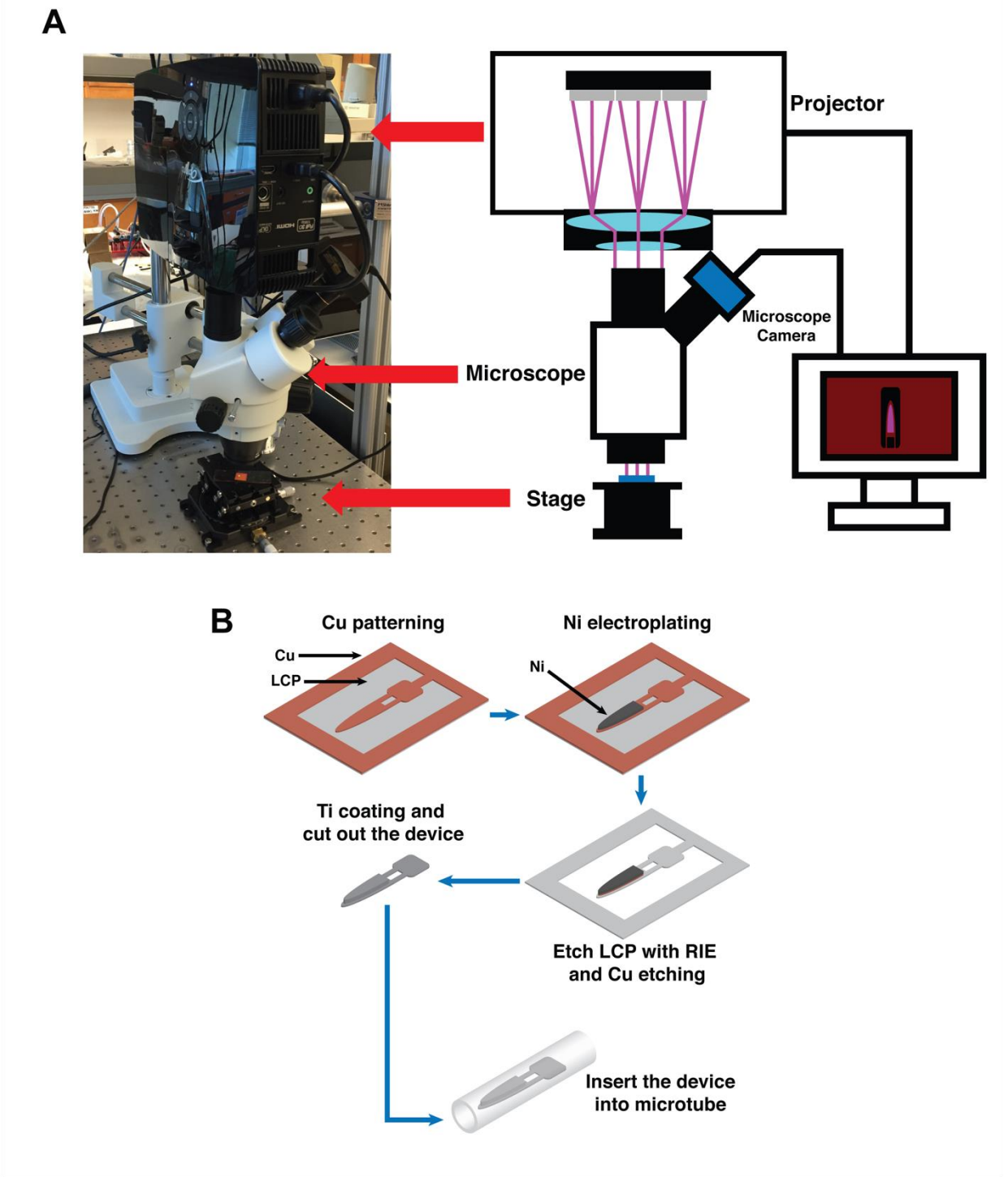

Figure 2.5: Microfabrication for the magnetic microactuator. (A) A custom maskless photolithography setup. (B) Fabrication procedure for the magnetic microactuator

spin coated AZ9260 onto the Cu layer and exposed the cantilevers designs using our custom maskless photolithography setup. After etching the Cu layer using a wet Cu etchant (CE-100, Transene, Danvers, MA, USA), we removed PR using acetone. Next, we defined the Ni magnet electroplating mold on spin-coated AZ9260 using the same maskless photolithography procedure. We electroplated Ni to achieve a final thickness of 20 μm. After removing the PR, we etched the cantilever pattern on bare LCP layer using an RIE and removed the remaining Cu layer using a chemical etchant (BTP, Transene, Danvers, MA, USA). Finally, we coated the device with 100 nm thick titanium (Ti) using a sputterer (Magnetron sputtering systems, PVD Products, Inc., Wilmington, MA, USA) on both sides to improve biocompatibility.

Figure 2.6 shows our microfabricated LCP-based device. The needle-shape was chosen to accommodate the relatively small tube diameter. We can control the deflection direction and amplitude of the microactuator by adjusting the strength and the direction of the externally applied magnetic field (Fig. 2.6B). We assembled the microdevices into a prototype GDD drainage tube using an anchor to demonstrate protein-removal performance inside the tube (Fig. 2.6C). Once

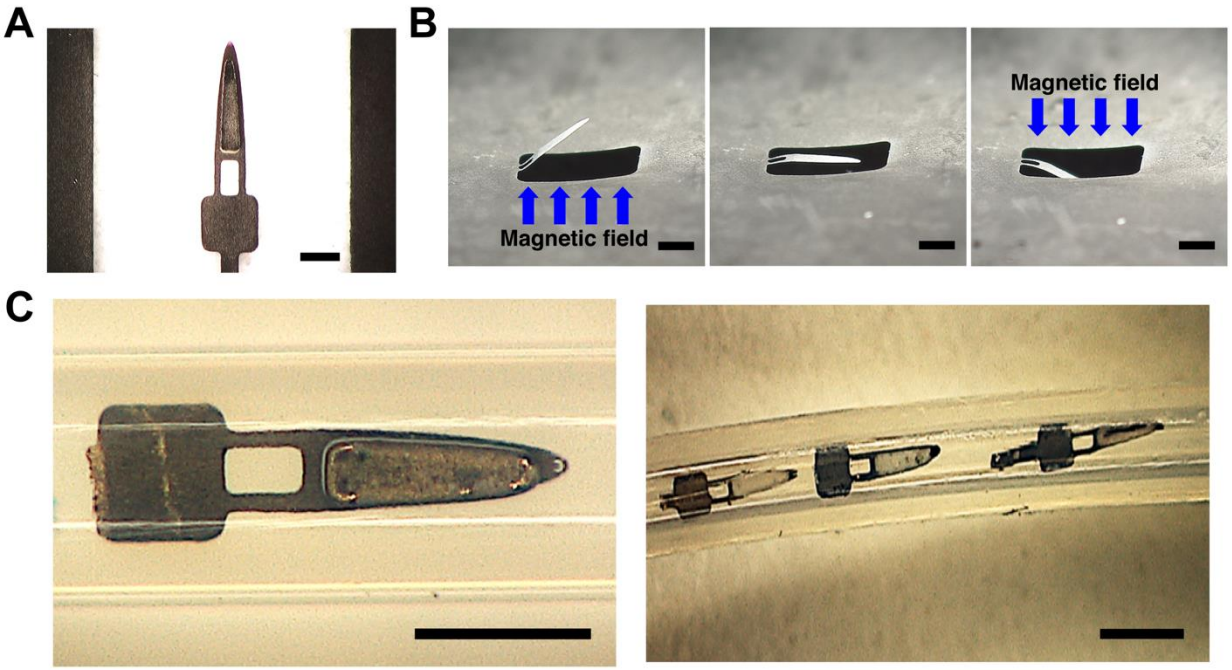

Figure 2.6: Images of fabricated microactuators and self-clearing GDD. (A) Digital photograph of the fabricated magnetic microactuators. Scale bar = 200 μm. (B) The deflected microactuator with different directional magnetic flux density with 13.7 mT. Scale bar = 200 μm. (C) Digital photographs of the integrated microactuators in the lumen of a prototype GDD microtube. Scale bar = 500 μm.

manually placed into the microtube, we heated the tube and applied tensile stress at both ends to decrease the diameter of the microtube and fix the microactuators in position, which prevented any shifting of devices during actuation in a continuous fluid flow.

2.5 Mechanical Characterization

We measured the magnitudes of angular deflections for a range of applied magnetic flux density up to 40.9 mT. We used a bespoke iron-core electromagnet to generate the magnetic field. We quantified the strength of magnetic field using a commercial gaussmeter (Model 8010, Pacific Scientific OECO, Milwaukie, OR, USA). We then placed the device on top of the electromagnet and applied the magnetic field of varying amplitude and frequency. We imaged the deflected actuators using a digital microscope KH8700, Hirox, Hackensack, NJ, USA) and calculated the deflection angles from the images using imageJ software (version 1.50i). To better characterize the motion of the devices in liquid, we also characterized the dynamic responses of the magnetic microactuators in deionized water using a custom laser deflecting setup. Using a mirror, we placed a laser beam onto the metallic surface of the device, which then reflected the laser beam onto a position sensitive diode (PSD) sensor. We recorded the two-dimensional position data from the PSD using a custom data acquisition system (LabView 2014, Austin, TX, USA).

The microactuators can deflect out of plane when the direction of the applied magnetic field is normal to the magnetization direction of the ferromagnetic element. The deflection angle of magnetic microactuator can be described in the reference [117].

$$\phi = \frac{V_m(\vec{M} \times \vec{H})}{k_{beam}}$$

with the angular deflection ϕ, magnet volume V_m, magnetization M, applied magnetic field H, and the flexure stiffness k_{beam}. The beam geometry and the material property affect the mechanical stiffness of the flexure with following

$$k_{beam} = \frac{E_c w t^3}{12 l}$$

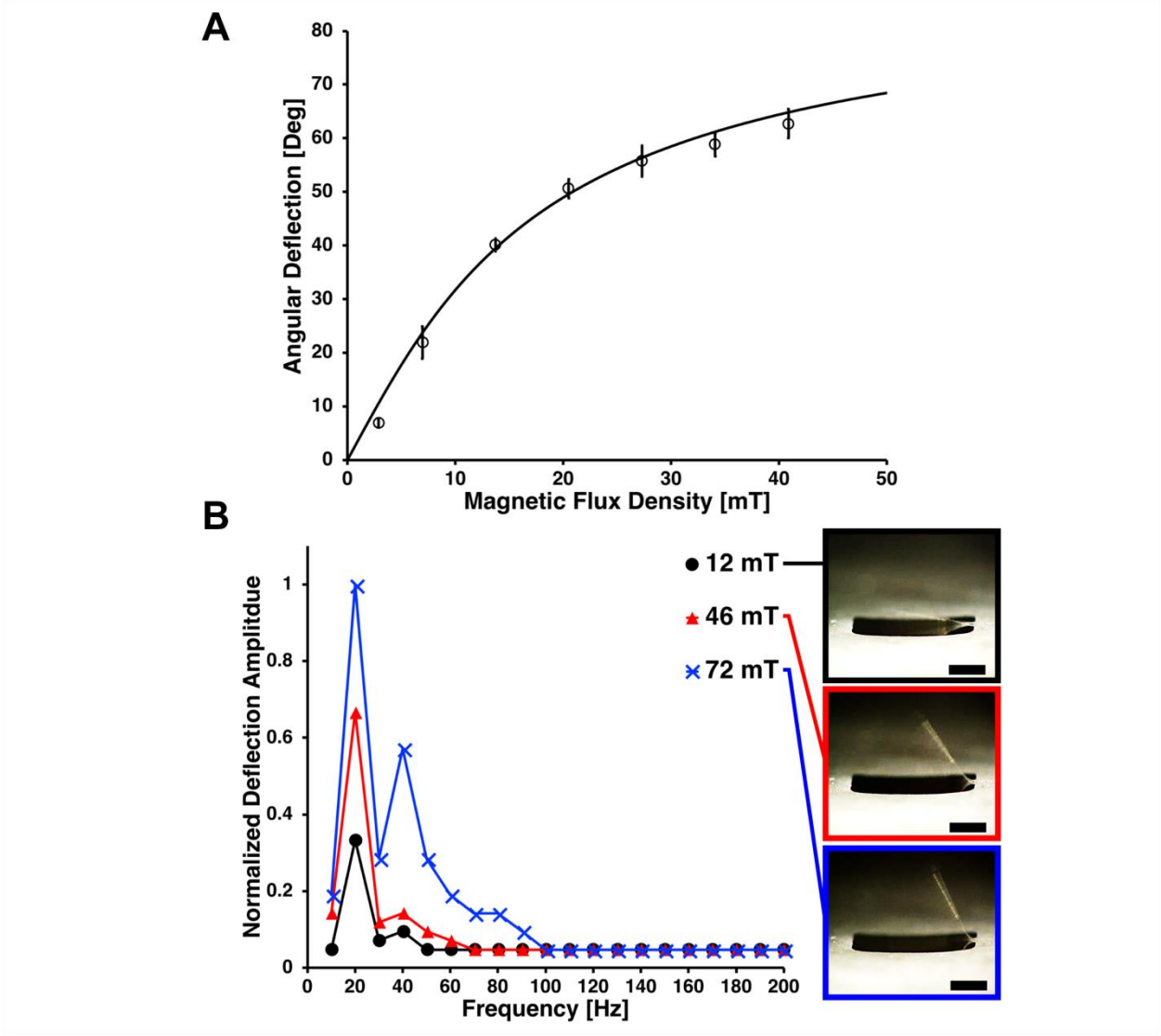

Figure 2.7: Static and dynamic characterization. (A) Theoretical and measured angular deflections (n = 3). (B) Frequency response of magnetic microactuator in the water. Note the captured images of microactuators in resonance at various magnetic flux density levels (inset). Scale bar = 500 μm

with the elastic modulus E_c, beam width w, beam thickness t, and beam length l [118]. As shown in Fig. 2.7A, the measured deflection angle corresponded closely with the theoretical values. We varied the frequency and amplitude of the externally applied, time varying magnetic fields using a custom electromagnet to obtain the frequency response (10–200 Hz) of our microactuators (Fig.

2.7B). As expected, the amplitude of deflection increased as a function of applied magnetic field strength. Furthermore, we determined that the actuation frequency of 20 Hz to be the primary resonance, which can be used to generate the highest dynamic deflection amplitude. The increase in dynamic deflection amplitude may be attributable to the increase in mean fluid velocity around the microactuator, which leads to an increase in the wall shear stress on the microactuator and the tube. Therefore, we used a fixed actuation frequency (20 Hz) with the highest actuation amplitude (64^{o}) for all experiments and simulation.

To verify these Ti-coated LCP based microactuator is robust enough to withstand a large number of actuation cycles in physiological condition, we examined the changes in the dynamic responses of these microdevices in 37 °C phosphate buffered saline (PBS, ThermoFisher Scientific, Waltham, MA, USA). After 10.9 million actuation cycles, we saw no visible damage to the LCP-based microactuators and no change in the resonant frequency of tested devices (n= 4, Fig 2.8). If we assume a 5-min weekly actuation, this equates to up to 35 years of lifetime, which suggests adequate robustness for our LCP-based microactuators against fatigue related failure.

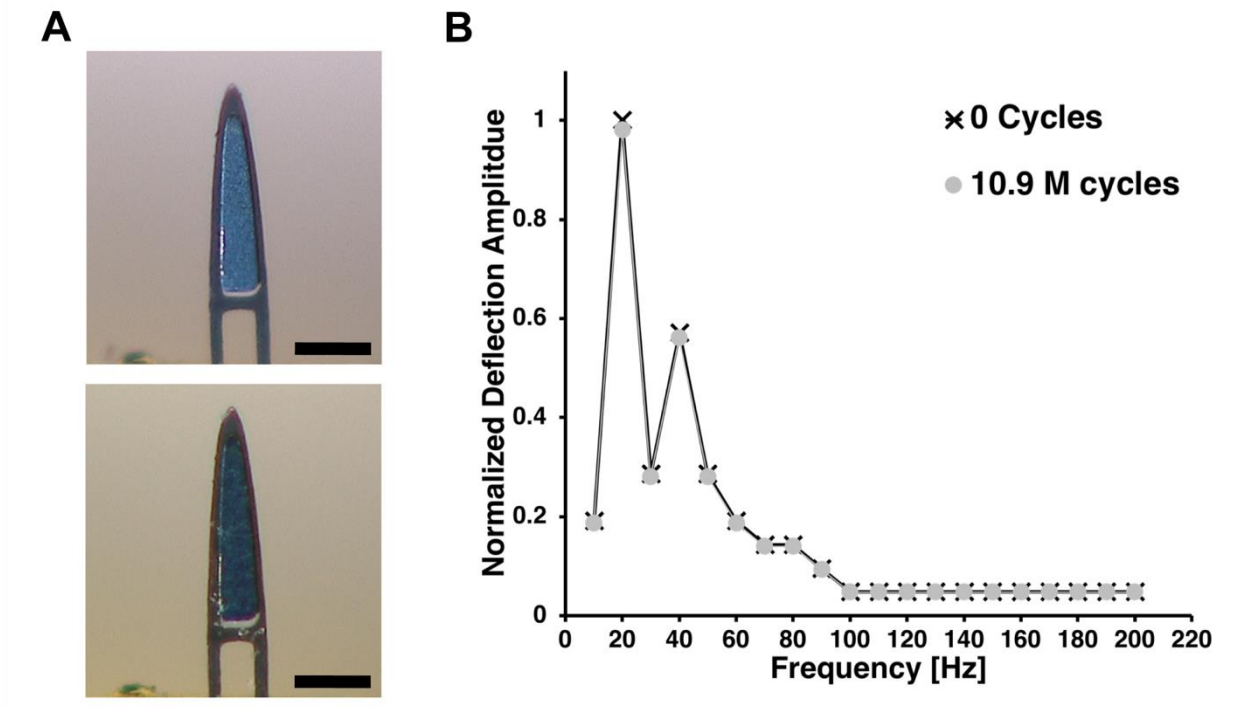

Figure 2.8: Fatigue evaluations**.** (A) Photographs of a microactuator before actuation (top) and after 10.9 M actuation cycles (bottom). Scale bar = 100 µm. (B) Frequency responses of a representative device before and after long-term actuation in PBS.

2.6 BSA-FITC Adsorption and Desorption

To maximize the fluorescence intensity, we incubated Ti-coated LCP samples in various concentrations of BSA- FITC (1 – 8 mg ml^{-1}) for 2 h. The fluorescence intensity of absorbed BSA-FITC plateaued around 5 mg ml^{-1} (Fig. 2.9A), therefore, all subsequent BSA-FITC evaluations used this concentration. The jet impingement technique is widely used to analyze the shear stress required to remove cells by corresponding the size of a lesion created by a perpendicular jet of fluid to a well-characterized shear stress profile.

To quantify the adhesion strength of BSA- FITC on Ti-coated LCP surface, we used the theoretical description of the wall shear stress under the impinging jet proposed by Phares et al [119]. For this analysis, we assumed that the AH is incompressible Newtonian fluid in a steady and laminar flow. In the theoretical description of the wall shear stress in normally impinging jet with jet height H, the wall shear stress τ at a radial distance r can be described by

$$\frac{\tau}{\tau_m} = 0.18\left(\frac{1 - e^{-114\lambda^2}}{\lambda}\right) - 0.943\lambda e^{-114\lambda^2}$$

with the maximum shear stress τ_m and non-dimensionalized jet height ($\lambda = r/H$). The maximum shear stress τ_m is given by

$$\tau_m = 0.16\frac{\rho u_0^2}{(H/D)^2}$$

with the fluid density ρ, the average flow velocity at the nozzle exit u_0, and diameter for the nozzle D. The critical shear stress (τ_c) required to remove the adsorbed BSA- FITC can then be calculated by measuring the radius of lesion (Fig. 2.9B). In the jet impingement test, the fluid jet was

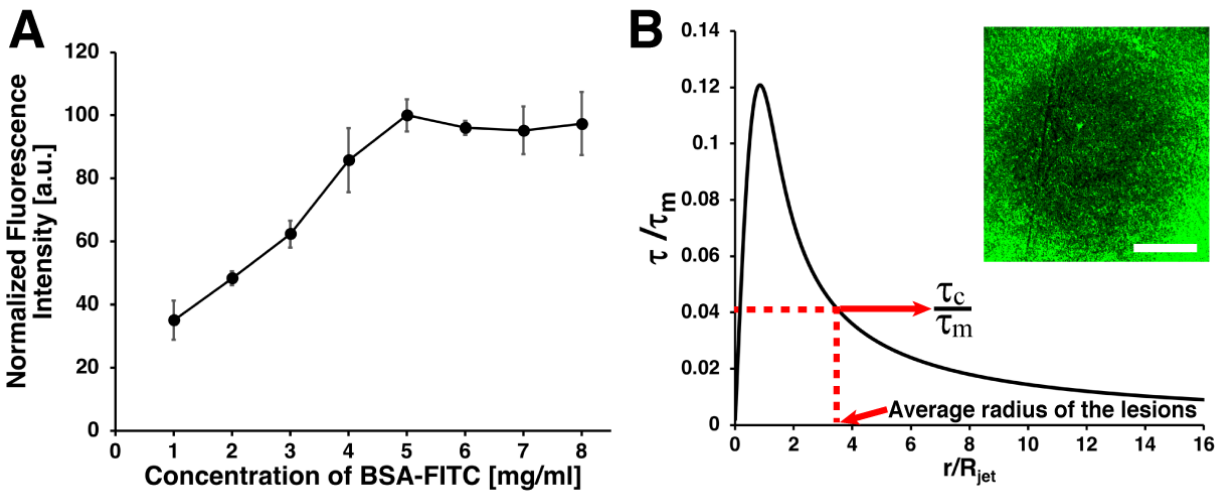

Figure 2.9: Optimization of BSA-FITC coating and jet impingement test. (A) The relationship between adsorbed BSA-FITC and the concentration of the protein solution with 2 hours incubation (n=5). (B) Plot of non-dimensional shear stress versus lesion size. Note the image of lesion created using jet impingement (inset). Scale bar = 200 µm. The dotted line and arrows point to the average lesion size and the corresponding non-dimensional shear stress.

delivered at a flow rate of 1.18 ml min^{-1} for 5 s, which corresponds to Reynolds number of 100 in laminar flow range to be used for Eqs. (3) and (4). The fluid jet created τ_m ~ 30 dyn cm^{-2} which is in line with published shear stress value required to rupture protein-ligand interaction [120]. Figure 2.9B shows an image of BSA-FITC lesion created by jet impingement and a plot of non-dimensional wall shear stress as a function of non-dimensional lesion size for jet radius R_{jet} = 125 µm. With an average lesion radius of 284 µm (n = 4), the estimated shear stress required to remove BSA-FITC (τ_c) was 10.2 dyn cm^{-2}. The numerical analysis results (Fig. 2.4) showed that our magnetic microactuators can generate up to 10 dyn cm^{-2}. Taken together with the results from our jet impingement study, we expected to show a robust protein removal using our prototype GDD drainage tube.

2.7 Protein Biofouling Removal in GDD

The main function of our magnetic microactuators is to remove the protein adsorbed on the device surface and the inner wall of GDD microtube to prevent the initiation of inflammatory cascade. As such, we quantified the decrease in fluorescence intensity due to device actuation on device surface and the inner wall of the microtube as simulated in Fig. 2.10. To study anti-

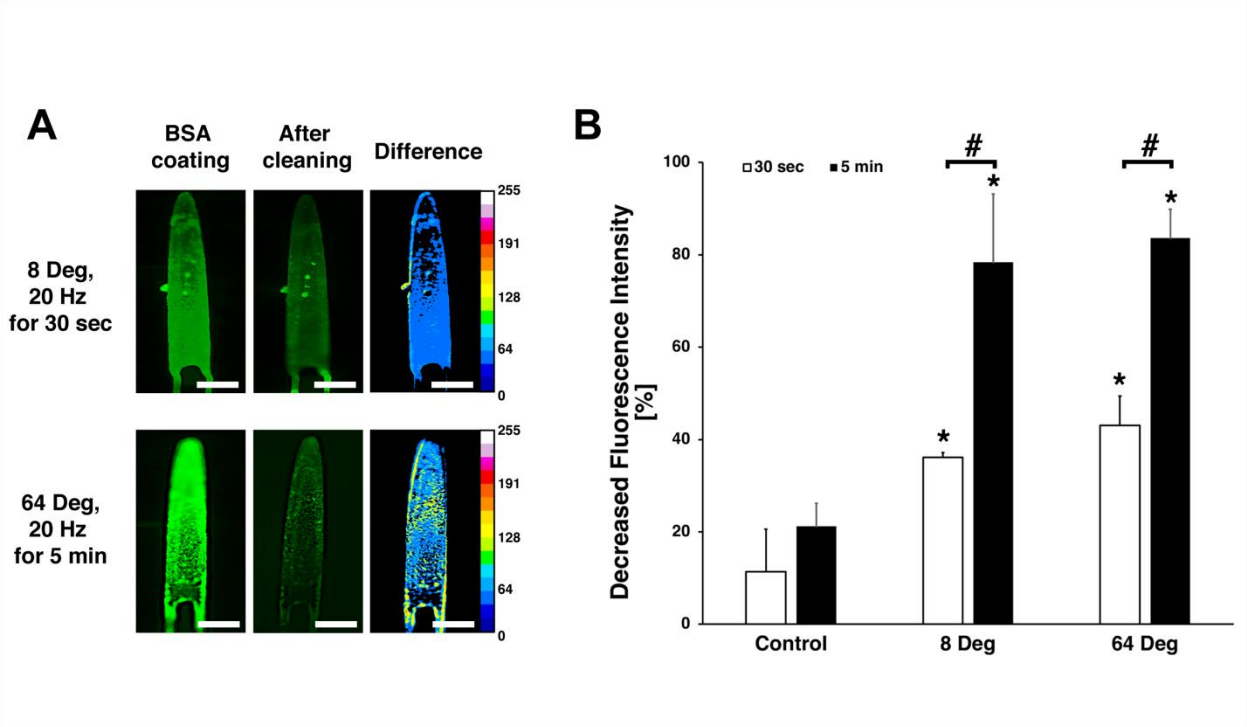

Figure 2.10: Impact of actuation amplitude and duration. (A) Fluorescence intensities (a. u.) of BSA-FITC coated microactuators before and after actuation using different deflection amplitudes and actuation duration at 20 Hz. Significant protein removal can be seen for both small and large amplitude actuation. The difference map shows a more significant protein removal with longer actuation duration. Scale bar = 200 μm. (B) Comparison of decreased fluorescence intensity (n = 3 for each actuation condition). * and # indicates statistical significance against corresponding control ($p < 0.01$)

biofouling capability of the actuator itself, we actuated BSA-FITC coated devices with different actuation durations at 20 Hz. The maximum actuation duration was set to 5 min based on prior literature and for practical consideration assuming that a shorter actuation protocol would be less burdensome on clinicians and patients [121], [122]. The minimum actuation duration was set to be 30 s, which is 10 % of the maximum actuation duration. Figure 2.10 demonstrates BSA-FITC removal due to actuation of magnetic microdevices. We compared the decreased fluorescence intensity values using one-way analysis of variance (ANOVA) with Tukey's HSD post-hoc pairwise analysis. The results showed that BSA-FITC coated on microactuators (n= 3) was significantly reduced compared to non-actuated control regardless of deflection amplitude or actuation duration ($p < 0.01$). Without actuation, the fluorescence intensity decreased by approximately 10–20% depending on treatment duration. However, the difference in fluorescent intensity between the small (8^o) and large (64^o) deflection magnitudes was not statistically

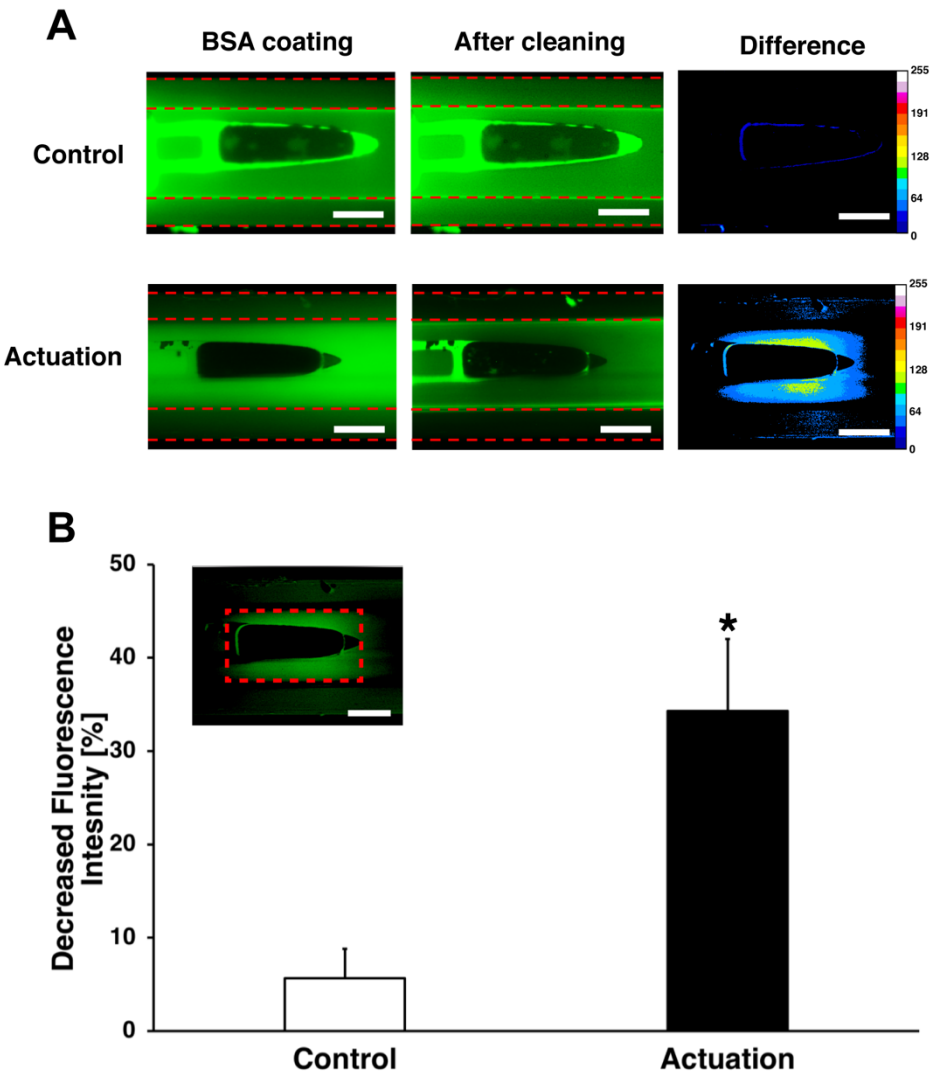

Figure 2.11: Protein cleaning in the microtube**.** (A) Fluorescence images of BSA-FITC removal using the microactuator located within the lumen of microtube with an actuation for 5 min at 20 Hz (a. u., scale bar = 200 μm). (B) The area used for measuring fluorescence intensity (red dotted box (scale bar = 200 μm) and decreased fluorescence intensity near the actuator.

30 s, BSA-FITC amount reduced by 42%. whereas up to 85% protein clearance can be seen on device when actuated for 5 min. Thus, in subsequent evaluations to determine the impact of actuation on removing protein adsorbed on the microtube inner wall, we actuated all samples for 5 min to maximize protein clearance.

To demonstrate the in situ anti-biofouling performance of our smart GDD, we coated the inner lumen of 300-μm-diameter microtube integrated with our magnetic microactuator using BSA-FITC. Figure 2.11 highlights the difference in fluorescence intensity between actuated versus non-actuated GDD prototype. Without actuation, we saw virtually no difference in fluorescence intensity. Following actuation, however, we saw a significant decrease in fluorescence intensity in areas surrounding the microdevice. The pattern of cleared area closely resembles the shear stress distribution predicted by our numerical analysis (Fig. 2.4). We then quantified the amount of fluorescence intensity decrease from the end of the beams to the actuator tip and compared the results using a two-sample t-test. The results show that the microactuation can remove significant amount of adsorbed BSA from the tube wall compared to the non-actuated control ($p < 0.01$, Fig. 2.11A). However, the decrease in fluorescence intensity (< 40%) in microtube was much smaller than the 85% decrease we saw from the device surface following a 5 min actuation (Fig. 2.11B).

To confirm that the biofouling removal process does occur via mechanical shear generated by the micro-actuation and not by the heat generated from the microactuation, we also measured the amount of heat generated during actuation (Fig. 2.12). When we actuated our microdevices (n= 4) for 5 min at 20 Hz using 40 mT in room temperature PBS, no temperature increase was seen in thermal camera images (FLIR A325sc, FLIR, Wilsonville, OR, USA). It is important to ensure that no thermal effect occurs due to microactuation since excessive heat may lead to unintended damage to the surrounding tissue.

2.8 Conclusions and Discussion

Here we demonstrated that the LCP-based micro-actuators can easily be fabricated at low-cost using our maskless photolithography. LCP is widely used polymer in biomedical applications due to their near hermetic properties, biocompatibility and superior chemical resistance [123]–[126]. By using commercially available low-cost LCP sheets as the substrate in combination of highly scalable microfabrication processes such as maskless photolithography, oxygen etching, electroplating, and polymer coating, it is possible to manufacture these LCP-based devices at

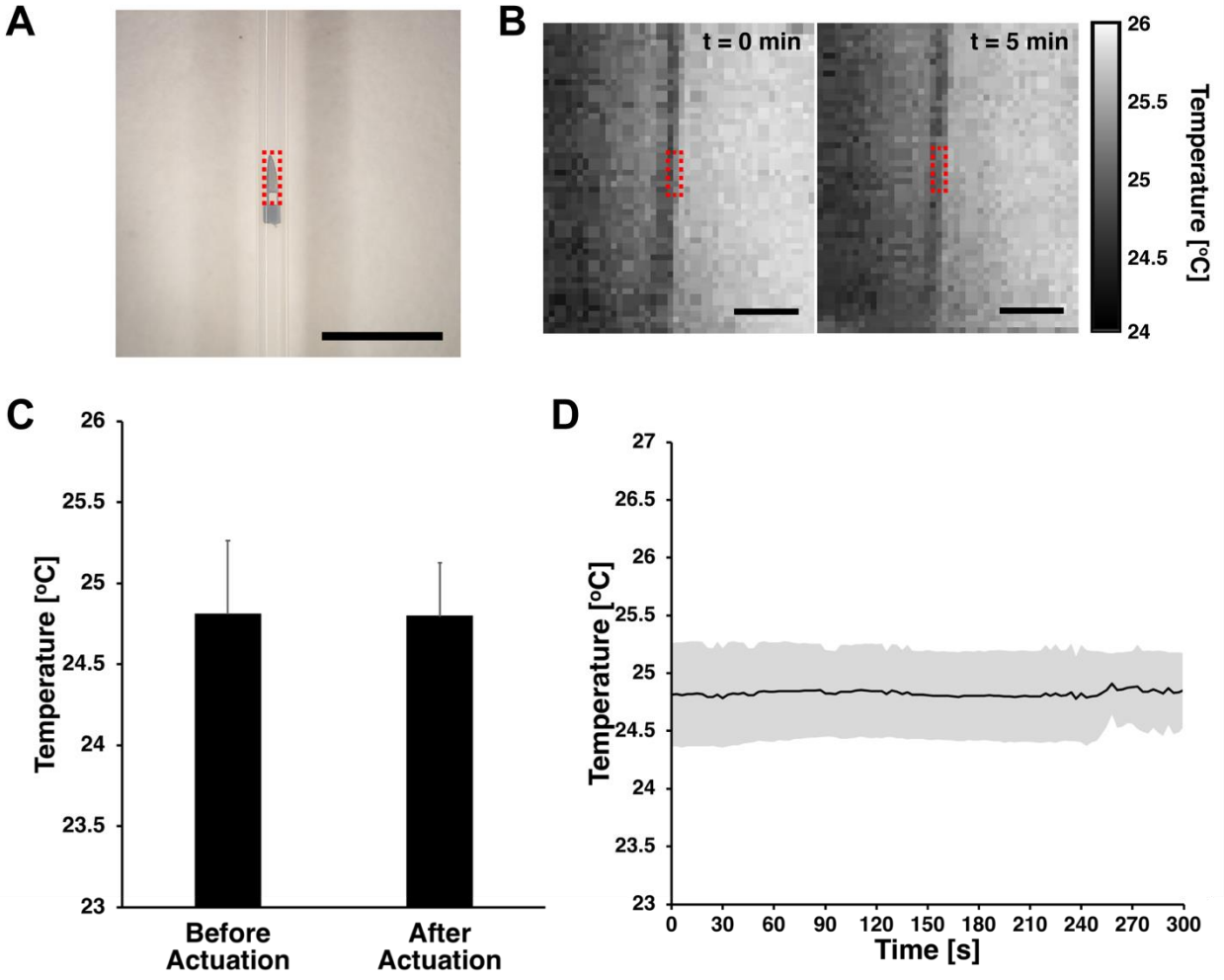

Figure 2.12: Temperature evaluations**.** (A) Photographs of a microactuator for temperature measurement. Red dotted box indicates the selected region of interest (ROI) for temperature analysis. Scale bar = 2 mm. (B) The infrared images of the ROI (the dotted red boxes) before actuation and after 5 min actuation. Scale bar = 2 mm. (C) Averaged temperature from the ROI before and after actuation (n = 4). (D) Averaged temperature from the ROI as a function of time with grey shaded error range.

extremely low costs. Moreover, the simple integration process that we employed to immobilize microdevices inside a small drainage tube may be used to create other smart MEMS-enabled catheter-based devices.

Both the static and the dynamic responses of these microfabricated LCP-based actuators corresponded well with the theoretical values, which suggests a good control of our fabrication process. The *in vitro* evaluation using BSA-FITC showed that, as expected, the actuation from our device can effectively reduce proteinaceous biofouling on the actuator surface and the inner wall

of the micro- tube. The results from the in vitro experiments demonstrated a good agreement with our results from the numerical analysis that predicted the pattern of biofilm clearance by quantifying the shear stress distribution and the jet impingement study that quantified the adhesion strength of the BSA-FITC. This approach to quantify the adhesion properties of specific biofilm and to model the shear stress profile of a device actuation may be used in future iterations to design novel microactuator arrays that are tailored for bespoke implantable application against specific biofouling materials.

The potential implication of utilizing active mechanism for combating biofouling is enormous since many chronically implantable devices including biosensors, neural interface electrodes, and drug delivery and drainage devices suffer from significant performance degradation due to biofouling [7], [97]. Although there is a number of proposed mechanisms for actively addressing biofouling using electrical and mechanical transducers [121], the magnetically-powered actuators have several key advantages. First, the magnetic device can be activated in situ wirelessly via externally applied magnetic field with low power requirements without the need for any invasive procedure. Second, the magnetic microactuators can be tailored to deliver large disruptive forces to remove multi-scale biofouling materials including protein, bacteria, and cells. Third, the lack of integrated circuit and internal power source can facilitate the integration and packaging of these type of devices into existing medical devices, which can accelerate clinical adoption. Finally, as mentioned, the simple design is compatible with many scalable microfabrication technologies that can significantly reduce the cost of manufacturing.

Despite these key benefits, there are several remaining questions to be answered. First, the amount of protein removed from the microtube wall was much lower than that from the actuator surface despite our numerical analysis demonstrating a higher maximum shear stress on the wall. This may be due to the fact that each microscope image was focused on microactuator surface, which is located at the center of the microtube. As can be seen from Fig. 2.4, the magnitude of shear stress distribution around the mid-plane of microtube is much lower than the top and bottom of the microtube. It may be interesting to characterize protein distribution using a confocal microscope in the future to verify this hypothesis. If not, it is possible to leverage our predictive modeling to redesign microactuators that can provide a greater average shear stress to ensure a more efficient protein-removal. Secondly, additional experiments are needed to determine optimum actuation duty cycle that will ensure a protein-free GDD microtube. Although the

microactuators were able to demonstrate good protein reduction in just 5 min, it may be possible to reduce this actuation duration further by performing a systematic evaluation. Thirdly, although it is possible to integrate many microactuators into a long microtube, the manual assembly process can be further streamlined if 1D arrays of microactuators are fabricated to better control the device spacing. Finally, additional in vitro and in vivo work is necessary to ascertain whether periodically removing biofilm using our self-clearing implants will actually prolong the device lifetime and improve patient outcome. A critical question to address is to determine what happens with the displaced biofouling material. A detailed histopathological evaluation using animal models must be performed to ensure that the displaced biomaterial will not cause undesirable downstream effects.

Recently, we developed a multifunctional implantable glaucoma shunt with a self-clearing capability and a pressure sensitive valve system using magnet elements embedded silicon elastomer (Fig. 2.13). This simple microfabricated devices would combat biofouling that greatly reduces functional lifetime of theses chronic implants and provide personalized pressure control to prevent hypotony-related vision threating complications. Magnet-based multifunctional glaucoma shunts are well suited for this application for several reasons. First, they do not require an integrated power supply, control electronics, or wires, which eliminates the need for stringent hermetic packaging necessary inside the body. Second, they can be driven by a remote source of magnetic field. Lastly, the magnetic valve can open and close the microchannel for aqueous humor without external electric circuit, which makes magnetic valve ideal for reducing a risk of hypotony

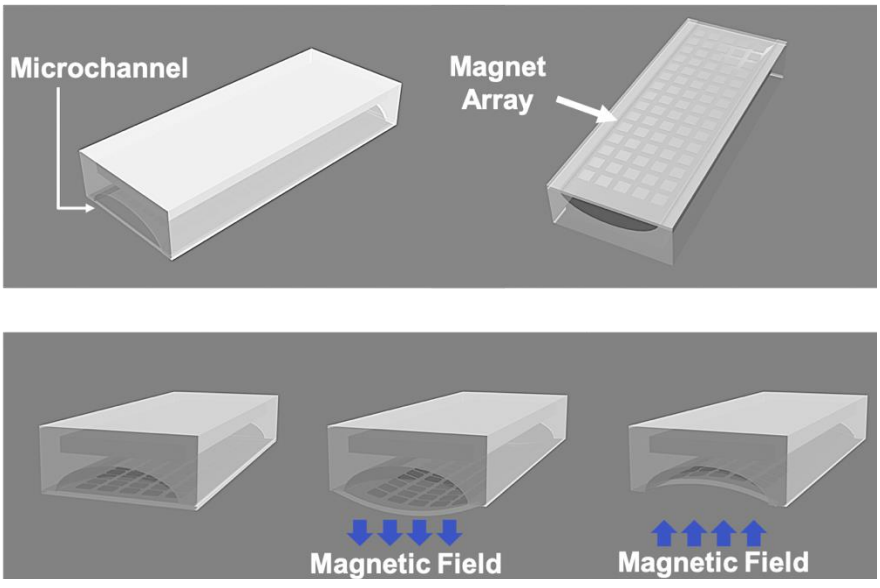

Figure 2.13: 3D schematics of the glaucoma shunt with magnet blocks embedded in the PDMS membrane.

by poor IOP control. we fabricated PDMS based microchannel integrated with micromagnet array embedded thin film PDMS layer in order to clean the whole channel by actuating bottom layer of the microchannel. Although additional characterizations are necessary to determine its cleaning capability, we have little concern due to increased out-of-plane deflection and compliance of this PDMS actuator. Direction of the functional membrane deflection was successfully controlled by changing the direction of an external magnetic field.

3. DEVELOPMENT OF FRACTAL MICROELECTRODES FOR ENERGY EFFICIENT NEUROSTIMULATION

3.1 Introduction

Electrical stimulation of the nervous system is used ubiquitously to replace and restore lost bodily functions in patients with a number of neurological impairments including neuromotor deficit [127], vision and hearing loss [128], [129], chronic pain [130], and epilepsy [131]. In 2015, the total market size for various implantable neural stimulation devices that target spinal cord, cochlear, cerebral cortex, and other peripheral nerves (e.g., Sacral, Vagus nerve), exceeded $4.9 billion with the annual growth rate of 17% [132]. The increasing popularity for neurostimulation has fueled the demand for more precise targeting of neural substrates. For example, vision prostheses now feature more than 1000 stimulating microelectrodes with a diameter of 100 μm, and manufacturers of cortical stimulation devices have begun to create higher density electrodes for stimulating various deep brain structures [133]. The advances in microfabrication technologies has made it possible for researchers to investigate feasibility of high density micros- cale electrode arrays even with more complex geometries [134]–[138]. While it is relatively easy to design, and manufacture smaller stimulating electrodes, doing so can functionally limit the amount of electrical charge that can be delivered through smaller surface area.

Moreover, the reduction in electrode size also increases the overall electrical load of battery-powered stimulation systems. A conventional implantable neural stimulation system, which consists of three major components: implantable pulse generator (IPG), electrical leads, and neurointerfacing electrodes, have average lifetime of 4–6 years [139]. Although the lifetime of these chronically implanted systems differ widely depending on individualized stimulation parameters and usage, minimizing the electrical load is imperative for ensuring long-term utility of these systems [140], [141]. Therefore, enhancing the resolution of stimulation using smaller microscale electrodes requires a careful consideration on overall impact of electrode design in terms of stimulation performance as well as its impact on device longevity.

There are significant efforts in the field to increase the efficiency of neurostimulators by decreasing microelectrode impedance or increasing the charge transfer capability. For instance, electrode material and the surface morphology were found to have significant impact on electrochemical impedance and charge transfer capac- ity. Iridium oxide (IrOx) electrodes have

been studied widely to show superior charge injection capability than Pt-based electrodes [142], [143]. Similarly, researchers have also touted poly(3,4-ethylenedioxythiophene) (PEDOT) for having a higher charge injection limit than Pt and IrOx electrodes [144]. However, PEDOT has been reported to shows mechanical failure such as delamination and cracking during chronic stimulation [145]. Despite many groups working to develop higher performing microelectrodes using various electrode materials, platinum (Pt) remains as the gold-standard for commercial neurostimulation devices, especially for cortical stimulation. In terms of morphology, researchers have explored various fabrication methods to improve performance of electrodes. De Haro et al., demonstrated that electroplated Pt has lower impedance and higher corrosion resist- ance than sputtered Pt, which can improve the lifetime of the microelectrode [146]. Sputtered material such as IrOx and titanium nitride have been demonstrated to be superior than evaporated IrOx due to difference in nanoscale surface morphology [142], [143]. Shota et al., showed that microelectrode composed of IrOx and Pt-black with nanoscale roughness has a lower impedance and high charge-injection capability than flat microelectrode [147]. Boehler et al., reported that Pt microelectrode with nanograss structure has reduced impedance and strong adhesion to metal- lized substrate [148].

The impact of electrochemical performance on electrodes with high perimeter-to-surface area (PSA) has also been well documented [149]–[151]. Electrochemical impedance spectroscopy (EIS) from circular microscale electrodes with different diameters showed that smaller microelectrode corresponded to a higher impedance, which can be attributed to an increase in the solution resistance and shorter charging time of capacitive double-layer on electrode [152]. Grill et al., reported that conventional deep brain stimulation electrodes split into smaller segments with higher PSA ratios have higher stimulation efficiency and smaller energy load for IPGs despite showing no significant differences in impedance between single electrode and segmented ones [153]. Cogan et al. confirmed that increasing the PSA ratio of the IrOx microelectrode lowered the electrode impedance and improved the charge injection limit perhaps due to reduction in access resistance and increasing ion flux to the electrode surface [154]. These reports suggest that increasing the PSA may be an effective way of improve electrode performance.

One easy way to achieve high PSA in a small footprint is to use fractals. For this reason, fractal designs have been used widely in antennae designs to achieve multi-band capability and to reduce size [155]–[158]. Recently, several groups have begun to explore the utility of fractal

designs in neurostimulation as well. Golestanirad et al. reported a numerical model of modified Sierpinski carpet electrode that requires 22% less energy to activate a given population of neurons [159]. Most recently, another group reported similar results using a numerical model of an electrode with branching fractal design that can penetrate deeper into the neural substrate compared to Euclidean electrodes, suggesting better neurostimulation performance [160]. Compared to conventional Euclidean electrode geometry, which results in a significant current density gradient across the electrode surface [161], [162], fractal electrodes are able to deliver a more uniformly high current density across the surface [160]. However, all of the published work to date focused on numerical analyses of various fractal designs without systematic electrochemical evaluations. Two important questions remain to be explored: (1) do fractal electrodes exhibit similar charge injection limit improvement as shown in high PSA electrodes? and (2) by what mechanism?

In this work, we electrochemically examined the role of electrode geometry in terms of PSA ratio and shape using custom microfabricated electrode arrays. Four types of electrodes with identical surface area but varying PSA ratios were created: circular, fractal, serpentine I, and serpentine II (Table 3.1). The circular electrodes with 100 μm diameter was chosen as a representative Euclidean design with the lowest PSA ratio. The fractal and ser- pentine I electrodes were designed to have the same PSA ratio to explore whether different shapes would have an impact on electrochemical performance of microelectrodes. Serpentine II electrode had the highest PSA ratio. Serpentine designs were used for their space-filling capacity and potential utility in flexible bioelectronics [163]–[165]. Based on prior literature, we expected to show increased electrode performance with increasing PSA regardless of the electrode shape.

Using numerical modeling, we quantified the total charge injected and the current density around the microelectrodes. We evaluated the electrochemical performance of each electrodes using cyclic voltammetry, EIS, and voltage transient analysis. The cathodal and the total charge storage capacity of each electrode were calculated from the time integral of the current in cyclic voltammogram, which is related to the charge injection capability of electrode. The EIS measurements were performed in phosphate buffered saline to characterize capaci- tive and non-Faradaic processes. Additionally, we used ferri-ferrocyanide red-ox pair as a probe to characterize mass-transport to the electrodes associated with Faradaic processes that occur during charge injection with electrical stimulation [166]. To investigate the effects of the geometry on charge

injection limit, we compared the maximum negative potential excursion and the maximum driving voltage of the different shaped microelectrodes using voltage transient analysis with different charge injection levels. Finally, the energy consumption from different microelectrodes was quantified from the cathodic potential transient and the applied current waveform. Our results indicate that the electrode shape may play a more significant role in charge injection capability of microelectrodes than previously reported. We found that fractal microelectrodes exhibit markedly superior electrode performance than other PSA-matched microelectrodes. Here we provide empirical evidence to suggest that the improved microelectrode performance in non-Euclidean electrodes may be due to lower access resistance and more efficient mass-transport in high PSA and fractal electrodes. Furthermore, these results suggest the possibility of further design optimization towards more energy efficient stimulating electrodes that may enable more reliable chronic electrical neuromodulation.

3.2 Device Design and Numerical Modeling of Current Density Distribution

To examine the electrochemical role of electrode geometry in terms of PSA ratio, we designed four types of electrodes with identical surface area but varying PSA ratios were created: circular, fractal, serpentine I, and serpentine II. A description of the Pt electrode geometries is provided in Table 1. The geometries of non-Euclidian electrodes were designed to match the surface area from circular shaped microelectrode with a diameter of 100 μm (7854 μm^2) (Fig. 3.1). In Vicsek fractal, the area (A_n) and perimeter (P_n) at iteration n can be described using $A_n = l^2 \cdot 5^n$ and $P_n = 5P_{n-1} - 8l$ with l as the length of the initial square. Based on the area of circle microelectrode (7854 μm^2) and the resolution limit for microfabrication, the side of the smallest square unit of the fractal (l) was set to be 7.93 μm with n = 3. The fractal and serpentine I electrodes were designed to have the same surface area as well as the perimeter to explore whether different shapes would have an impact on electrochemical performance of microelectrodes. The desired PSA in serpentine electrodes were achieved by adjusting the radius of curvature and the length of straight portions. Fractal shape and serpentine I shape had approximately 6.35 times longer perimeter than the circular electrodes while serpentine II electrodes had 10 times longer perimeter. Serpentine II electrode had the highest PSA ratio. Serpentine designs were used for their space-filling capacity and potential utility in flexible bioelectronics. Based on prior literature, we expected to show increased electrode performance with increasing PSA regardless of the electrode shape.

Table 3.1: Dimensions of the microelectrodes

	Circle	Fractal	Serpentine I	Serpentine II
Perimeter [mm]	**0.3142**	**1.998**	**1.998**	**3.156**
Area [mm^2]	**7.854×10^{-3}**	**7.854×10^{-3}**	**7.854×10^{-3}**	**7.854×10^{-3}**
Perimeter/Area [mm^{-1}]	**40**	**254**	**254**	**400**
Footprint [L × W]	**D = 100 µm**	**157 µm × 157 µm**	**94 µm × 148 µm**	**126 µm × 130 µm**

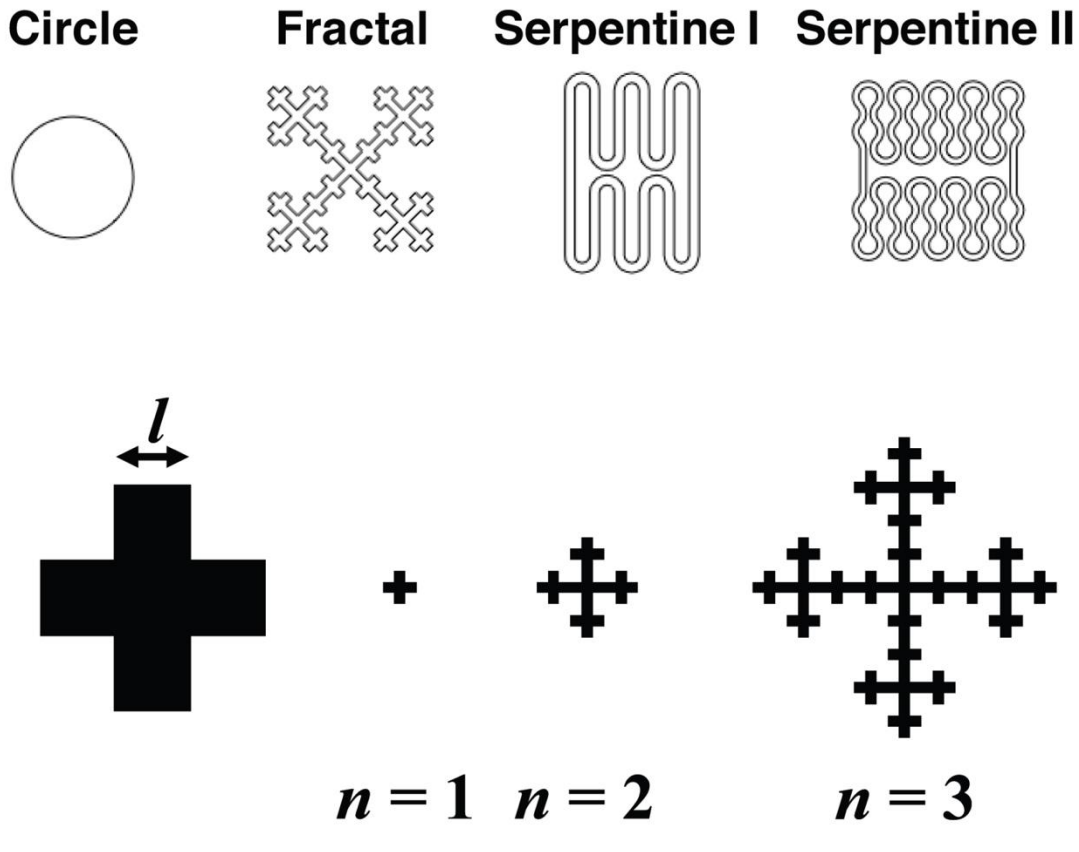

Figure 3.1: Planar geometry with different shapes and Vicseck fractal design parameters at different iteration levels with the minimum feature size *l*.

microelectrodes surface using numerical modeling. The impact of the water window potential of the Pt (−0.6 V) on the four electrode designs was examined using AC/DC module in 3D COMSOL

model. The impedance of each electrode design was also modeled in COMSOL using 10 mV AC voltage perturbation from 10 Hz to 100 kHz.

The electric current mode solved the charge conservation equation for calculating current density distribution across the internal boundaries below:

$$\nabla J + \frac{\partial \rho}{\partial t} = 0$$

where J is the current density, and ρ is the charge density. The current density is governed by the equations below:

$$J = \sigma E = -\sigma \nabla V$$

$$\nabla \cdot J + \frac{\partial \rho}{\partial t} = \nabla^2 V = 0$$

with the electrical potential V. The electric currents mode ignores any Faradaic reactions that occur on the elec- trode surface. The model includes microelectrode domain, extracellular boundary with cylindrical shape, and five hemi-sphere domains with radius from 200 μm to 1200 μm to estimate current density distribution and total delivered current around the electrode (Fig. 3.2). The conductivity of simulated domain was 0.2 S m^{-1} to matched the brain tissue conductivity. The electric potential of −0.6 V was applied to electrode surface to simulate the cathodic limit of water window. The calculation of impedance in frequency domain were made from 10 Hz to 100 kHz by applying 10 mV AC voltage perturbation to electrode surface. The cylindrical outer boundary was grounded at 0 V, and the model was meshed using tetrahedral mesh elements.

The electrochemical process including chemical reacn because the mathematical handling of electrochemical reactions from non-uniform current density along irregular geometry is difficult

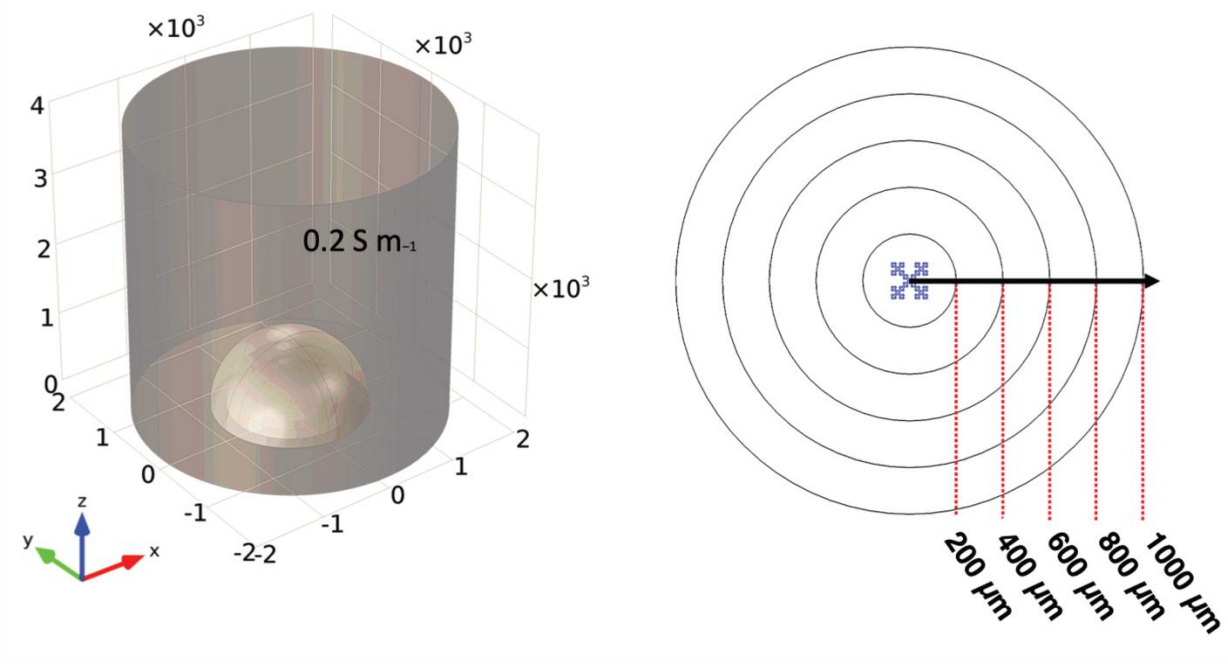

Figure 3.2: The finite element model with constant voltage.

to model accurately [167]. Therefore, most modeling studies have focused on the simulation of the Faradaic process on the simple circular shaped microelectrodes with limited conditions such as just one red-ox pair with the parameters from simplified chemical reaction assumption [168], [169]. However, the numerical simulation for non-Faradaic process without consideration of mass transfer kinetics are widely utilized because it can still provide insight on solution resistance, charge transfer resistance, double layer capacitance and electrical stimulation efficiency for various electrode geometries [170], [171]. Fig 3.3A shows that the fractal design produces the highest current density around the microelectrode, followed by other shapes in the order of perimeter-to-area ratio. The average current density followed the same trend with the fractal electrode having highest value at all distances away from the electrode surface. The fractal electrode was able to inject the highest amount of current of 267 µA compared to 172 µA for the circular electrode (i.e., 55% increase) ((Fig. 3.3B). The serpentine II and serpentine I electrodes delivered the current of 264 µA and 250 µA, respectively (Fig. 3.3C).

Fig 3.3D shows the impedance calculated for each microelectrode design. Typically, the impedance at high frequency (>10 kHz) corresponds to the solution resistance while the impedance

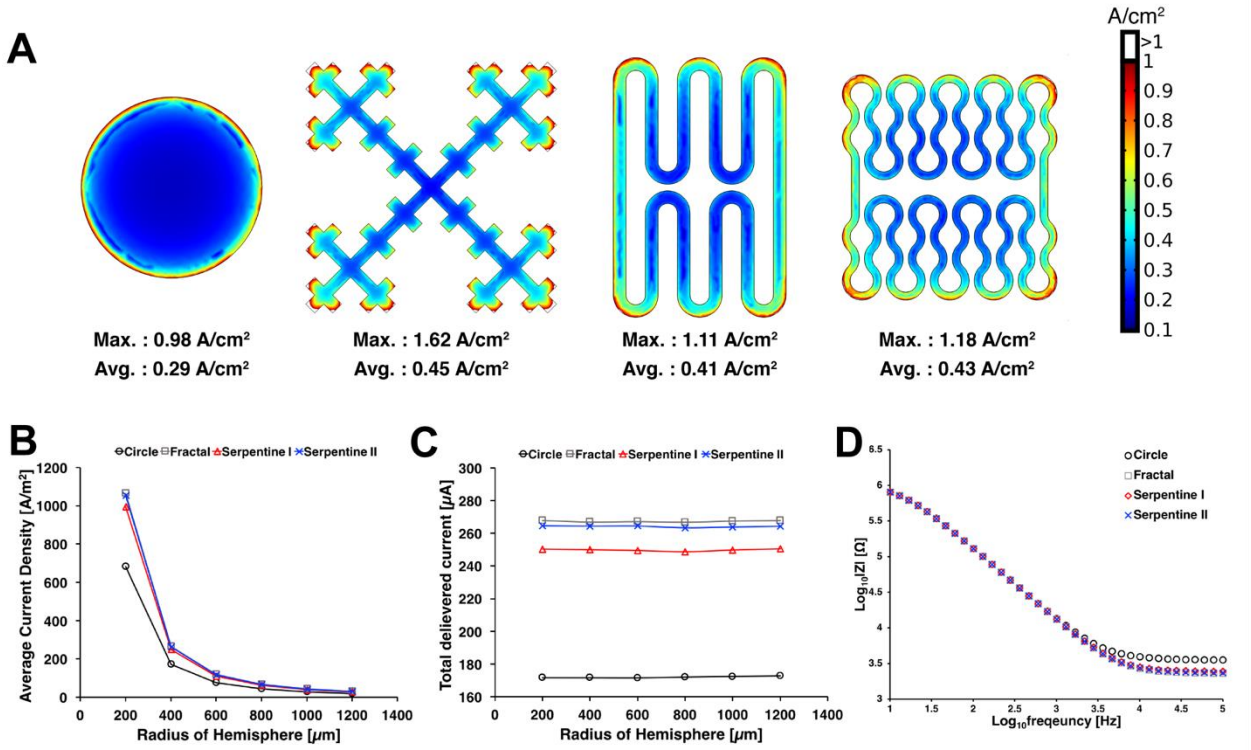

Figure 3.3: The current density distribution of different electrode design using the voltage-control stimulation (−0.6 V). (A) The current density surface plot for each microelectrode design. Both the maximum and the average current density across the electrode surface was highest for the fractal design followed by serpentine II, serpentine I, and circular electrode. (B) Average current density as a function of distance away from each electrode center. (C) The total delivered current on hemispheric boundaries. (D) Simulated impedance Bode plot of each microelectrode design.

at low frequency are affected by the charge transfer resistance and the diffusion-limited Faradaic processes. In our simulation, the fractal design had the lowest impedance at 100 kHz, followed by serpentine II, serpentine I, and the circular design. This result corresponds to the same trend found for the average current density (Fig. 3.3B) and the total delivered current (Fig. 3.3C), which suggests that lower solution resistance may be responsible for better charge injection capacity. At lower frequency (10 Hz), the impedance of each electrode design was not significantly distinguishable from each other, which reflects the lack of Faradaic components.

3.3 Electrode Fabrication

Figure 3.4A and B show the fabricated microelectrodes and overall fabrication flow. Platinum microelectrode of varying PSA were fabricated on 500 nm film of silicon nitride layer by plasma

enhanced chemical vapor deposition (Axic, Milpitas, CA, USA). A photoresist (AZ1518, MicroChem, Newton, MA, USA) was spincoated over the silicon nitride layer and patterned to define microelectrode designs with different shapes. Pt film (100-nm-thick) was deposited on to the photoresist using a titanium (10 nm) as an adhesion layer. The electrode arrays were created using lift-off process. A 1.5-μm-thick layer of polyimide (PI-2545, HD Microsystems, Parlin, NJ) was spin-coated over the wafer and cured as the insulation layer. The microelectrodes, counter electrode, and contact pads were created by reactive ion etching (RIE) with 20 sccm O_2 at 100 W in 50 mTorr for 10 min using photoresist (AZ9260, MicroChem, Newton, MA, USA) as the etch mask.

3.4 Electrochemical Characterization

We evaluated the electrochemical performance of each electrodes using CV and EIS. CV and EIS were performed using a custom microelectrode packaging platform (Fig. 3.4D). CV was measured using a commercial potentiostat (SP-200, Bio-Logic.Inc, Seyssinet-Pariset, France) in a standard three-electrode configuration using KCl saturated Ag/AgCl (RE-1CP, ALS Co., Ltd, Tokyo, Japan), along with the working and counter electrodes on the microelectrode array. CV was performed in phosphate-buffered saline solution (PBS) having composition of KH_2PO_4 1.1 mM, NaCl 155 mM, and $Na_2HPO_4 \cdot H_2O$ 3 mM with pH 7.4 (ThermoFisher Scientific, Waltham, MA, USA). All CV were measured at sweep rate of 50 $mV \cdot s^{-1}$ between potential range of - 0.65 V and 0.85 V versus Ag/AgCl reference electrode. EIS measurements were obtained using the same experimental setup. The perturbation potential was sinusoidal 10 mV excitation voltage with the frequency range from 10 to 100 kHz.

Figure 3.5A shows CV responses of the microelectrodes with different shapes measured in PBS from −0.65 V to 0.85 V at a sweep rate of 50 $mV \cdot s^{-1}$. The voltammographs show that the

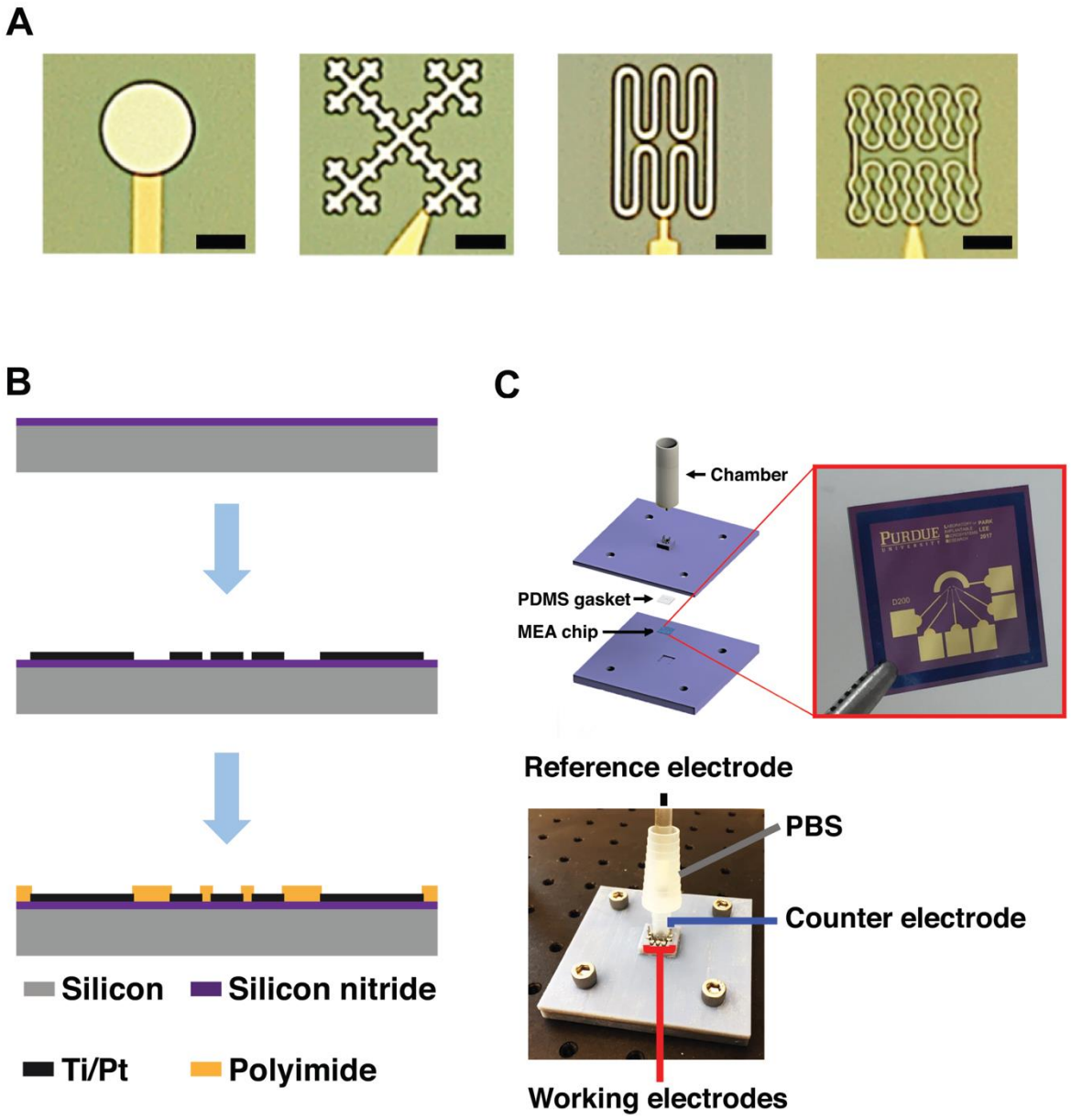

Figure 3.4: Electrode Fabrication. (A) Optical micrographs of the fabricated microelectrodes. Sale bars = 50 μm. (B) Fabrication sequence of microelectrode arrays: deposition of 500 nm silicon nitride: evaporation of Ti/Pt; and polyimide passivation layer coating followed by RIE for opening. (C) Experimental setup with 3D printed fixture to accommodate the microelectrode arrays for electrochemical measurements

fractal, serpentine I, and serpentine II electrodes with higher perimeter-to-area ratio all have lower cathodic current density than the circular electrode. From the voltammographs, we

calculated the total and cathodal charge storage capacities (CSC) of each electrodes using the following equation [142]:

$$CSC = \frac{1}{vA}\int_{E_c}^{E_a} |i| dE \ \ (C/cm^2)$$

with the potential versus Ag/AgCl reference electrode *E*, the measured current *i*, the positive and negative potential range E_a and E_c, the surface area of the microelectrode *A*, and the scan rate *v*. For cathodal stroage capacity (CSC_c), only the cathodic current was used for calculation, and both anodic and cathodic currents were used for total charge storage capacity (CSC_t). The average CSC_c and CSC_t for each electrode design are shown in Table 2. The CSC_c and CSC_t of the electrodes were compared using one-way ANOVA with Tukey's HSD post-hoc analyses. The results indicated that the CSC_c and CSC_t of circular microelectrode were significantly smaller than the other microelectrodes with higher perimeter-to-area ratio ($p < 0.01$) (Fig. 3.5B). In contrast with the FEM result, serpentine II electrodes had the highest CSC values rather than the fractal design although the difference between the two were not statistically significant (Table 3.2). Interestingly, CSC values for fractal electrodes were significantly higher than serpentine I electrodes even though they share the same PSA and SA, which suggests that the electrode shape may have a significant impact on electrode performance.

Figure 3.6A shows representative impedance spectra of each microelectrode design in PBS. Although there were relatively small differences, the high PSA electrodes exhibited lower impedance at high frequency. At lower impedance, however, the circular microelectrode had the lowest impedance. The difference between simulated and measured impedance values are listed shown in Fig 3.6B – E and Table 3.3. Unlike the Bode plot, the Nyquist representation of EIS data showed significant differences between electrodes (Fig. 3.7). Using Randle's circuit as an equivalent model (Fig. 3.7B, the values of solution resistance R_s, the charge transfer resistance R_{CT}, and the double layer capacitance C_{dl} were estimated. The fractal electrode had the lowest R_S and R_{CT}, and the highest C_{dl} (Table 3.4). To distinguish the impact of mass transport on microelectrode performance, EIS was performed again in ferri-ferrocyanide, which is electrochemically reversible analyte with differing charges and relatively large ion size [166]. EIS measurements were repeated using 10 mM solution of analyte ($Fe(CN)_6^{-3/-4}$) in 0.1 M KCl (Fig.

3.8). AC voltage perturbation of 30 mV was applied at the working electrode using sinusoidal signal from 10^{-2} Hz to 100 kHz at the equilibrium voltage 0.22 V vs. Ag/AgCl sat. The EIS data were recorded at 7 points per decade. The Bode plot showed that each microelectrode has different impedance at low frequency range (<10 Hz) in which the impedance is dominated by mass transfer kinetics (Fig. 3.8A). Figure 3.8B shows the Nyquist plot with two identifiable semi-circles corresponding to different electrochemical processes. The diameter of the larger loop represents the charge transfer resistance whereas the smaller second loop indicates the impedance due to the diffusion of electroactive species to the electrode surface. The Nyquist plots were fitted with an equivalent circuit model (Fig. 3.8C) to extract the values of R_S, R_{CT}, C_{dl}, the Warburg coefficient W, and the nonlinear resistance related to hemi-spherical diffusion R_{NL}. The estimated values of each parameter from different electrode designs (n = 5 each) indicated that the fractal electrodes have the lowest R_S, R_{CT}, W, and R_{NL}, and the highest C_{dl}, which suggests that the fractal design has substantially lower overall resistance due to both Faradaic and non-Faradaic processes (Table 3.5 and Fig 3.9).

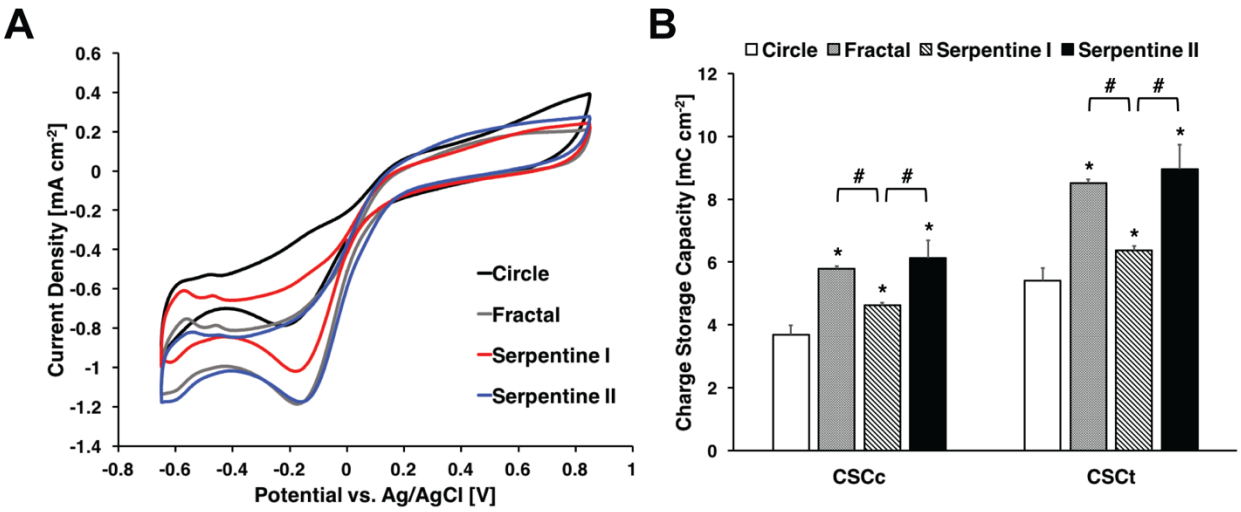

Figure 3.5: Cyclic Voltammetry. (A) Comparison of representative cyclic voltammogram of Pt microelectrodes in PBS. (B) Charge storage capacity of each microelectrode (n = 5 for each). ANOVA results revealed significant differences ($p < 0.01$) as compared to circular electrodes (*), and significant differences ($p < 0.01$) between fractal and serpentine I, serpentine I and serpentine II.

Table 3.2: CSC_c and CSC_t of each microelectrode.

		Circle	Fractal	Serpentine I	Serpentine II
CSC [mC cm^{-2}]	CSC_c	3.69 ± 0.31	5.79 ± 0.10	4.62 ± 0.10	6.13 ± 0.55
	CSC_t	5.42 ± 0.39	8.51 ± 0.13	6.37 ± 0.13	8.94 ± 0.79

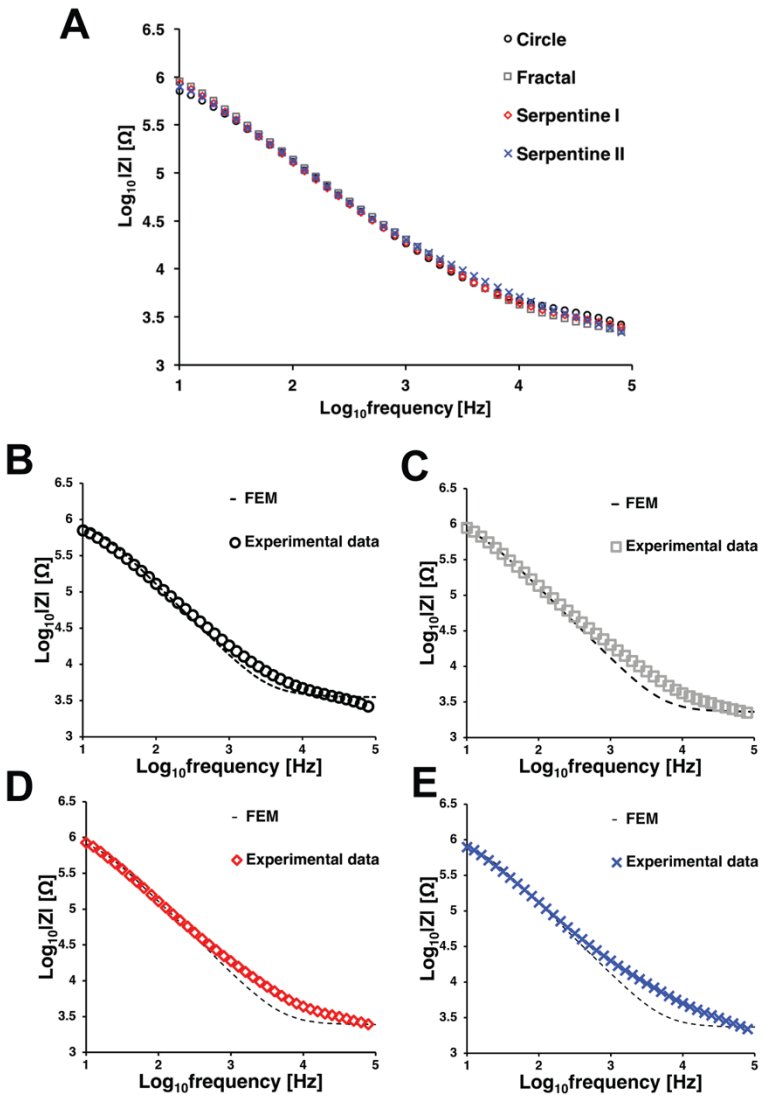

Figure 3.6: The impedance magnitudes simulated by FEM and EIS experimental data. (A) Circle, (B) Fractal, (C) Serpentine I, and (D) Serpentine II.

Table 3.3: Comparison of the impedance from experiment and COMSOL simulation (Unit: [Ω])

Frequency	Method	Circle	Fractal	Serpentine I	Serpentine II
10 Hz	Simulation	1.038×10^6	1.037×10^6	1.036×10^6	1.032×10^6
	Experiment	0.708×10^6	0.899×10^6	0.873×10^6	0.816×10^6
	Error [%]	31.80	13.23	15.71	20.92
1 kHz	Simulation	1.356×10^4	1.323×10^4	1.324×10^4	1.318×10^4
	Experiment	1.568×10^4	1.703×10^4	1.641×10^4	1.724×10^4
	Error [%]	15.58	28.68	23.87	30.79
100 kHz	Simulation	3540	2306	2454	2336
	Experiment	2402	2080	2267	1984
	Error [%]	32.13	9.781	7.609	15.06

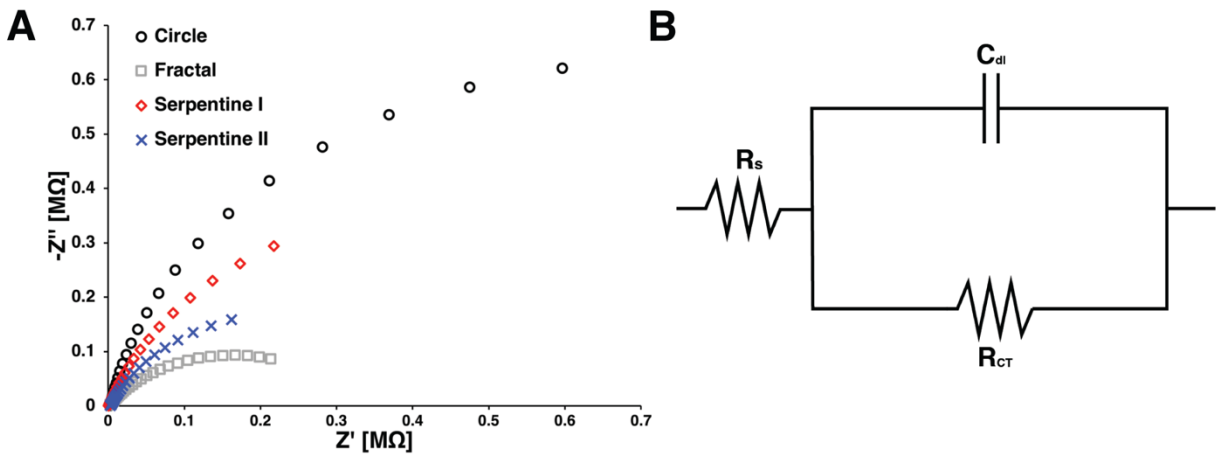

Figure 3.7: Figure 3.8 (A) Nyquist plot of microelectrodes. (B) Randle's circuit for equivalent circuit model analysis.

Table 3.4: Estimated parameters of equivalent circuit model for each electrode in PBS.

	R_s [Ω]	R_{CT} [MΩ]	C_{dl} [nF]
Circle	3050 ± 141.3	3.032 ± 0.203	14.1 ± 0.209
Fractal	1066 ± 402.4	1.379 ± 0.944	22.7 ± 0.162
Serpentine I	2304 ± 193.6	2.762 ± 0.473	17.3 ± 0.156
Serpentine II	1609 ± 251.8	2.269 ± 0.218	19.3 ± 0.073

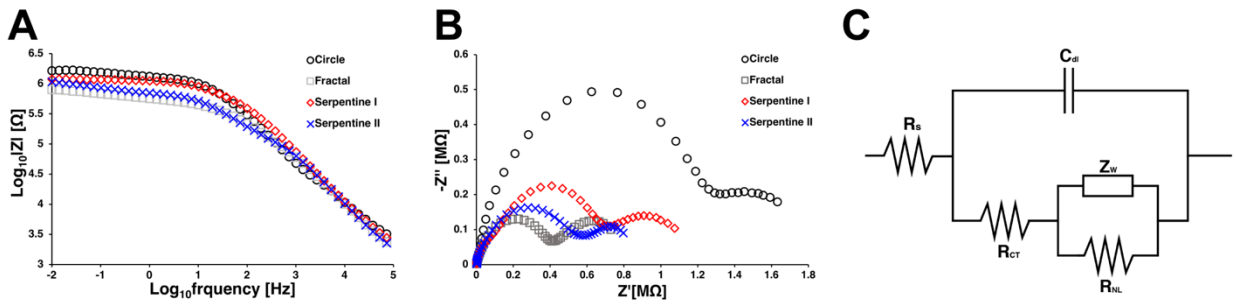

Figure 3.8: (A) The impedance spectra of microelectrodes in a 10 mM ferri-ferrocyanide + 0.1 M KCl solution. (B) Nyquist plot of microelectrodes in a 10 mM ferri-ferrocyanide + 0.1 M KCl solution. (C) Modified Randle's circuit for equivalent circuit model analysis.

Table 3.5: Estimated parameters of equivalent circuit model for each electrode measured in 10 mM potassium ferri-ferrocyanide + 0.1 M KCl.

	Rs [Ω]	**R_{CT} [MΩ]**	**C_{dl} [nF]**	**W [$M\Omega \cdot s^{-1}$]**	**R_{NL} [kΩ]**
Circle	1666 ± 14	2.08 ± 0.017	12.3 ± 0.805	3.46 ± 0.218	1004 ± 143.1
Fractal	475 ± 10	0.762 ± 0.147	50.1 ± 11.5	0.131 ± 0.042	467.2 ± 146.6
Serpentine I	723 ± 64	1.37 ± 0.140	29.4 ± 1.36	2.43 ± 0.173	681.6 ± 2.914
Serpentine II	550 ± 40	1.05 ± 0.551	16.1 ± 1.01	1.53 ± 0.623	567.5 ± 367.2

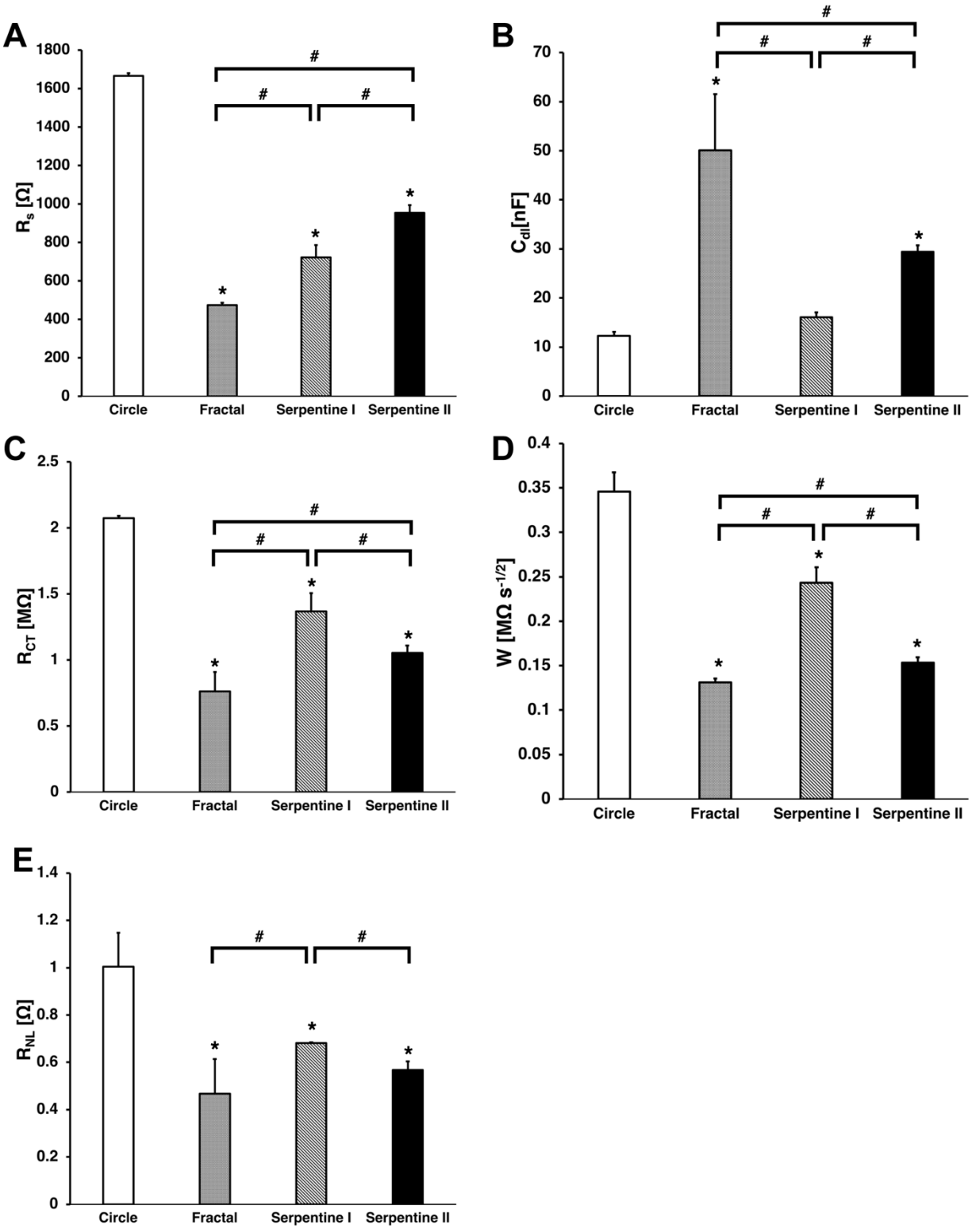

Figure 3.9: Fitted values (R_s, C_{dl}, R_{CT}, W, and R_{NL}) of each microelectrode (n=5 for each).ANOVA results revealed significant differences ($p<0.05$) as compared to circular electrodes (∗), and significant differences ($p<0.05$) between fractal and serpentine I, serpentine I and serpentine II.

3.5 Voltage Transients

The voltage transient responses from the four electrodes (n = 5 each) were compared using constant current pulses at five different amplitudes (2 nC, 4 nC, 10 nC, 30 nC, and 50 nC per phase) at a frequency of 50 Hz (Fig. 3.10). The potential in the interphase region was 0 V versus Ag/AgCl sat. As can be seen in Fig. 5E, the fractal electrodes did not reach the −0.6 V water window limit until 30 nC/phase whereas all other electrodes exceed the water window by then. The voltage transient measurements using a charge-balanced biphasic current-controlled waveform were performed with an analog stimulus isolator (AM 2200, AM Systems, Sequim, WA, USA). A bespoke MATLAB program (R2016a, Mathworks, Natick, MA, USA) was used to generate stimulating waveform with specific pulse width, amplitude, and frequency. The pulses were injected into the electrode-electrolyte test cell, and a data acquisition board (NI USB-6353, National Instruments, Austin, TX, USA) was used to record the voltage transient responses. The charge-balanced biphasic pulse used in the experiments were cathodic-first current pulse with 100 μs duration followed by 100 μs inter-phase delay. The stimulating frequency was set at 50 Hz. The maximum negative potential excursion (E_{mc}) was esteimated to be the potential immediately after the end of the cathodic pulse (Fig. 3.10A). The time delay at which the current becomes zero was measured to be approxmiately 12 μs, and E_{mc} was recorded at 12 μs following the end of the cathodic current pulse. V_{dr} is the negative driving voltage which is maximum voltage to deliver the cathodic current

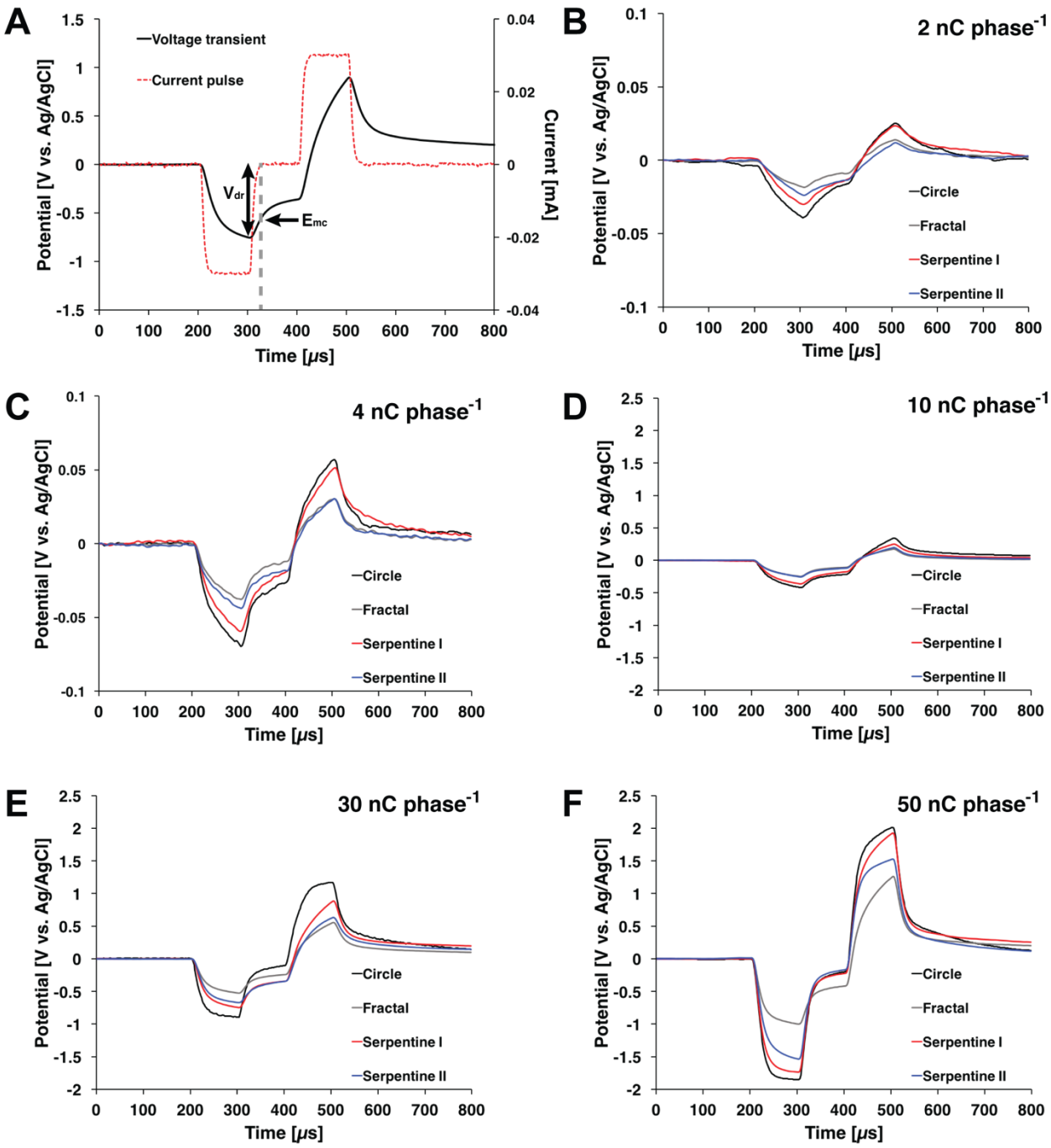

Figure 3.10: Voltage transients. (A) Representative voltage transient of microelectrode with biphasic, symmetrical current pulse was applied at 50 Hz highlighted with maximum negative potential excursion (E_{mc}) and maximum driving voltage (V_{dr}). (B–F). Comparison of the voltage-transient responses of different microelectrodes at various total charge per phases (n = 5 for each). Overall, the fractal design had the lowest E_{mc} and V_{dr}.

pulse. The maximum negative potential E_{mc} is another way to estimate charge injection capacity of a stimulating electrodes. From the voltage transient response, E_{mc} can be estimated as the electrode potential at the end of cathodic current pulse [154].

A comparison of the E_{mc} for the four electrode designs is shown in Fig. 3.12A and 3.13. In general, the fractal electrodes had the lowest E_{mc}, followed by serpentine II, serpentine I, and the circular electrodes, which suggests highest charge injection capacity for the fractal design. Post-hoc pairwise comparison ($p < 0.01$) using Tukey's test indicated that the fractal electrodes had statistically lower E_{mc} than all other electrodes at any charge injection level except against serpentine II at 10 nC/phase. Similarly, serpentine II electrodes were had statistically lower E_{mc} than serpentine I or circular electrodes except against serpentine I at 50 nC/phase. Serpentine I electrodes had statically lower E_{mc} than circular electrodes at all charge injection levels. The maximum driving voltage (V_{dr}) is the highest potential required to deliver the current pulse. The lower V_{dr} indicates that less energy is required to deliver a given charge to electrode surface. Figure 3.12B shows different V_{dr} required to deliver different charge levels to the four electrode designs under evaluation. One-way ANOVA with post-hoc pairwise comparison using Tukey's test showed that the fractal electrode needed the lowest V_{dr} than any other electrodes at any charge injection levels. However, there was no significant difference between V_{dr} of serpentine I and circular electrode at 10 nC/phase. Similar to E_{mc} results, despite having the highest PSA ratio, the V_{dr} of serpentine II electrodes were significantly higher than fractal electrodes, which suggests that there may be additional geometric effects that influence electrode performance.

3.6 Energy Consumption

The energy required to apply a cathodal pulse is described by the equation below (Foutz et al. 2012):

$$E_{load} = \int_0^{PW} I_{stim} V_{load} dt$$

where E_{load} is the energy consumed in the electrode and the solution, I_{stim} is the current amplitude for the pulse, V_{load} is the load voltage, and PW is the pulse-width. A comparison of the energy needed to apply the various current amplitudes is shown in Fig. 3.13. The fractal electrode needed

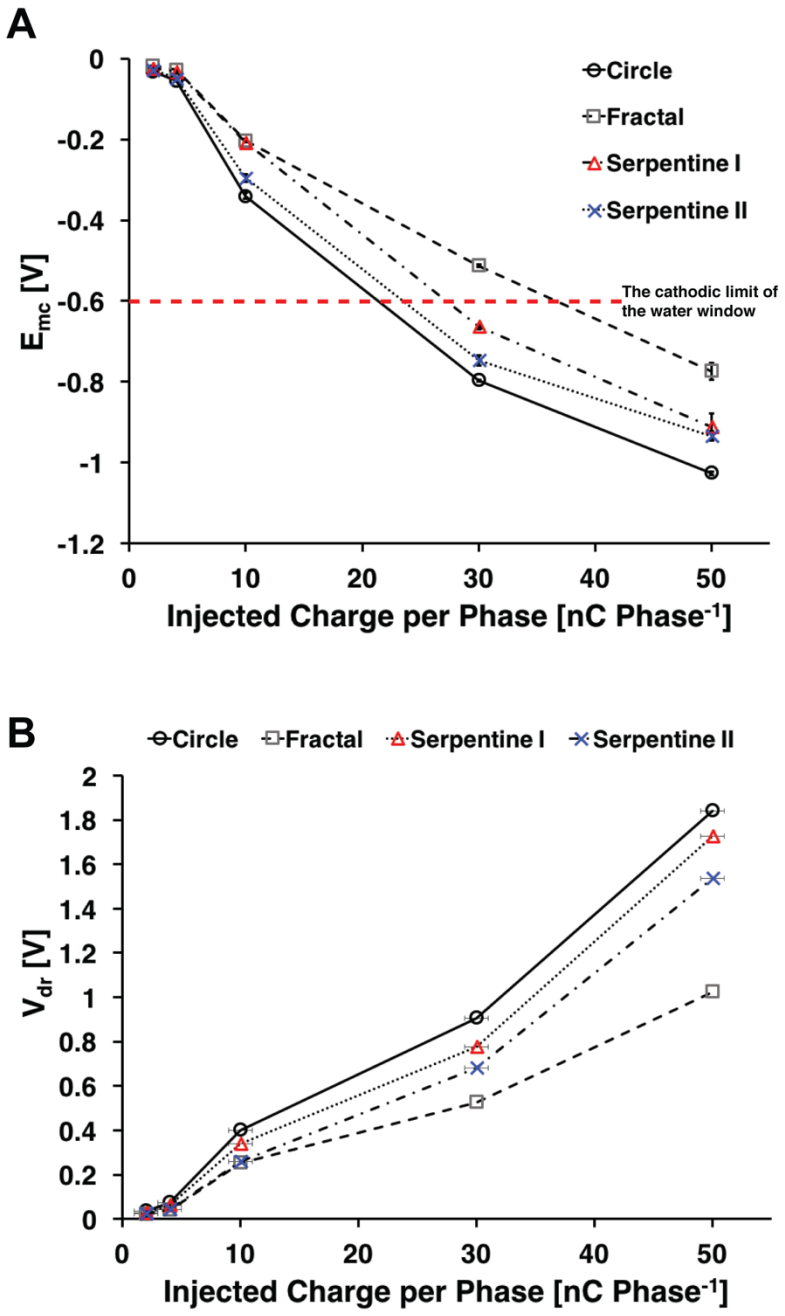

Figure 3.11: (A) Maximum negative potential excursion of the microelectrodes for each electrode design. Estimated charge injection limit (at −0.6 V) for each electrode: circle – 295.07 μC/cm^2 fractal – 510.507 μC/cm^2 serpentine I – 318.817 μC/cm^2 serpentine II – 359.527 μC/cm^2. Maximum driving voltage. Note that the fractal electrodes required significantly smaller amount of V_{dr} for any given injected charge levels.

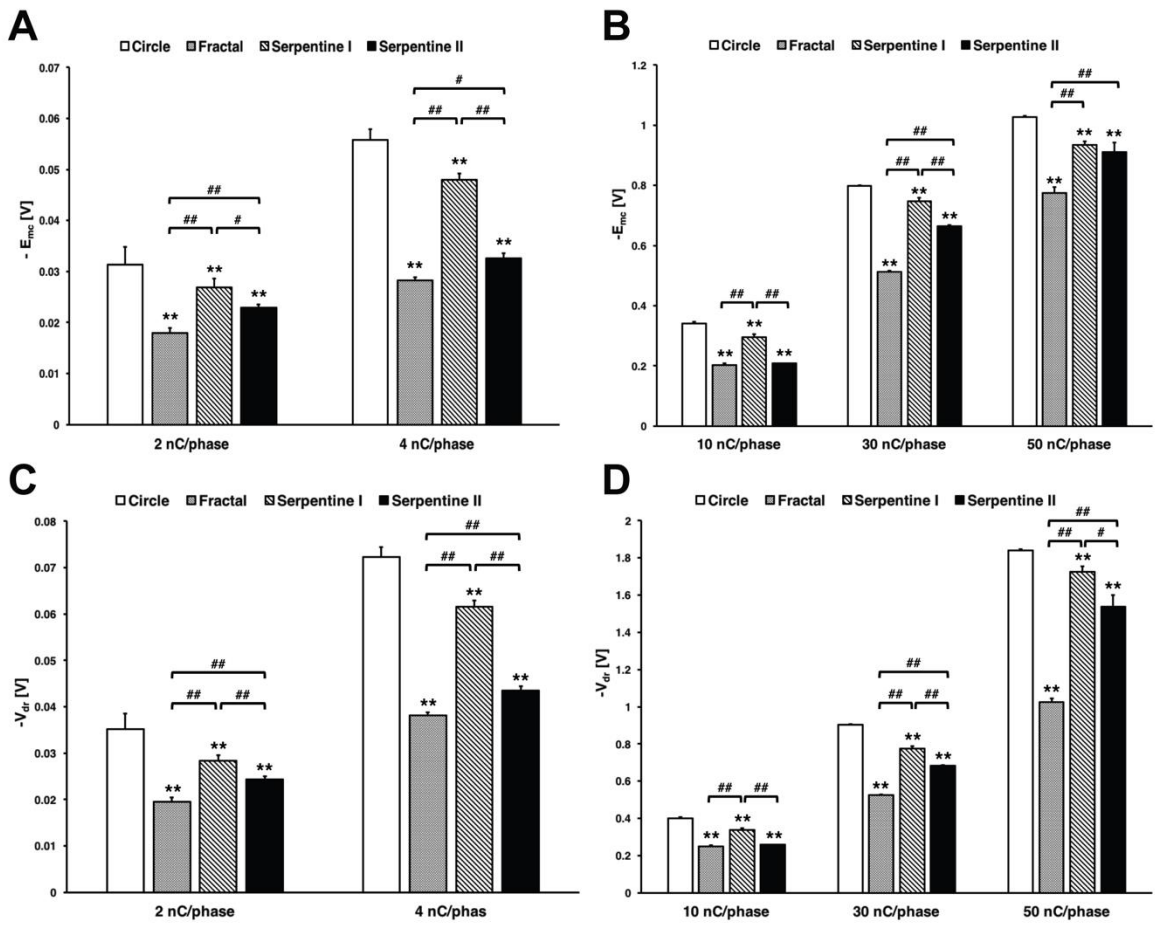

Figure 3.12: (A-B) Maximum negative potential excursion of the microelectrodes with different shapes. Post-hoc pairwise comparisons using Tukey's test ($p<0.01$). (C-D) Maximum driving voltage. Post-hoc pairwise comparison using Tukey's test ($p<0.01$).

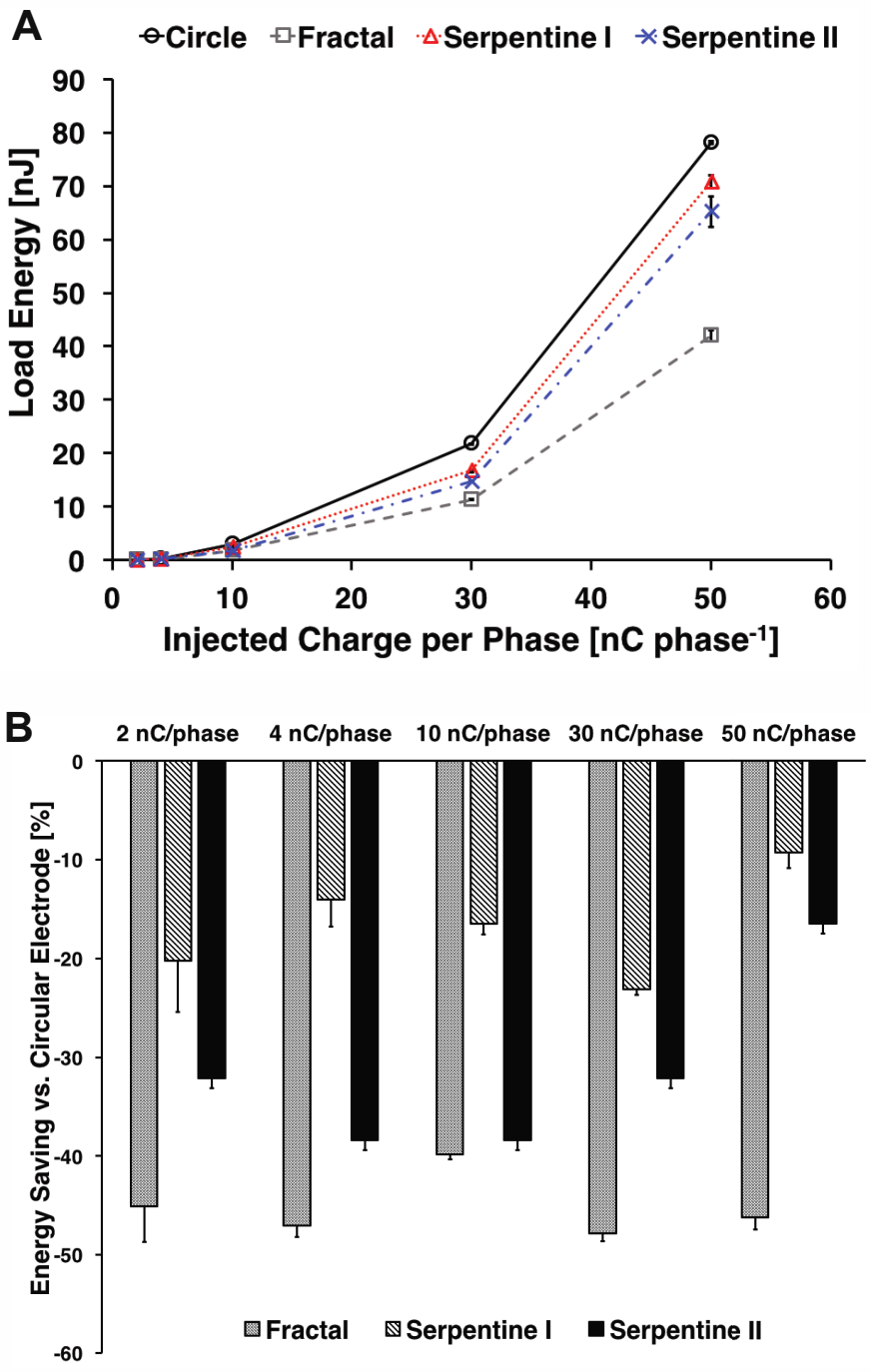

Figure 3.13: Comparison of load energy of the microelectrodes. (A) Energy consumption for a single cathodal pulse from the microelectrodes with different shape when the constant charge per phase was injected. (B) Energy consumption compared to the circular shaped microelectrode. During constant current stimulation the energy required to deliver the same amount of charge was significantly lower for fractal electrodes than other high PSA or circular electrodes.

significantly less energy (up to 47%) to deliver any given charge compared to the circular electrode. The serpentine II electrodes required less energy as well (up to 39%) compared to the circular electrode. However, as the charge level increases, the relative energy savings for the high PSA electrodes against the circular design decreased to less than 20%.

3.7 Conclusions and Discussion

Here we experimentally demonstrated that electrodes with Vicsek fractal geometry may be more electrochemi- cally efficient in charge transfer during neurostimulation than conventional circular microelectrodes and other microelectrodes with higher PSA ratio. Contrary to our expectation, the two different electrode designs with the same PSA ratio demonstrated significantly different electrochemical performance, which suggests the possibility of tailoring optimum electrode designs for various neurostimulation applications. The enhanced charge capacity afforded by the fractal design may also translate into a more energy efficient neurostimulation system with improved functional lifetime.

The CV responses of the four different electrodes revealed a similar PSA effect that has previously been reported in literature [154]. The fractal electrodes, however, showed significantly larger CSC than PSA-matched serpentine I electrodes. Compared to circular electrodes with the same surface area, CSC_c for fractal electrode was 57% higher whereas serpentine I electrode with the same PSA only showed 25% increase. The CSC_c for fractal electrode was similar to that of serpentine II electrodes with perimeter that is 1.6 times larger. The CSC_c increase in Pt microelectrodes can be compared to that of IrO_x microelectrodes. Although the magnitude of CSC_c in IrO_x electrodes are typically 10 times larger than that of Pt electrodes, the change in CSC_c due to increasing PSA from 74 to 255 was approximately 31%, which is close to 25% increase we observed between circular (PSA = 40) and serpentine I (PSA = 256) [154], [172]. This suggests that fractal design in IrO_x may also translate into an even larger improvement in CSC_c as we demonstrated in Pt microelectrodes.

The charge injection limit measured by the voltage transient response of microelectrodes showed similar superior performance of the fractal designs. When pulsed with a charge-balanced current-controlled biphasic stimu- lation waveform, the fractal electrodes exhibited lowest driving potential (V_{dr}) than the other electrode designs. The negative potential excursion (E_{mc}) was the lowest in fractal electrodes as well. When extrapolated for charge injection limit, the fractal

electrodes were able to deliver 73% more charge than circular design (510 $\mu C \cdot cm^{-2}$ vs. 295 $\mu C \cdot cm^{-2}$, Fig. 3.12) without reaching the water hydrolysis limit. Interestingly, the total current injected estimated in our constant voltage COMSOL model was also approximately 55% larger, which is close to the charge injection limit improvement we demonstrated. Other groups have postulated that the increase in charge injection capability of high PSA may be attributable to decrease in access resistance and increase in ionic flux in high PSA electrodes [149], [154]. Indeed, the estimated access resistance (i.e., $V_{dr} - E_{mc}$) for fractal and other high PSA ratio electrodes remained lower than that of circular electrodes at various charge injection levels (Fig. 3.12).

This is also supported by our COMSOL analysis. Although our simplified numerical analysis does not take into account the impact of diffusion, the fractal and other high-PSA electrodes showed a lower overall resistance than circular electrode (Fig. 3.6). The impedance measured in PBS also suggest the lower overall electrode resistance for non-Euclidean electrodes, however, it is difficult to distinguish the contribution due to Faradaic processes. Our EIS data in ferri-ferrocyanide does provide clearer evidence to demonstrate superior ionic flux in fractal and other non-Euclidean, high-PSA microelectrodes (Fig. 3.8). Moreover, the equivalent circuit model analysis showed that the fractal elec- trodes have significantly higher capacitance than other electrodes, which suggests that these non-Euclidean microelectrodes have greater charge injection capacbility due to lower access resistance, superior ion flux, and lager capacitance (Fig. 3.9). Compared to the conventional stimulation electrodes found in DBS or SCS, the microelectrodes have significantly higher overall interface impedance due to their smaller size. Thus, creating a more efficient electrode design is critical in ensuring longevity of neurostimulation devices with high-density microelectrode array.

In a recent simulation, Watterson et al. highlighted enhanced potential penetration capability of fractal electrodes [160]. The authors suggested that larger electrode bounding perimeter and the additional double layer capacitance afforded by the vertical side-wall, can lead to additional charge transfer that results in greater potential penetration. However, our work demonstrates that even without the added side-wall, the fractal designs may have greater charge injection capability due to superior Faradaic and non-Faradaic electrochemical processes. Although several groups have already proposed the idea of using high PSA electrode to improve charge transfer efficiency of stimulating electrodes, this work provides the first evidence to suggest that even more superior electrode may be possible by optimizing the geometry.

A critical next step is to evaluate the impact of electrode design in terms of its mechanical stability. As shown in our FEM (Fig. 3.3), the fractal design resulted in higher current density than other electrodes. The Pt electrodes are known to suffer from dissolution that scale with the magnitude of current density [173], [174]. With the increased cur- rent density, we expect the dissolution process for these high PSA electrodes to be accelerated as well. Therefore, further study on the effects of fractal design on electrode dissolution is warranted altough the concern for elec- trode integrity may be mitigated by utilizing non-Pt electrodes materials or via imbalanced stimulation waveforms [175]. Finally, it is essential to investigate whether a more energy efficient neural stimulation can actually be achieved in vivo using these fractal microelectrode designs to confirm our electrochemical results.

4. GRAPHENE PROTECTION LAYER TO PREVENT NEUROSTIMULATION-INDUCED PLATINUM DISSOLUTION

4.1 Introduction

Platinum (Pt) is widely used in neurostimulation devices as the electrode material and is regarded as the gold standard for implantable neural interface [176]–[181]. However, a well-known problem of using Pt, especially for a high-density neural interface with microscale electrodes, is that it can undergo irreversible electrochemical reactions during neurostimulation that can physically alter the electrode surface. Irreversible Pt dissolution can occur during neurostimulation due to cyclic formation and reduction of an oxide layer on Pt surface [173]. Moreover, Pt can react with the chloride ions during the anodic phases to form platinum chloride species that can affect cellular physiology [182]–[184].

Pt dissolution can have detrimental effects on the functional lifetime of neural interface by altering the geometry, the material, and the electrical properties of the microelectrode [185], [186]. Moreover, the byproduct of Pt dissolution may be toxic to the surrounding neural tissue. Pt concentration as low as 1 ppm is known to cause morphological and functional changes in neurons, and Pt concentration over 50 ppm is thought to have cytotoxic effects [187]. More recently, Wissel et al revealed that released Pt during the stimulation can significantly reduce mitochondrial activity and induce oxidative stress on cells [188].

Pt dissolution is thought to occur even at low current levels. In one of the classic experiments, Robblee et al, demonstrated a Pt dissolution rate of 0.5 μg cm^{-2} in vivo for 1.1 mm-diameter circular electrodes even with a low charge density of 20 μC cm^{-2}. With smaller microelectrodes, the dissolution process is expected to be accelerated. This may be problematic especially for fractal microelectrodes that are thought to have superior charge transfer capabilities than conventional circular electrodes [189]–[191]. Although the dissolution rate is known to be slower in vivo due to protein layer adsorption on the microelectrodes, the fractal designs are still expected to experience significant dissolution during neurostimulation due to their higher current density.

With the growing demand for more advanced flexible and minimally invasive neural interfaces (annual growth rate of 7%–17%) and the increase in the number of neurological disorders (36.7% between 1990 and 2015), the use of high-density Pt microelectrodes in

neurostimulation devices is likely to experience continued growth in the future [132], [192]. However, the concerns for neural interface stability due to Pt dissolution of microelectrodes may temper the excitement for these advanced microfabricated devices. Therefore, a better solution to prevent Pt dissolution is needed to ensure that the chronic neural interface remain functional for long-term usage.

In this work, we demonstrate that a graphene mono layer can be used as a protective layer that can significantly alleviate Pt-dissolution during a prolonged neurostimulation while maintaining good charge transfer characteristics. Graphene is a two-dimensional carbon sheet with a honeycomb structure. With the long range π-conjugation, graphene is widely used in electronics, energy, and biomedical applications because of its remarkable mechanical, thermal, and electrical characteristics [193]–[199]. Furthermore, because of its impermeability against gas and liquid, graphene is known to be an excellent diffusion barrier that can protect the surfaces of reactive metals from oxidation [200]–[203].

Here we microfabricated fractal and circular Pt-microelectrodes to measure their dissolution rates during a prolonged neurostimulation in a proteinaceous buffer solution. We compared the dissolution rate of the bare Pt with graphene-coated Pt (G-Pt) microelectrodes using an inductively coupled plasma- mass spectroscopy (ICP-MS) and confirmed the compositional changes using an x-ray energy dispersive spectroscopy (EDX). Furthermore, we measured the changes in electrochemical properties of various microelectrodes before and after an extended neurostimulation. We found that a graphene monolayer significantly decreased the Pt dissolution rate to negligible levels even for fractal microelectrodes with little change in their charge transfer characteristics during charge-balanced biphasic stimulation. Our results suggest that a graphene monolayer may be used to mitigate Pt-dissolution in chronically implantable neural interface devices. Moreover, these results suggest a path forward for utilizing the fractal microelectrodes for high-density neural stimulation applications (e.g. deep brain stimulation, vision prostheses, etc.) without the potential reliability issues.

4.2 Device Fabrication

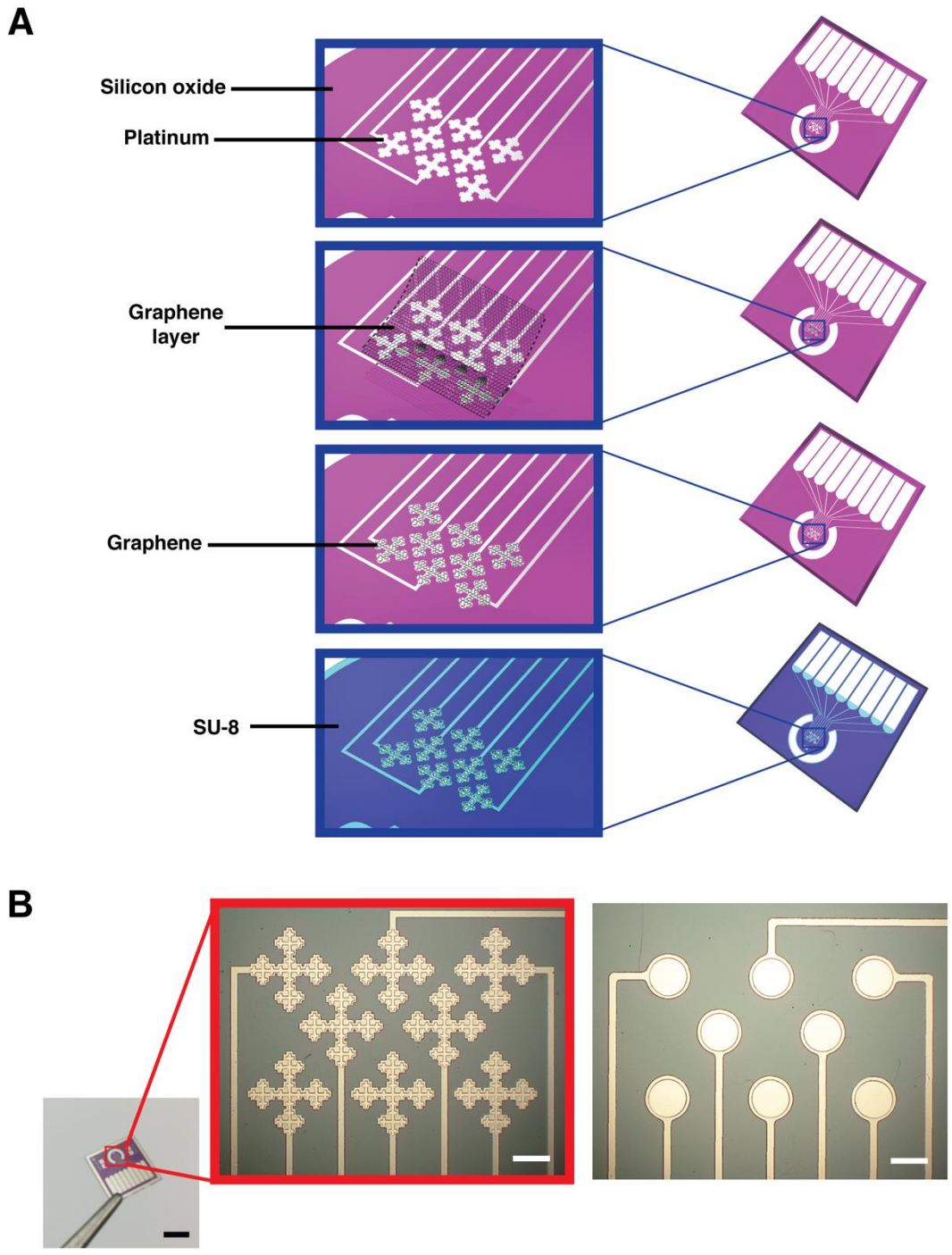

Figure 4.1: G-Pt microelectrodes with different shapes**.** (A) Fabrication process of G-Pt microelectrodes: metal patterning for electrodes and contact pads on silicon oxide on silicon wafer. Transfer the monolayer graphene. Graphene patterning for electrode sites. SU-8 patterning for the passivation layer. (B) Optical micrographs of the fabricated G-Pt microelectrodes. Scale bar =100 µm.

The circular and fractal shaped microelectrodes were designed to have identical surface area (7.854×10^{-3} mm) to investigate the impact of geometry on Pt corrosion. Pt microelectrodes array were fabricated on 500 nm film of silicon oxide by thermal oxidation of silicon wafer (Fig. 4.1). Microelectrodes patterns were defined using a positive photoresist (AZ1518, MicroChem, Newton, MA, USA), which is followed by deposition of Ti adhesion layer (10 nm) and Pt layer (100 nm thick) using e-beam evaporator. The metal patterns were achieved by lift-off process using acetone. SU-8 passivation layer (1.5 µm thick) was spin-coated and patterned using photolithography.

To fabricate the G-Pt microelectrode, a monolayer of graphene (~ 1.7 nm-thick [204]) was grown on copper (Cu) substrate by low pressure chemical vapor deposition (CVD) at 1000 ^{o}C using methane as carbon precursor. Poly(methyl methacrylate) (PMMA) was first spin coated on the graphene layer to aid the transfer process. After curing the PMMA at 180 °C for 5 min, the Cu was etched away by $FeCl_3$ solution. The PMMA/ graphene stack was washed with deionized water, then the stack was transferred onto Pt patterned substrate. PMMA was removed using acetone, the sample was cleaned with isopropyl alcohol (IPA). The transferred graphene was patterned using photolithography and reactive ion etching with oxygen plasma. Finally, SU-8 was coated and patterned for passivation layer.

4.3 Platinum Dissolution

To measure Pt dissolution rate, the 3D printed testing chamber was filled with air-saturated phosphate- buffered saline (PBS) with composition of 1.1 mM KH_2PO_4, 155 mM NaCl, 3 mM $Na_2HPO_4 \cdot H_2O$ with pH 7.4 (ThermoFisher Scientific, Waltham, MA, USA) with 0.2 mg ml^{-1} bovine serum albumin (ThermoFisher Scientific, Waltham, MA, USA) at room temperature. The current pulses for 0.35 mC cm^{-2} were injected into the electrode at 50 Hz with a 1 ms pulse width and 1 ms inter-pulse delay. Aliquots of PBS in the testing chamber were taken every 2 h during the 10 h stimulation of each electrode type (n = 3, each) and measured the Pt concentration change using Thermo Element II ICP-MS (ThermoFisher Scientific, Waltham, MA, USA. Collected samples were digested using aqua regia and diluted with 4% HCl for ICP-MS analysis of Pt ion concentration.

Figures 4.2A and B show bare Pt microelectrodes before and after a continuous 3 d stimulation using 0.35 mC cm^{-2} at 50 Hz, which is below the safety charge injection limit for Pt

electrodes [205], [206]. Both fractal and circular design showed significant dissolution only after 3 d in a proteinaceous PBS. Figure 4.2C compares the amount of Pt released over the stimulation period for bare and G-Pt micro- electrodes with circular and fractal designs. In our previous study,

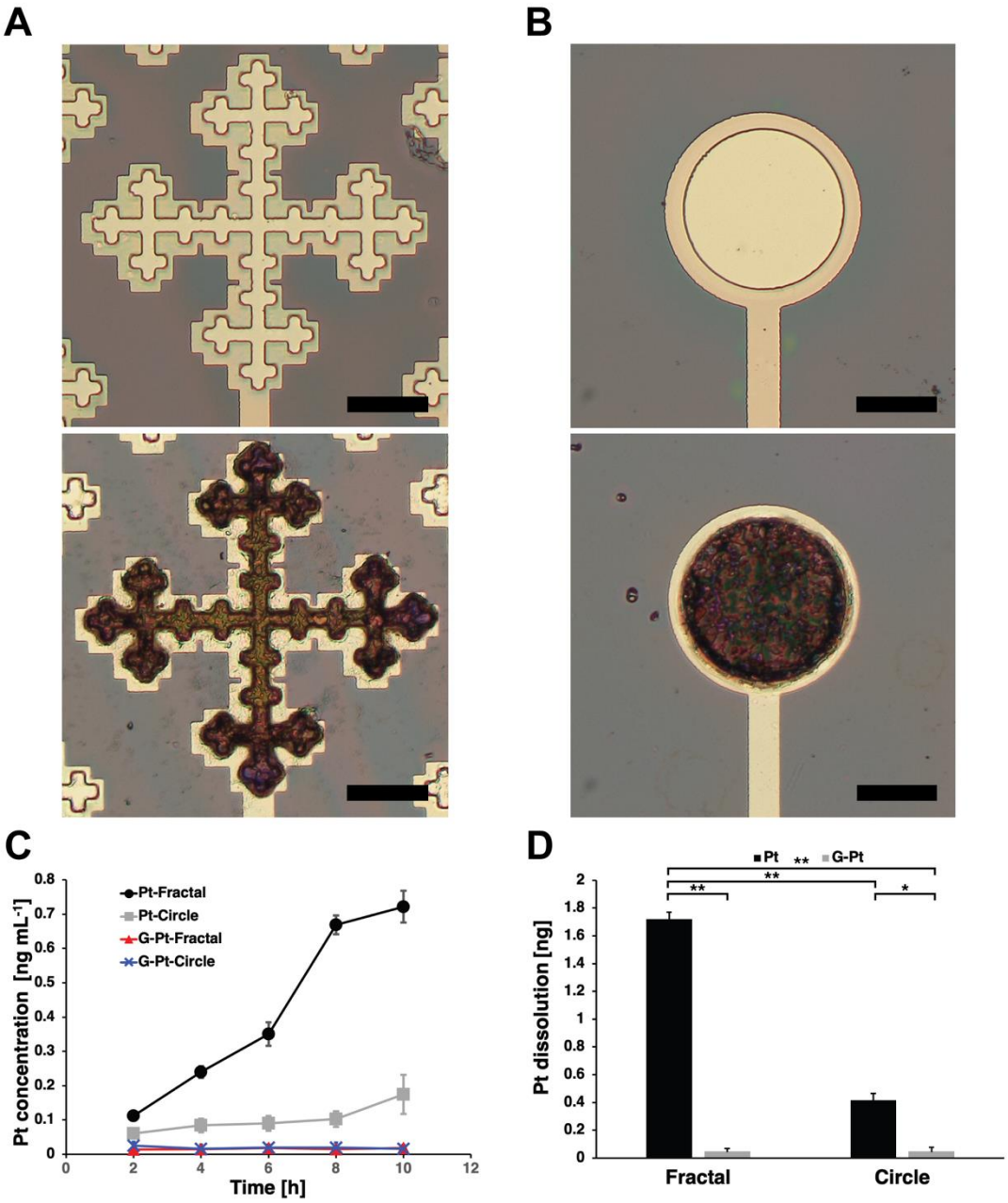

Figure 4.2: Pt microelectrodes dissolution. (A) Representative optical image of Pt microelectrode with the fractal design before (top) and after (bottom) 3 d stimulation. Scale bar =50 µm. (B) Optical images of circular Pt microelectrodes before (top) and after (bottom) 3 d stimulation. Scale bar =50 µm. (C) Pt concentration in PBS from the fractal and circle microelectrodes with Pt and G-Pt. (D) Total Pt dissolution for 10 h-stimulation, which showed statistically significant reduction for both fractal and circular microelectrodes (* for $p < 0.05$, and

the fractal microelectrodes exhibited higher current density across its surface than the circular microelectrodes for a given electrode potential [191]. With the increased current density, we predicted that the electrode dissolution may be predicted. As we expected, the bare Pt microelectrodes with fractal design showed the highest dissolution rate with 35.4 ng C^{-1} than its circular counterpart with dissolution rate of 8.7 ng C^{-1} for 10 h-stimulation. Conversely, both fractal and circular G-Pt exhibited significant reduction in Pt dissolution rate compared to their bare Pt counterparts (1.0 ng C^{-1} for both), which supports our hypothesis that the graphene monolayer can effectively prevent dissolution as a diffusion barrier.

When comparing the total amount of lost Pt, the effectiveness of graphene monolayer in preventing dissolution becomes clearer (figure 4.2D). For fractal microelectrodes, the graphene layer reduced Pt dissolution by 97% after 10 h ($p < 0.01$, Table 4.1). For circular microelectrodes, it reduced Pt dissolution by 88% ($p < 0.01$). For a longer stimulation period, we expect the percent reduction to be even larger for each electrode design.

Table 4.1: Amount of Pt release of each electrode type during 10-h stimulation

	Pt [ng]	**G-Pt [ng]**	**Reduced Pt loss [%]**
Circle	0.42 ± 0.05	0.05 ± 0.03	87.8 ± 7.22
Fractal	1.72 ± 0.09	0.05 ± 0.02	97.1 ± 0.99

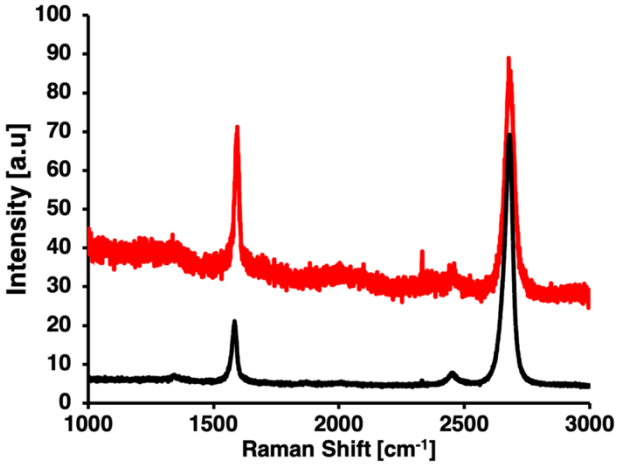

Figure 4.3: Raman spectroscop**y.** Raman spectroscopy were taken on the same graphene coated fractal electrode before (black line) and after stimulation (red line).

To explore stability of the graphene layer on the Pt electrode surface, we performed Raman spectroscopy on G-Pt electrode surface (Fig 4.3). We observed the characteristic peaks for graphene monolayer before and after the neurostimulation, which suggests that graphene layer was not affected by the biphasic stimulation. We also confirmed the compositional changes using EDX (Fig 4.4). After 10 h stimulation, both fractal and circular bare Pt microelectrodes had higher oxygen and lower Pt contents than before the stimulation (Table 4.2). The Pt contents were decreased by the dissolution process, which suggests that the electroactive surface may also be reduced. In contract, we saw little change in oxygen and Pt contents on G-Pt microelectrodes following the 10 h stimulation (Fig 4.5).

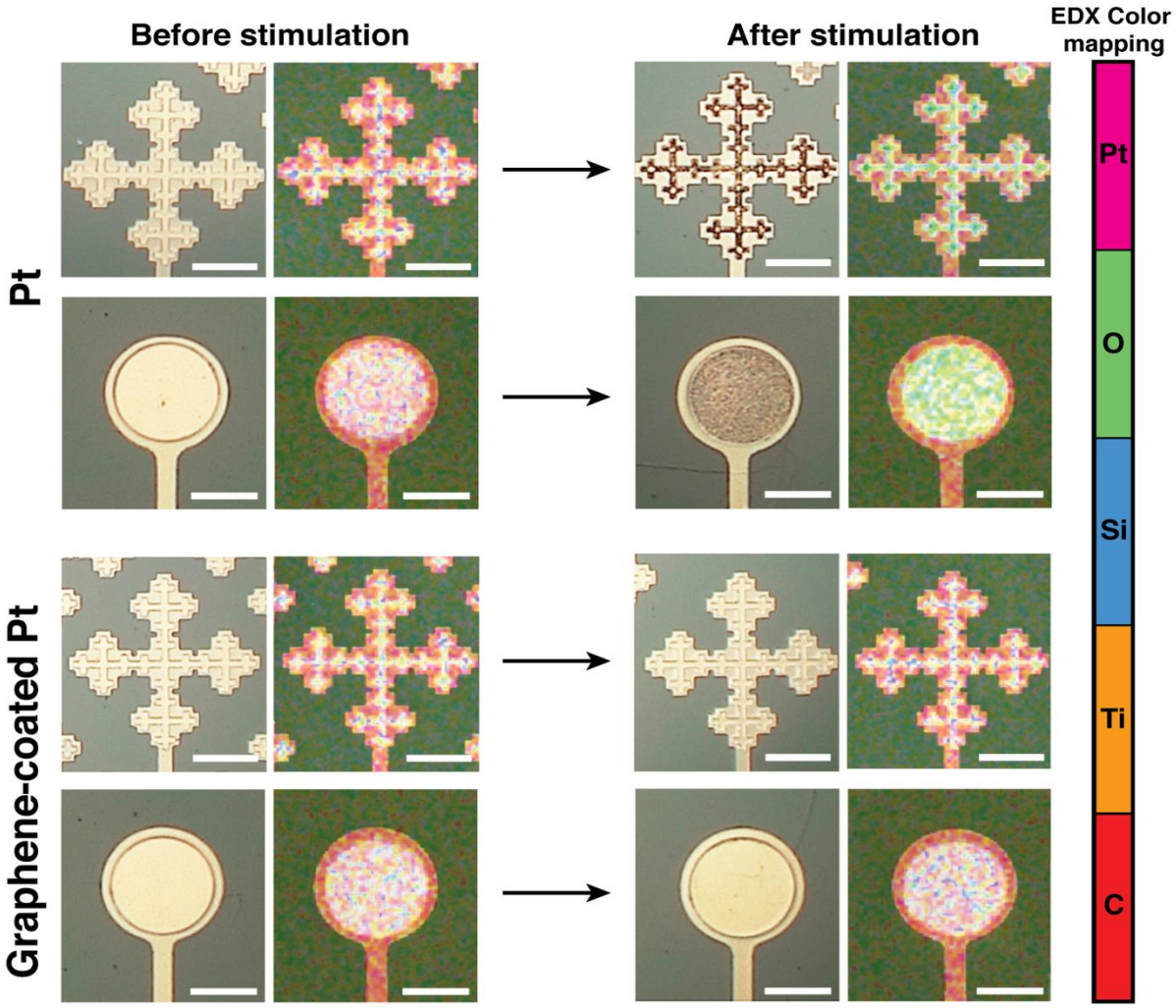

Figure 4.4: Optical images and the corresponding EDX color map of Pt and G-Pt microelectrodes. In the EDX image, pink, green, blue, orange, red dots indicate the presence of Pt, oxide, silicon, titanium, and carbon, respectively. Scale bar =50 µm. Note the change in coloration in both optical and EDX images that suggests change in electrode material.

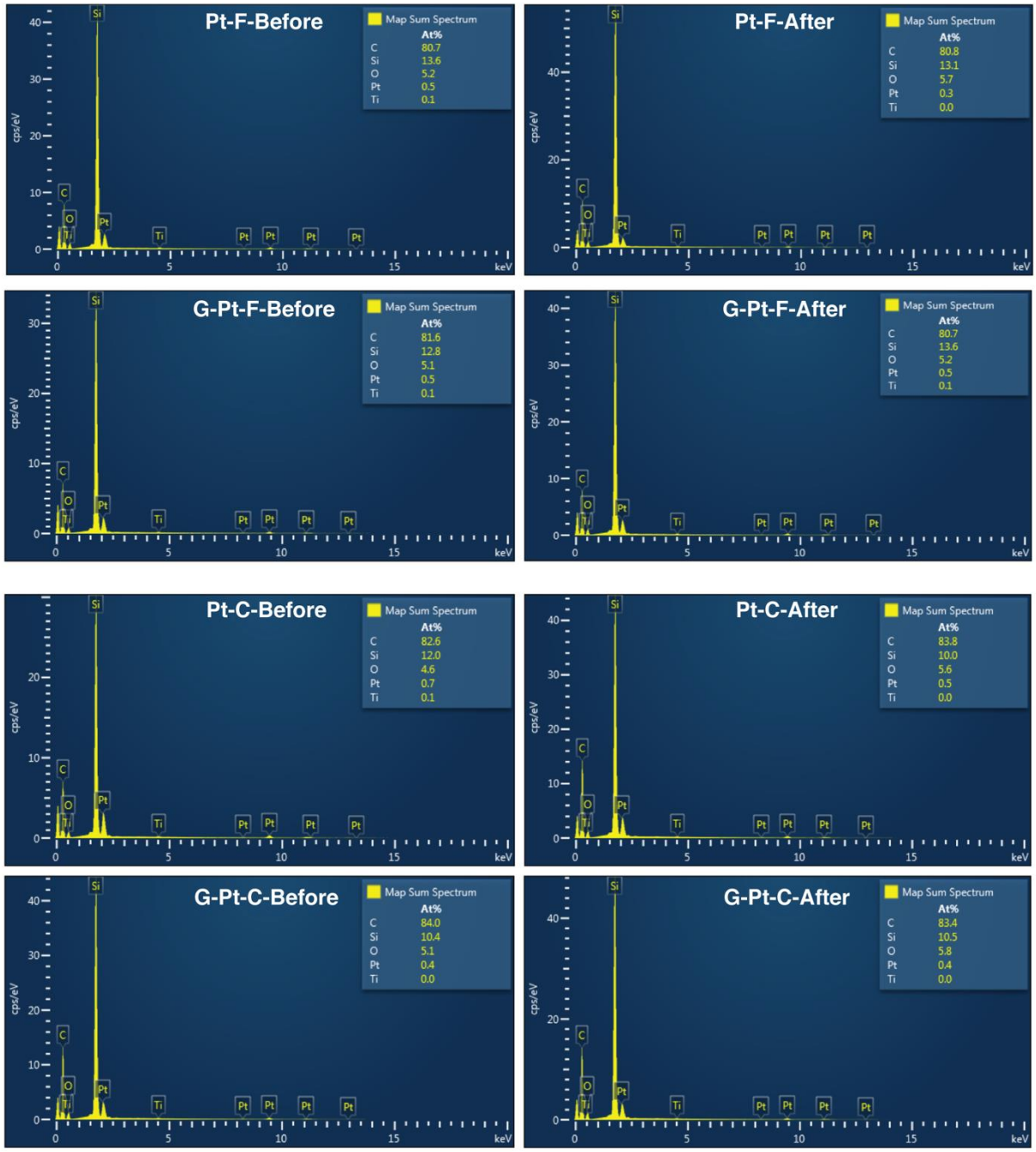

Figure 4.5: EDX spectra from each microelectrode.

Although we demonstrated that the Pt dissolution may be suppressed using a graphene monolayer, we will need to further explore the robustness of this approach. The anti-corrosion

Table 4.2: Atomic weight percentage of each electrode from map sum EDX spectrum (Unit = [%])

	Pt-F (Before)	Pt-F (After)	Pt-F (Before)	Pt-F (After)	Pt-F (Before)	Pt-F (After)	Pt-F (Before)	Pt-F (After)
C	80.7	80.8	82.6	83.8	81.6	80.7	84.0	83.4
Si	13.6	13.1	12.0	10.0	12.8	13.6	10.4	10.5
O	5.2	5.7	4.6	5.6	5.1	5.2	5.1	5.8
Pt	0.5	0.3	0.7	0.5	0.5	0.5	0.4	0.4
Ti	0.1	0.0	0.0	0.1	0.1	0.0	0.0	0.0

properties of graphene demonstrated in other non-noble metal has shown that potential defects, cracks, or scratches on graphene could lead to a localized oxidation [207]–[210], which may be why we still observed some dissolution on G-Pt microelectrodes. These defects in graphene could provide a diffusion channel for molecules such as O_2 and H_2O through the graphene–metal interface [211]–[213] and the space between graphene–metal inter- face may act as a 2D container for Faradaic reactions [214]–[216]. When the coupling is strong, the density of states of graphene gets modified and changes from the Dirac cone dispersion to a more conventional parabolic dispersion [217]. As such, we suspect that different substrate metals have varying degrees of coupling interaction with graphene, which can impact various electrochemical reactions including corrosion and charge transfer process. Therefore, a careful consideration of metallic substrate may be necessary to avoid generation of potentially harmful electrochemical byproducts that can compromise the neural interface over long-term. One way to mitigate graphene defects is to use multi-layer graphene. However, additional graphene layers may increase overall electrode impedance and reduce charge transfer performance of these stimulating microelectrodes. Nevertheless, it would be informative to demonstrate the impact of monolayer and multi-layer G-Pt microelectrodes using in vitro and in vivo models. Our results show that G-Pt micro- electrodes had only 0.019 ng ml^{-1} of dissolution after 10 h stimulation. In previous studies, > 1.6 µg ml^{-1} of dissolved Pt was required to induce cell death [218]. Although it would require 35 d of continuous stimulation to generate such large concentration Pt from monolayer G-Pt, it would be interesting to see how multi-layer G-Pt microelectrodes would perform.

4.4 Cyclic Voltammetry and EIS

To investigate the impact of Pt dissolution on the electrochemical performance and the CSC_c of these microelectrodes, we performed CV measurements on bare Pt and G-Pt microelectrodes with different designs. CV and EIS was measured using a potentiostat (SP- 200, Bio-Logic.Inc, Seyssinet-Pariset, France) with Ag/AgCl with 3M KCl (RE-1CP, ALS Co. Ltd., Tokyo, Japan), 5 mm diameter graphite counter electrode, and working electrodes on the microelectrode array. CV was measured in PBS with 0.2 mg ml^{-1} BSA. Scan rate for CV was 50 mV s^{-1} between potential range of −0.6 V and 0.8 V versus Ag/AgCl reference electrode. CSC_c was calculated from the overall charge storage capacity (CSC) using the previously described equation in chapter 3. EIS were measured with the AC voltage perturbation potential of 30 mV amplitude in the frequency range from 1 to 100 kHz in PBS with BSA at room temperature.

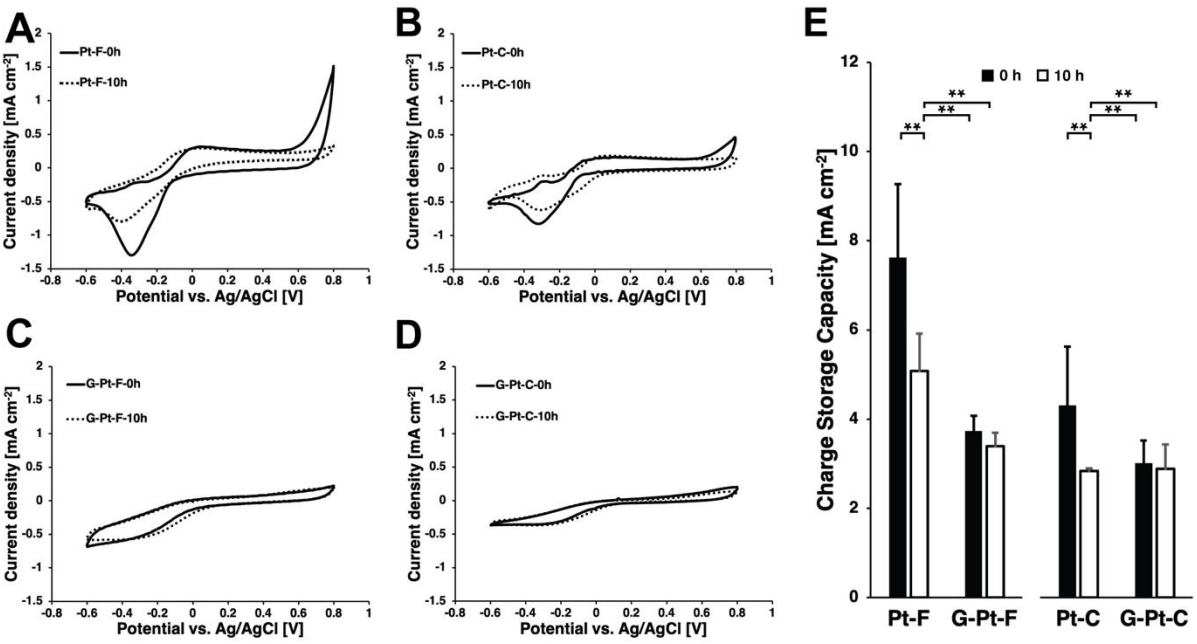

Figure 4.6: CV of Pt and G-Pt microelectrodes. (A) CV of fractal Pt microelectrodes before and after the stimulation. (B) CV of the circular Pt microelectrodes . (C) Cyclic voltammetry measurements on the fractal G-Pt microelectrodes. (D) Cyclic voltammetry measurements on the circular G-Pt microelectrodes. (E) CSC of each electrode (n = 5 for each). Note that ANOVA showed statistically significant differences between electrodes (**, $p < 0.01$).

Figures 4.6A and B show a substantial decrease in oxidation and reduction peaks following a 10 h of stimulation using bare Pt microelectrodes with either fractal or circular design. These results suggest that the bare Pt microelectrodes not only demonstrate physical changes but they also undergo substantial changes to their electrochemical characteristics after only a 10 h of continuous stimulation. In comparison, G-Pt microelectrodes demonstrated little change in CV after the same treatment (Fig 4.6C and D). Compared to the bare Pt microelectrodes, G-Pt ones showed substantially decreased Faradaic reaction peaks, which supports our hypothesis that the graphene layer can significantly reduce Pt dissolution by impeding the diffusion of oxidative species. The CSC_c measures the total amount of charge available for a single cathodic stimulation pulse, which is an indication of the cathodic charge injection capacity. Using one-way ANOVA with Tukey's HSD post-hoc test, we compared the CSC_c of each micro- electrode before and after

the 10 h stimulation (Fig 4.6E). The CSC_c of bare Pt microelectrodes decreased significantly after the 10 h stimulation ($p < 0.01$). As expected, the fractal microelectrodes showed a more significant CSC_c decrease than the circular microelectrodes. However, G-Pt microelectrodes showed little changes in CSC_c before and after the stimulation. This further supports our hypothesis that the graphene layer can provide protection against Pt dissolution and prevent changes in charge transfer characteristics. Although G-Pt microelectrodes had smaller CSC_c than bare Pt microelectrodes, which is most likely due to the reduction in Faradaic charge transfer, the improved stability in CSCc suggest G-Pt may be a better neural interface for chronic implantation.

Next, we performed EIS to evaluate the changes in microelectrode impedance following the stimulation (n = 5, each). Figure 4.7A show the impedance spectra of the bare Pt and G-Pt microelectrodes before and after the stimulation. Throughout the entire frequency range, the impedance of bare Pt electrodes increased. In contrast, we observed relatively small differences in the G-Pt microelectrodes (Fig 4.7B). The phase responses of Pt and G-Pt microelectrodes had different shapes, which demonstrates the impacts of electrode design and graphene coating (Fig 4.7C and D). Compared to the bare Pt microelectrodes, G-Pt microelectrodes showed relatively small change in phase responses before and after the stimulation.

When comparing the impedance at 1 kHz, we saw that the impedance of bare Pt microelectrodes increased significantly following the stimulation (Fig 4.7E). Conversely, we found no significant differences in impedances for G-Pt microelectrodes after the stimulation (Fig 4.7F), which further demonstrate superior stability of G-Pt microelectrodes. To better understand the electrochemical characteristics of the microelectrodes, EIS data were fitted to an equivalent circuit model to estimate the parameters of a solution resistance R_s, a charge transfer resistance R_{ct}, a double layer capacitance C_{dl}, a resistance of the adsorbed protein film R_f, capacitance of the protein film C_f, and the Warburg element W (Fig. 4.7G) [218], [219]. Overall, the fractal microelectrodes had lower resistive components (R_s, R_{ct}, and R_f) than circular microelectrodes (Table 4.3). Following the stimulation, we saw substantial changes in each fitted parameter for bare Pt microelectrodes. The changes were more pronounced for fractal than circular microelectrodes, which highlight the risk of using unprotected fractal microelectrodes. However, we saw minimal changes across all estimated EIS parameters for the G-Pt microelectrodes after the stimulation. Interestingly, R_f were higher for bare Pt microelectrodes than G-Pt ones. In

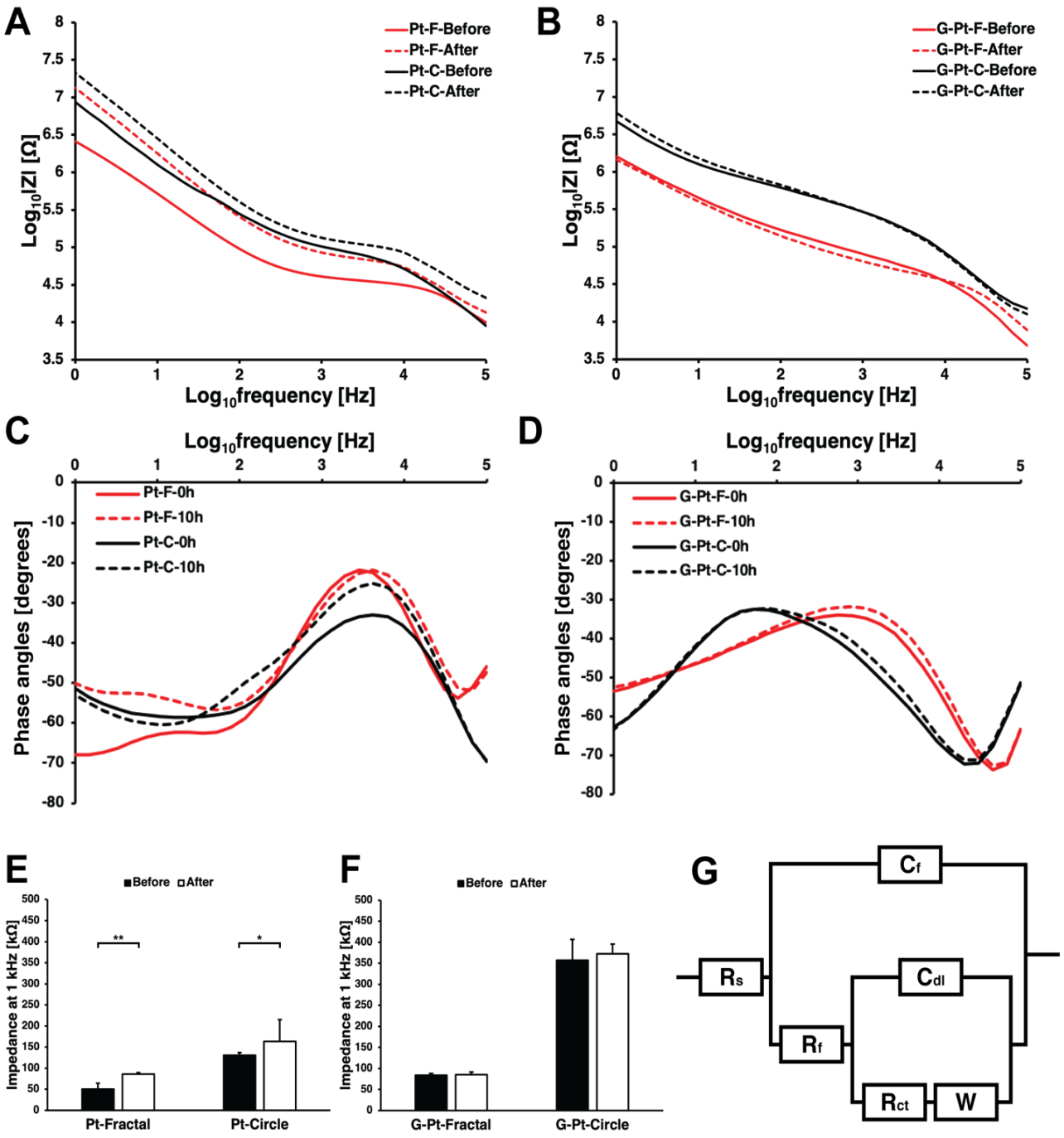

Figure 4.7: Electrochemical impedance spectroscopy. (A) Impedance responses of the bare Pt microelectrodes with different shapes before and after the stimulation. (B) Impedance responses of the G-Pt microelectrodes. (C) Phase angle versus frequency of the Pt microelectrodes. (D) Phase angle versus frequency of the G-Pt microelectrodes. (E) Impedance of Pt microelectrodes at 1 kHz (* for $p < 0.05$, and ** for $p < 0.01$). (F) Impedance of G-Pt at 1 kHz. (G) Equivalent circuit model for each electrode in PBS with BSA.

contrast, C_f of bare Pt micro- electrodes were lower than that of G-Pt microelectrodes. Compared to the surface potential of Pt (< 200 mV) [220], the graphene layer has a lower surface potential (−77 mV) in PBS [221], which can electrostatically repulse negatively charged BSA molecules with the surface potential of −20.3 mV in PBS [222]. There- fore, we suspect that there may be a smaller amount of adsorbed protein on Gt-Pt microelectrodes than on bare Pt microelectrodes. Moreover, we saw that the R_f increased while C_f decreased following a 10 h stimulation of bare Pt microelectrodes, which may be due to an increased amount of adsorbed protein. In contrast, we saw little change in R_f and C_f for G-Pt microelectrodes, which suggests there may be relatively little change in protein adsorption amount on these electrodes even after a prolonged neurostimulation.

Table 4.3: Estimated parameters of equivalent circuit model for each electrode in PBS. (n = 5 each)

	R_s [kΩ]	R_{ct} [kΩ]	C_{dl} [nF]	R_f [kΩ]	C_f [nF]	W [MΩ $s^{-1/2}$]
Pt-F-Before	2.02 ± 0.27	15.5 ± 7.68	4.38 ± 0.69	49.9 ± 0.75	0.20 ± 0.05	1.92 ± 0.43
Pt-F-After	4.26 ± 0.35	56.0 ± 3.85	2.40 ± 0.32	124 ± 0.03	0.15 ± 0.04	4.58 ± 0.49
Pt-C-Before	5.32 ± 0.29	40.2 ± 14.1	2.02 ± 1.01	73.8 ± 1.02	0.29 ± 0.08	6.14 ± 3.52
Pt-C-After	8.62 ± 0.10	63.6 ± 27.9	1.75 ± 0.97	248 ± 1.93	0.18 ± 0.05	7.33 ± 1.96
G-Pt-F-Before	2.27 ± 0.21	19.5 ± 9.72	5.96 ± 3.12	24.8 ± 0.64	0.30 ± 0.07	2.02 ± 0.46
G-Pt-F-After	2.42 ± 0.29	21.7 ± 11.8	6.05 ± 2.74	26.1 ± 1.27	0.26 ± 0.10	2.20 ± 0.11
G-Pt-C-Before	5.51 ± 0.12	42.4 ± 13.1	3.05 ± 2.83	44.8 ± 4.13	0.30 ± 0.12	7.79 ± 0.62
G-Pt-C-After	5.57 ± 0.18	43.1 ± 9.95	3.39 ± 1.29	49.2 ± 16.6	0.32 ± 0.11	7.68 ± 0.76

4.5 Voltage Transients

Finally, we compared the voltage transient characteristics of the microelectrodes to confirm the long-term stimulation charge-injection capacity (n = 5, each). Each electrode was stimulated using biphasic, symmetric pulses with 1 ms pulse width at 26.97 nC per phase (0.35 mC cm^{-2} with 26.97 µA at 50 Hz). The charge-balanced biphasic current pulse was applied using a sourcemeter (2601A, Keithley, Cleveland, OH, USA) with a biased inter-pulse potential level to 0 V versus Ag/AgCl reference electrode. The voltage transient measurements were performed in the PBS with BSA at room temperature. To prevent DC leakage during the stimulation, an isolation capacitor (10 µF) was placed between the sourcemeter and working electrode. The pulsing was done at 50 Hz with a 1 ms pulse width and 1 ms inter-phase delay. The current pulses were injected into the electrode, and a data acquisition board (NI USB-6333, National Instruments, Austin, TX, USA)

was used to record the voltage transient. The time delay that the applied current is completely off was measured to be approximately 50 µs, therefore, E_{mc} was estimated at 50 µs immediately after the end of the cathodic pulse. To estimate Q_{inj}, E_{mc} of each electrode was measured in the range of specific injected charge density (0.15, 0.2, 0.25, 0.3, 0.35 mC cm^{-2}). Regression function was estimated using the E_{mc} points in the injected charge density range, and Q_{inj} was calculated by the regression function.

The interphase potential was set to 0 V versus Ag/AgCl reference electrode. To compare, we measured the maximum negative potential excursion (E_{mc}), the maximum driving voltage (V_{dr}), and the charge injection limit (Q_{inj}) from the voltage transient responses (Fig 4.8A). Figure 4.8B shows that the maximum negative voltages of both types of bare Pt microelectrodes increased after the 10 h of stimulation. However, G-Pt microelectrodes maintained relatively stable voltage transient responses following the stimulation (Fig 4.8C). The E_{mc} is the potential required to polarize the electrode, which is measured at the end of the cathodic phase of the biphasic pulse. Figures 4.8D and E show the comparison of E_{mc} and V_{dr} for each electrode at 26.97 nC per phase. In general, fractal microelectrodes have lower E_{mc} and V_{dr} than the circular ones as we demonstrated previously [191]. Moreover, the bare Pt fractal microelectrodes showed a larger increase in E_{mc} and V_{dr} following 10 h stimulation than the circular microelectrodes, which highlight the design's vulnerability. However, G-Pt microelectrodes showed virtually no change in E_{mc} and V_{dr} following the stimulation. When comparing the Q_{inj} of each microelectrode, the benefit of G-Pt became even more apparent (Fig 4.8E). Our results showed that bare fractal microelectrodes suffered significant loss in Q_{inj} after the 10 h stimulation while G-Pt microelectrodes maintained its Q_{inj}. This bodes well for the high performing fractal designs because their post-stimulation Q_{inj} remained > 3X of the circular microelectrodes.

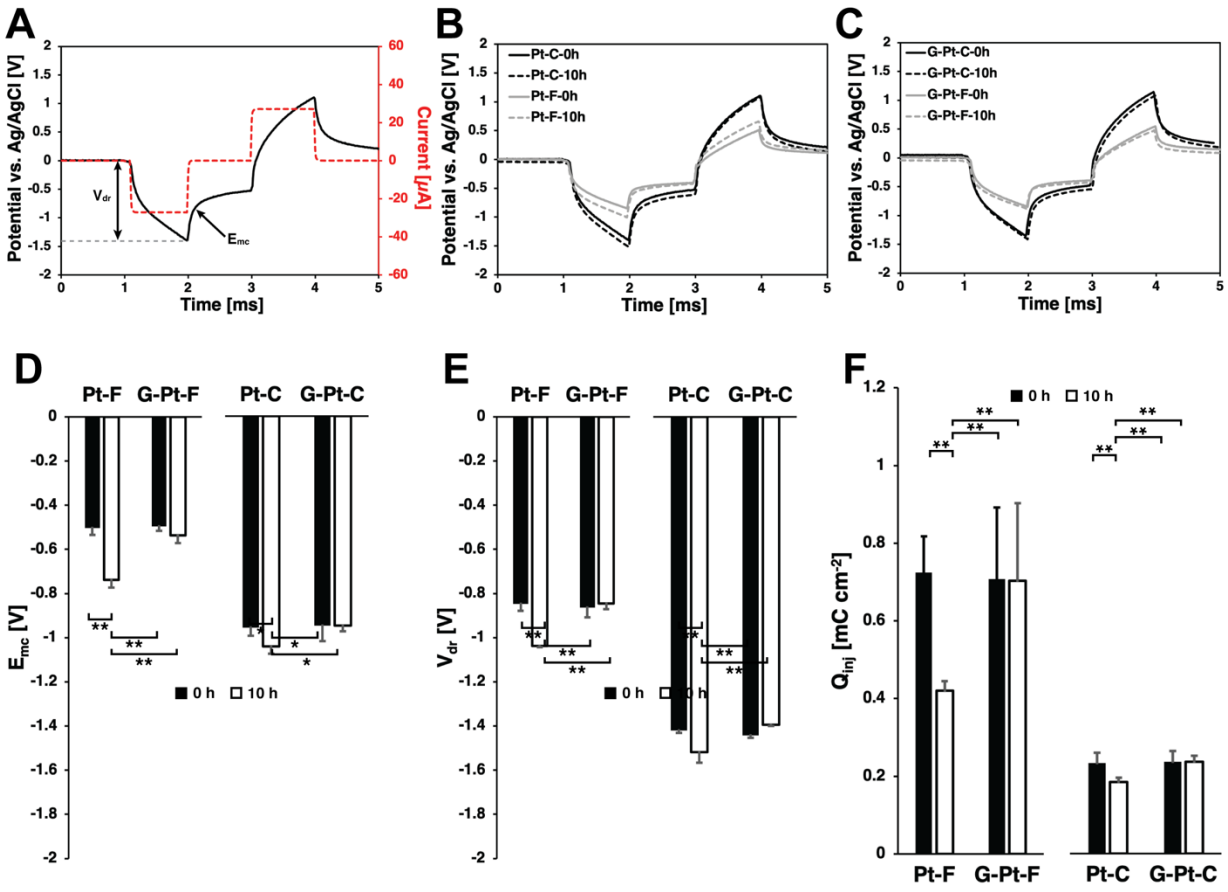

Figure 4.8: Voltage transient measurement. (A) Representative voltage transient of microelectrode with biphasic, symmetrical current pulse at 50 Hz frequency. (B) Voltage transients from Pt microelectrodes with circular and fractal shape before and after 10 h stimulation. (C) Voltage transients from G-Pt microelectrodes with circular and fractal shape before and after 10 h stimulation. (D) Maximum negative potential excursion. (E) Driving voltage from the microelectrodes. (F) Charge injection limit (* for $p < 0.05$, and ** for $p < 0.01$).

4.6 Conclusions and Discussion

From these results, we conclude the following: (1) long-term stimulation of Pt microelectrodes can result in dissolution-induced electrode degradation and failure; (2) fractal microelectrodes have significantly superior charge transfer characteristics than simple circular design; (3) fractal microelectrodes are more susceptible to stimulation-induced dissolution; (4) however, graphene monolayer can significantly reduce the stimulation-induced dissolution in Pt microelectrodes. Taken together, our results suggest that G-Pt fractal microelectrodes may provide an electrochemically more stable interface for neural stimulation. In the future, we plan to verify the long- term reliability and the robustness of these graphene coating and to confirm these finding using in vitro and in vivo models.

5. CONCLUSIONS AND FUTURE WORKS

5.1 Summary

Self-Clearing Smart GDD

In Chapter 2, we presented a clinical non-invasive solution for clearing of GDDs. The occlusion of the lumen of the tube due to biofoulings is one of the most common complications for GDDs. Once the GDD is implanted, the surface of the device is immediately covered with interstitial proteins such as albumin, fibrinogen, and IgG, which initiates foreign body responses resulting thick encapsulation of the device. Especially, the tube part of the GDD shunt with a diameter of 50 – 200 μm can be blocked by the blood clots, the posterior capsule, or vitreous humor. Additional surgical intervention is required to remove the blockage, which may double the total cost of the treatment with additional risks to the patient. To combat the problems associated with biofouling, we placed microactuators in the middle of the microchannel, which can mechanically clear the surface of the channel and ultimately vary the AH flow resistance.

We customized a maskless photolithography setup for rapid prototyping of various designs and arrangements of microactuators without the cost and time delay to order several masks for photolithography. We used a commercially available projector with the lens and microscope aligned between the sample stage and the projector to achieve micro-scale patterns. The photolithography patterns can be easily edited using Microsoft PowerPoint. Cu-cladded LCP was used to maximize simplicity and fabrication speed by using the Cu layer as a seed layer for the Ni electroplating. The actuator pattern was defined using an RIE and remaining Cu was etched by a chemical etchant. The Ni pattern on the microactuator was coated with 100 nm thick Ti to improve biocompatibility.

The successful application requires the microactuator to remotely actuate in a controlled external magnetic field. To precisely control the magnetic field density, we used an electromagnetic coil. The LCP-based thin film microactuator can be deflected over 60 degrees in static magnetic field, which follows theoretical estimation. A primary resonant frequency around 20 Hz was measured in PBS using our customized laser deflecting setup. In addition, mechanical fatigue was evaluated to confirm that our actuator has good mechanical reliability from extended

actuation. The results showed that there was no cracks or visible damage on the microactuators and no shift in the resonant frequency after 10.9 million actuation cycles.

Serum albumin non-specifically binds onto the implant surface within minutes after the implantation and initiate foreign body responses. We hypothesis that if serum albumin can be removed from the surface of GDD tube, the occlusion of the tube by biofoulings may be suppressed. Therefore, protein clearing capability was evaluated using fluorescence labeled bovine serum albumin (BSA-FITC). The fluorescence intensity of BSA-FITC adsorbed on the microactuators was quantified to compare the amount of proteins on the device before and after the actuation. We demonstrated that the actuation significantly reduced the amount of the adsorbed proteins from the device surface. The lumen of microtube was also cleaned by the inserted microactuators due to the shear stress generated by the actuation.

Electrode design for efficient electrical neurostimulation

It is challenging to achieve high charge transfer capability using microscale electrodes owing to their increased impedance and charge transfer resistance. Although electrode designs with high PSA ratio have previously been suggested to increase the charge injection limit, it is still not clear how PSA ratio of the microelectrodes affect the charge transfer process. In Chapter 3, to investigate the role of electrode geometry in terms of PSA ratio and shape, we designed four types of electrodes (circular, fractal, serpentine I, and serpentine II) with identical surface area but different PSA ratios. Using the FEM simulation, we evaluated the current density on the electrode surface with applying the constant voltage (–0.6 V), and the impedance in frequency range from 10 Hz to 0.1 MHz by applying 10 mV AC voltage perturbation. The results indicate that the fractal design can inject the highest amount of current and lowest solution resistance.

In Chapter 3, the electrochemical performance of the electrodes with different designs was evaluated using CV, EIS, and voltage transients. With CV, we can identify the presence of electrochemical reactions and charge storage capacity, which is the total amount of charge available for a single stimulation pulse. The voltammographs showed that fractal, serpentine I, and serpentine II designs all have a lower cathodic current response peaks than the circular electrode even though they have same the surface area. Furthermore, CSC values for fractal electrodes were significantly higher than serpentine I sharing the same PSA and SA with the fractal design. EIS

data indicated that the fractal design has the lowest impedance due to the advantage in chemical diffusion on microelectrode related to the Faradaic charge transfer. The charge injection limits of the electrodes were compared by voltage transient responses with different current pulse amplitudes. These results suggest that the fractal electrode is the most efficient design to increase charge injection limit of the microelectrodes.

Graphene protection layer to prevent corrosion in Pt electrode

In Chapter 4, we applied the graphene protection layer to enhance the reliability of the Pt microelectrode with fractal shape with increased current density at the edges and the corners. Pt is one of the standard materials for neurostimulation due to its excellent charge transfer capability and biocompatibility. However, Pt undergoes irreversible electrochemical reactions during neurostimulation, which can lead to delamination, cracks, and corrosion of the thin Pt film. Furthermore, these reactions produce cytotoxic byproducts that can damage the surrounding neural tissues. Although we suggested that the fractal microelectrodes have a better charge transfer performance than conventional circular designs, Pt fractal microelectrodes had an accelerated dissolution rate than the circular ones due to its increased current injection at the edges. Therefore, there is a need for a technique to develop more reliable neurostimulating microelectrodes.

In Chapter 5, we demonstrated that the graphene monolayer coated on the Pt microelectrode can significantly reduce the Pt dissolution while maintaining high charge transfer capability of these microelectrodes. To evaluate the corrosion prevention performance of the graphene layer, we fabricated bare Pt and graphene-coated Pt microelectrodes with circular and fractal designs. The monolayer graphene layer was transferred to the electrode substrate and patterned using photolithography and RIE. After a continuous 10 h stimulation with injected charge density of 0.35 mC cm^{-2} at 50 Hz frequency, the amount of Pt dissolved in the PBS solution was measured using inductively coupled plasma mass spectrometry. Our results showed that the graphene protection layer reduced >97 % for fractal Pt microelectrodes while they maintained the superior charge transfer characteristics. In addition, there was no significant changes in electrochemical characteristics of the graphene-coated Pt microelectrodes before and after the 10 h stimulation period.

5.2 Future Works

This work represents our efforts to improve the reliability of various implantable devices against biofouling and electrochemical corrosion. However, biotic and abiotic failures of implantable devices occur concurrently and cannot be isolated from one another. It may possible to prevent different kinds of failures in implantable devices by combining our strategies in one system. For example, we could develop a magnetically actuated implantable soft robot with neurostimulation and neural recording electrodes that can be remotely re-positioned *in situ* in a precise and controlled manner. This multifunctional device may be used to not only record and stimulate but prevent biofouling-related performance degradation (Fig. 5.1). Furthermore, graphene protection layer could significantly reduce the corrosion of the working electrodes to withstand the prolonged electrical stimulation *in vivo* without requiring surgical intervention to replace the devices.

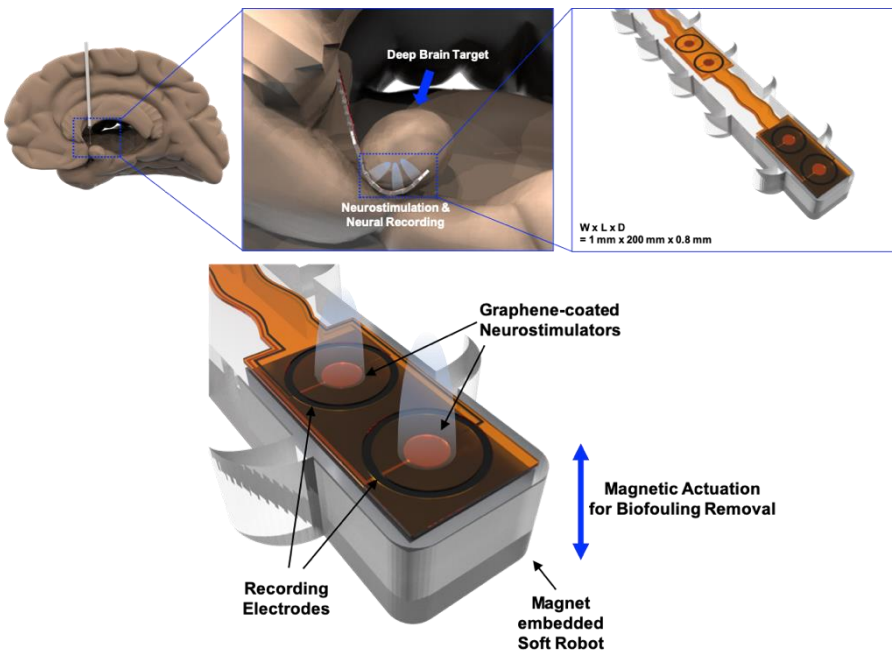

Figure 5.1: Magnetic soft robot combined with the neural probe consisted of graphene-coated microelectrodes to enhance the reliability.

REFERENCES

[1] P. Bendel, *Biomedical applications of metals*, vol. 221, no. July. 2005.

[2] E. Meng and R. Sheybani, "Insight: Implantable medical devices," *Lab Chip*, vol. 14, no. 17, pp. 3233–3240, 2014.

[3] A. C. R. Grayson *et al.*, "A BioMEMS review: MEMS technology for physiologically integrated devices," *Proc. IEEE*, vol. 92, no. 1, pp. 6–21, 2004.

[4] A. Dehennis, M. A. Mortellaro, and S. Ioacara, "Multisite study of an implanted continuous glucose sensor over 90 days in patients with diabetes mellitus," *J. Diabetes Sci. Technol.*, vol. 9, no. 5, pp. 951–956, 2015.

[5] M. Mortellaro and A. DeHennis, "Performance characterization of an abiotic and fluorescent-based continuous glucose monitoring system in patients with type 1 diabetes," *Biosens. Bioelectron.*, vol. 61, pp. 227–231, 2014.

[6] M. G. Allen, "Micromachined endovascularly-implantable wireless aneurysm pressure sensors: From concept to clinic," *Dig. Tech. Pap. - Int. Conf. Solid State Sensors Actuators Microsystems, TRANSDUCERS '05*, vol. 1, pp. 275–278, 2005.

[7] L. Yu, B. J. Kim, and E. Meng, "Chronically implanted pressure sensors: Challenges and state of the field," *Sensors (Switzerland)*, vol. 14, no. 11, pp. 20620–20644, 2014.

[8] P. J. Chen, D. C. Rodger, S. Saati, M. S. Humayun, and Y. C. Tai, "Microfabricated implantable parylene-based wireless passive intraocular pressure sensors," *J. Microelectromechanical Syst.*, vol. 17, no. 6, pp. 1342–1351, 2008.

[9] J. M. Anderson, A. Rodriguez, and D. T. Chang, "Foreign body reaction to biomaterials," *Semin. Immunol.*, vol. 20, no. 2, pp. 86–100, 2008.

[10] Y. K. Kim, E. Y. Chen, and W. F. Liu, "Biomolecular strategies to modulate the macrophage response to implanted materials," *J. Mater. Chem. B*, vol. 4, no. 9, pp. 1600–1609, 2015.

[11] Y. Onuki, U. Bhardwaj, F. Papadimitrakopoulos, and D. J. Burgess, "A review of the biocompatibility of implantable devices: Current challenges to overcome foreign body response," *J. Diabetes Sci. Technol.*, vol. 2, no. 6, pp. 1003–1015, 2008.

[12] D. W. Grainger, "All charged up about implanted biomaterials," *Nat. Biotechnol.*, vol. 31, no. 6, pp. 507–509, 2013.

[13] M. Esposito, C. Kennergren, N. Holmström, S. Nilsson, J. Eckerdal, and P. Thomsen, "Morphologic and immunohistochemical observations of tissues surrounding retrieved transvenous pacemaker leads," *J. Biomed. Mater. Res.*, vol. 63, no. 5, pp. 548–558, 2002.

[14] R. Farra *et al.*, "First-in-human testing of a wirelessly controlled drug delivery microchip," *Sci. Transl. Med.*, vol. 4, no. 122, 2012.

[15] B. W. Hanak, E. F. Ross, C. A. Harris, S. R. Browd, and W. Shain, "Toward a better understanding of the cellular basis for cerebrospinal fluid shunt obstruction: Report on the construction of a bank of explanted hydrocephalus devices," *J. Neurosurg. Pediatr.*, vol. 18, no. 2, pp. 213–223, 2016.

[16] E. Sharkawi *et al.*, "Systematic occlusion of shunts: Control of early postoperative iop and hypotony-related complications following glaucoma shunt surgery," *J. Glaucoma*, vol. 25, no. 1, pp. 54–61, 2016.

[17] M. Tanito, I. Sano, and A. Ohira, "A case report of progressive obstruction of Ex-PRESS miniature glaucoma shunt after transient flat anterior chamber and treatment using Nd:YAG laser," *BMC Ophthalmol.*, vol. 15, no. 1, pp. 4–6, 2015.

[18] J. Gu, Y. Zhang, J. Zhai, Z. Ou, and J. Chen, "Nd:YAG Laser for Ahmed Tube Shunt Blockage in Patients Implanted with Boston Type I Keratoprosthesis," *Ophthalmol. Ther.*, vol. 8, no. 2, pp. 333–339, 2019.

[19] R. Atoui, S. Mohammadi, and D. Shum-Tim, "Surgical extraction of occluded stents: when stenting becomes a problem," *Interact. Cardiovasc. Thorac. Surg.*, vol. 9, no. 4, pp. 736–738, 2009.

[20] W. J. Kao, A. Hiltner, J. M. Anderson, and G. A. Lodoen, "Theoretical analysis of in vivo macrophage adhesion and foreign body giant cell formation on strained poly(etherurethane urea) elastomers," *J. Biomed. Mater. Res.*, vol. 28, pp. 819–829, 1994.

[21] E. M. Christenson, J. M. Anderson, and A. Hiltner, "Oxidative mechanisms of poly(carbonate urethane) and poly(ether urethane) biodegradation: In vivo and in vitro correlations," *J. Biomed. Mater. Res. - Part A*, vol. 70, no. 2, pp. 245–255, 2004.

[22] M. Gerritsen *et al.*, "Influence of inflammatory cells and serum on the performance of implantable glucose sensors," *J. Biomed. Mater. Res.*, vol. 54, no. 1, pp. 69–75, 2001.

[23] C. L. Freeman, K. G. Mayhan, G. J. Picha, and C. K. Colton, "A study of the mass transport resistance of glucose across rat capsular membranes," in *Materials Research Society*, 1989, vol. 110, pp. 773–778.

[24] N. Wisniewski, B. Klitzman, B. Miller, and W. M. Reichert, "Decreased analyte transport through implanted membranes: Differentiation of biofouling from tissue effects," *J. Biomed. Mater. Res.*, vol. 57, no. 4, pp. 513–521, 2001.

[25] B. W. Hanak, E. F. Ross, C. A. Harris, S. R. Browd, and W. Shain, "Toward a better understanding of the cellular basis for cerebrospinal fluid shunt obstruction: report on the construction of a bank of explanted hydrocephalus devices," *J. Neurosurg. Pediatr.*, vol. 18, no. 2, pp. 213–223, 2016.

[26] J. Kestle *et al.*, "Long-Term Follow-Up Data from the Shunt Design Trial," *Pediatr. Neurosurg.*, vol. 84113, pp. 230–236, 2001.

[27] P. G. Christakis *et al.*, "The Ahmed Versus Baerveldt study: One-year treatment outcomes," *Ophthalmology*, vol. 118, no. 11, pp. 2180–2189, 2011.

[28] S. Chen, L. Li, C. Zhao, and J. Zheng, "Surface hydration: Principles and applications toward low-fouling/nonfouling biomaterials," *Polymer (Guildf).*, vol. 51, no. 23, pp. 5283–5293, 2010.

[29] D. Hutanu, "Recent Applications of Polyethylene Glycols (PEGs) and PEG Derivatives," *Mod. Chem. Appl.*, vol. 02, no. 02, pp. 2–7, 2014.

[30] J. S. Chung *et al.*, "Silver-perfluorodecanethiolate complexes having superhydrophobic, antifouling, antibacterial properties," *J. Colloid Interface Sci.*, vol. 366, no. 1, pp. 64–69, 2012.

[31] G. B. Hwang, K. Page, A. Patir, S. P. Nair, E. Allan, and I. P. Parkin, "The Anti-Biofouling Properties of Superhydrophobic Surfaces are Short-Lived," *ACS Nano*, vol. 12, no. 6, pp. 6050–6058, 2018.

[32] S. Jiang and Z. Cao, "Ultralow-fouling, functionalizable, and hydrolyzable zwitterionic materials and their derivatives for biological applications," *Adv. Mater.*, vol. 22, no. 9, pp. 920–932, 2010.

[33] Y. Chen and S. Thayumanavan, "Amphiphilicity in homopolymer surfaces reduces nonspecific protein adsorption," *Langmuir*, vol. 25, no. 24, pp. 13795–13799, 2009.

[34] L. E. Moore, R. G. Ledder, P. Gilbert, and A. J. McBain, "In vitro study of the effect of cationic biocides on bacterial population dynamics and susceptibility," *Appl. Environ. Microbiol.*, vol. 74, no. 15, pp. 4825–4834, 2008.

[35] H. Murata, R. R. Koepsel, K. Matyjaszewski, and A. J. Russell, "Permanent, non-leaching antibacterial surfaces-2: How high density cationic surfaces kill bacterial cells," *Biomaterials*, vol. 28, no. 32, pp. 4870–4879, 2007.

[36] E. I. Rabea, M. E. T. Badawy, C. V. Stevens, G. Smagghe, and W. Steurbaut, "Chitosan as antimicrobial agent: Applications and mode of action," *Biomacromolecules*, vol. 4, no. 6, pp. 1457–1465, 2003.

[37] J. L. Harding and M. M. Reynolds, "Combating medical device fouling," *Trends Biotechnol.*, vol. 32, no. 3, pp. 140–146, 2014.

[38] R. Gref *et al.*, "'Stealth' corona-core nanoparticles surface modified by polyethylene glycol (PEG): Influences of the corona (PEG chain length and surface density) and of the core composition on phagocytic uptake and plasma protein adsorption," *Colloids Surfaces B Biointerfaces*, vol. 18, no. 3–4, pp. 301–313, 2000.

[39] P. Y. J. Yeh, J. N. Kizhakkedathu, J. D. Madden, and M. Chiao, "Electric field and vibration-assisted nanomolecule desorption and anti-biofouling for biosensor applications," *Colloids Surfaces B Biointerfaces*, vol. 59, no. 1, pp. 67–73, 2007.

[40] V. Pepakayala, J. Stein, and Y. Gianchandani, "Resonant magnetoelastic microstructures for wireless actuation of liquid flow on 3D surfaces and use in glaucoma drainage implants," *Microsystems Nanoeng.*, vol. 1, no. 0, p. 15032, 2015.

[41] S. Pan, H. Zhang, W. Liu, Y. Wang, W. Pang, and X. Duan, "Biofouling Removal and Protein Detection Using a Hypersonic Resonator," *ACS Sensors*, vol. 2, no. 8, pp. 1175–1183, 2017.

[42] B. N. Johnson and R. Mutharasan, "Reduction of nonspecific protein adsorption on cantilever biosensors caused by transverse resonant mode vibration," *Analyst*, vol. 139, no. 5, pp. 1112–1120, 2014.

[43] W. H. Maisel *et al.*, "Pacemaker and ICD generator malfunctions: Analysis of food and drug administration annual reports," *J. Am. Med. Assoc.*, vol. 295, no. 16, pp. 1901–1906, 2006.

[44] K. Qian, M. O. De Beeck, G. Bryce, K. Malachowski, and C. Van Hoof, "Novel miniaturized packaging for implantable electronic devices," *2012 IEEE Int. Interconnect Technol. Conf. IITC 2012*, pp. 3–5, 2012.

[45] G. Manivasagam, D. Dhinasekaran, and A. Rajamanickam, "Biomedical Implants: Corrosion and its Prevention - A Review," *Recent Patents Corros. Sci.*, vol. 2, no. 1, pp. 40–54, 2010.

[46] N. Nioradze, R. Chen, J. Kim, M. Shen, P. Santhosh, and S. Amemiya, "Origins of nanoscale damage to glass-sealed platinum electrodes with submicrometer and nanometer size," *Anal. Chem.*, vol. 85, no. 13, pp. 6198–6202, 2013.

[47] J. Gimsa, B. Habel, U. Schreiber, U. Van Rienen, U. Strauss, and U. Gimsa, "Choosing electrodes for deep brain stimulation experiments-electrochemical considerations," *J. Neurosci. Methods*, vol. 142, no. 2, pp. 251–265, 2005.

[48] C. Marras *et al.*, "Morphological and chemical analysis of a deep brain stimulation electrode explanted from a dystonic patient," *J. Neural Transm.*, vol. 120, no. 10, pp. 1425–1431, 2013.

[49] M. M. Mazumder, S. De, S. Trigwell, N. Ali, M. K. Mazumder, and J. L. Mehta, "Corrosion resistance of polyurethane-coated Nitinol cardiovascular stents," *J. Biomater. Sci. Polym. Ed.*, vol. 14, no. 12, pp. 1351–1362, 2003.

[50] M. F. Maitz and N. Shevchenko, "Plasma-immersion ion-implanted nitinol surface with depressed nickel concentration for implants in blood," *J. Biomed. Mater. Res. - Part A*, vol. 76, no. 2, pp. 356–365, 2006.

[51] X. Xiao *et al.*, "In vitro and in vivo evaluation of ultrananocrystalline diamond for coating of implantable retinal microchips," *J. Biomed. Mater. Res. - Part B Appl. Biomater.*, vol. 77, no. 2, pp. 273–281, 2006.

[52] O. Auciello and A. V. Sumant, "Status review of the science and technology of ultrananocrystalline diamond (UNCD^{TM}) films and application to multifunctional devices," *Diam. Relat. Mater.*, vol. 19, no. 7–9, pp. 699–718, 2010.

[53] O. Auciello, P. Gurman, M. B. Guglielmotti, D. G. Olmedo, A. Berra, and M. J. Saravia, "Biocompatible ultrananocrystalline diamond coatings for implantable medical devices," *MRS Bull.*, vol. 39, no. 7, pp. 621–629, 2014.

[54] A. A. El Hadad *et al.*, "Biocompatibility and corrosion protection behaviour of hydroxyapatite sol-gel-derived coatings on Ti6Al4V alloy," *Materials (Basel).*, vol. 10, no. 2, 2017.

[55] J. D. Heckman *et al.*, "Bone morphogenetic protein but not transforming growth factor-β enhances bone formation in canine diaphyseal nonunions implanted with a biodegradable composite polymer," *J. Bone Jt. Surg. - Ser. A*, vol. 81, no. 12, pp. 1717–1729, 1999.

[56] J. R. Glass, K. T. Dickerson, K. Stecker, and J. W. Polarek, "Characterization of a hyaluronic acid-Arg-Gly-Asp peptide cell attachment matrix," *Biomaterials*, vol. 17, no. 11, pp. 1101–1108, 1996.

[57] T. M. Yue, J. K. Yu, Z. Mei, and H. C. Man, "Excimer laser surface treatment of Ti-6Al-4V alloy for corrosion resistance enhancement," *Mater. Lett.*, vol. 52, no. 3, pp. 206–212, 2002.

[58] M. Geetha, U. K. Mudali, N. D. Pandey, R. Asokamani, and B. Raj, "Microstructural and corrosion evaluation of laser surface nitrided Ti-13Nb-13Zr alloy," *Surf. Eng.*, vol. 20, no. 1, pp. 68–74, 2004.

[59] M. M. Civan and A. D. C. Macknight, "The ins and outs of aqueous humour secretion," *Exp. Eye Res.*, vol. 78, no. 3, pp. 625–631, 2004.

[60] M. Goel, R. G. Picciani, R. K. Lee, and S. K. Bhattacharya, "Aqueous Humor Dynamics: A Review," *Open Ophthalmol. J.*, vol. 4, no. 1, pp. 52–59, 2010.

[61] T. Seiler and J. Wollensak, "The resistance of the trabecular meshwork to aqueous humor outflow," *Clin. Exp. Ophthalmol.*, vol. 229, no. 2, pp. 265–270, 1982.

[62] B. T. Gabelt and P. L. Kaufman, "Changes in aqueous humor dynamics with age and glaucoma," *Prog. Retin. Eye Res.*, vol. 24, no. 5, pp. 612–637, 2005.

[63] H. H. Mark, "Aqueous Humor Dynamics in Historical Perspective," *Surv. Ophthalmol.*, vol. 55, no. 1, pp. 89–100, 2010.

[64] D. A. Lee and E. J. Higginbotham, “Glaucoma and its treatment,” *Am J Heal. Syst Pharm*, vol. 62, no. 7, pp. 691–699, 2005.

[65] Silvio P. Mariotti, “Global Data on Visual Impairments 2020,” 2010.

[66] H. A. Quigley and A. T. Broman, “The number of people with glaucoma worldwide in 2010 and 2020,” *Br. J. Ophthalmol.*, vol. 90, no. 3, pp. 262–267, 2006.

[67] Y. C. Tham, X. Li, T. Y. Wong, H. A. Quigley, T. Aung, and C. Y. Cheng, “Global prevalence of glaucoma and projections of glaucoma burden through 2040: A systematic review and meta-analysis,” *Ophthalmology*, vol. 121, no. 11, pp. 2081–2090, 2014.

[68] A. T. Broman *et al.*, “Estimating the rate of progressive visual field damage in those with open-angle glaucoma, from cross-sectional data,” *Investig. Ophthalmol. Vis. Sci.*, vol. 49, no. 1, pp. 66–76, 2008.

[69] F. Ko *et al.*, “Diabetes, Triglyceride Levels, and Other Risk Factors for Glaucoma in the National Health and Nutrition Examination Survey 2005–2008,” *Investig. Opthalmology Vis. Sci.*, vol. 57, no. 4, p. 2152, 2016.

[70] S. Drance, D. R. Anderson, M. Schulzer, and Collaborative Normal-Tension Glaucoma Study Group, “Risk factors for progression of visual field abnormalities in normal-tension glaucoma.,” *Am. J. Ophthalmol.*, vol. 131, no. 6, pp. 699–708, 2001.

[71] B. Muñoz *et al.*, “Causes of blindness and visual impairment in a population of older Americans: The Salisbury Eye Evaluation Study.,” *Arch. Ophthalmol.*, vol. 118, no. 6, pp. 819–825, 2000.

[72] P. Gupta, D. Zhao, E. Guallar, F. Ko, M. V Boland, and D. S. Friedman, “Prevalence of Glaucoma in the United States: The 2005– 2008 National Health and Nutrition Examination Survey,” *Invest Ophthalmol Vis Sci*, vol. 57, pp. 2905–2913, 2016.

[73] D. B. Kenneth Schwartz, “Current management of glaucoma,” *Curr. Opin. Ophthalmol.*, vol. 8, no. 6, pp. 339–342, 2003.

[74] L. Z. Bito, “Prostaglandins: a new approach to glaucoma management with a new, intriguing side effect.,” *Surv. Ophthalmol.*, vol. 41 Suppl 2, no. February, pp. S1-14, 1997.

[75] T. J. Zimmerman and William P. BogerIII, “The Beta-Adrenergic Blocking Agents and the Treatment of Glaucoma,” *Surv. Ophthalmol.*, vol. 23, no. 6, pp. 347–362, 1979.

[76] R. L. Coakes and R. F. Brubaker, “The Mechanism of Timolol in Lowering Intraocular Pressure,” *Arch. Ophthalmol.*, vol. 96, no. 11, p. 2045, 1978.

[77] E. Strahlman, R. Tipping, R. Vogel, and the I. D. S. Group, “A Double-Masked, Randomized 1-Year Study Comparing Dorzolamide (Trusopt), Timolol, and Betaxolol,” *J. Chem. Inf. Model.*, vol. 53, no. 9, pp. 1689–1699, 2013.

[78] S. Bloch, A. R. Rosenthal, L. Friedman, and P. Caldarolla, “Patient compliance in glaucoma,” *Br. J. Ophthalmol.*, vol. 61, pp. 531–534, 1977.

[79] R. K. Bansal and J. C. Tsai, “Compliance / Adherence to Glaucoma Medications — A Challenge,” *J. Curr. Glaucoma Pract.*, vol. 1, no. 2, pp. 22–25, 2007.

[80] E. Jones, J. Clarke, and P. T. Khaw, “Recent advances in trabeculectomy technique Recent advances in trabeculectomy technique,” *Curr. Opin. Ophthalmol.*, vol. 16, no. May, pp. 107–113, 2005.

[81] D. Mchugh, J. Marshall, J. Timothy, P. A. M. Hamilton, and A. Raven, “Diode laser trabeculoplasty (DLT) for primary open-angle glaucoma and ocular hypertension,” *Br. J. Ophthalmol.*, vol. 74, pp. 743–747, 1990.

[82] M. S. Juzych, M. R. Banitt, B. A. Hughes, C. Kim, M. T. Goulas, and D. H. Shin, “Comparison of Long-term Outcomes of Selective Laser Trabeculoplasty versus Argon Laser Trabeculoplasty in Open-Angle Glaucoma,” *Ophthalmology*, vol. 111, pp. 1853–1859, 2004.

[83] R. C. Spurny and C. M. Lederer, “Krypton Laser Trabeculoplasty A Clinical,” *Arch.Ophthalmol.*, vol. 102, pp. 1626–1628, 1984.

[84] S. Melamed, J. Pei, and D. L. Epstein, “Delayed Response to Argon Laser Trabeculoplasty in Monkeys Morphological and Morphometric Analysis,” *Arch.Ophthalmol.*, vol. 104, pp. 1078–1083, 1986.

[85] S. J. Gedde, J. C. Schiffman, W. J. Feuer, L. W. Herndon, J. D. Brandt, and D. L. Budenz, “Treatment outcomes in the Tube Versus Trabeculectomy (TVT) study after five years of follow-up.,” *Am. J. Ophthalmol.*, vol. 153, no. 5, pp. 789-803.e2, 2012.

[86] E. M. Ceballos, R. K. Parrish, and J. C. Schiffman, “Outcome of Baerveldt glaucoma drainage implants for the treatment of uveitic glaucoma,” *Ophthalmology*, vol. 109, no. 12, pp. 2256–2260, 2002.

[87] R. S. Ayyala, J. L. Duarte, and N. Sahiner, “Glaucoma drainage devices: state of the art.,” *Expert Rev. Med. Devices*, vol. 3, no. 4, pp. 509–521, 2006.

[88] S. Melamed and P. M. Fiore, “Molten Implant Surgery in Refractory Glaucoma,” *Surv. Ophthalmol.*, vol. 34, no. 6, pp. 441–448, 1990.

[89] T. L. Rittenbach, “Proptosis from a baerveldt tube shunt implant.,” *Optom. Vis. Sci.*, vol. 91, no. 6, pp. e145-8, 2014.

[90] S. R. Sarkisian, “Tube shunt complications and their prevention.,” *Curr. Opin. Ophthalmol.*, vol. 20, no. 2, pp. 126–130, 2009.

[91] C. Souza, D. H. Tran, J. Loman, S. K. Law, A. L. Coleman, and J. Caprioli, "Long-term outcomes of Ahmed glaucoma valve implantation in refractory glaucomas.," *Am. J. Ophthalmol.*, vol. 144, no. 6, pp. 893–900, 2007.

[92] S. J. Gedde, L. W. Herndon, J. D. Brandt, D. L. Budenz, W. J. Feuer, and J. C. Schiffman, "Surgical Complications in the Tube Versus Trabeculectomy Study During the First Year of Follow-up," *Am. J. Ophthalmol.*, vol. 143, no. 1, pp. 804–814, 2007.

[93] T. Schlote, F. Ziemssen, and K. U. Bartz-Schmidt, "Pars plana-modified Ahmed Glaucoma Valve for treatment of refractory glaucoma: A pilot study," *Graefe's Arch. Clin. Exp. Ophthalmol.*, vol. 244, no. 3, pp. 336–341, 2006.

[94] R. A. Hill, A. Pirouzian, and L. H. Liaw, "Pathophysiology of and prophylaxis against late Ahmed Glaucoma Valve occlusion," *Am. J. Ophthalmol.*, vol. 129, no. 5, pp. 608–612, 2000.

[95] L. Choritz, K. Koynov, G. Renieri, K. Barton, N. Pfeiffer, and H. Thieme, "Surface topographies of glaucoma drainage devices and their influence on human tenon fibroblast adhesion," *Investig. Ophthalmol. Vis. Sci.*, vol. 51, no. 8, pp. 4047–4053, 2010.

[96] J. V. et al. Ihlenfeld, "Transient in vivo thrombus deposition onto polymeric biomaterials: Role of plasma fibronectin," *Trans. Am. Soc. Artif. Intern. Organs*, vol. XXIV, pp. 727–735, 1978.

[97] W. Kenneth Ward, "A review of the foreign-body response to subcutaneously-implanted devices: the role of macrophages and cytokines in biofouling and fibrosis.," *J. Diabetes Sci. Technol.*, vol. 2, no. 5, pp. 768–77, 2008.

[98] A. L. Coleman *et al.*, "Initial Clinical Experience With the Ahmed Glaucoma Valve Implant in Pediatric Patients," *Arch. Ophthalmol.*, vol. 115, no. 2, p. 186, 1997.

[99] S. Dubey, J. Pegu, M. Agarwal, and A. Agrawal, "Vitreous occlusion of tube implant in a phakic patient with traumatic glaucoma," *Oman J. Ophthalmol.*, vol. 7, no. 3, pp. 2014–2016, 2014.

[100] M. McClintock and M. W. MacCumber, "Lowered intraocular pressure in a glaucoma patient after intravitreal injection of ocriplasmin," *Clin. Ophthalmol.*, vol. 9, pp. 1995–1998, 2015.

[101] P. G. Christakis *et al.*, "The ahmed versus baerveldt study: Three-year treatment outcomes," *Ophthalmology*, vol. 120, no. 11, pp. 2232–2240, 2013.

[102] W. F. Tsai, Y. C. Chen, and C. Y. Su, "Treatment of vitreous floaters with neodymium YAG Laser," *Br. J. Ophthalmol.*, vol. 77, no. 8, pp. 485–488, 1993.

[103] E. M. Kanner, P. A. Netland, S. R. Sarkisian, and H. Du, "Ex-PRESS miniature glaucoma device implanted under a scleral flap alone or combined with phacoemulsification cataract surgery," *J. Glaucoma*, vol. 18, no. 6, pp. 488–491, 2009.

[104] M. Tanito, I. Sano, and A. Ohira, "A case report of progressive obstruction of Ex-PRESS miniature glaucoma shunt after transient flat anterior chamber and treatment using Nd:YAG laser," *BMC Ophthalmol.*, vol. 15, no. 1, pp. 4–6, 2015.

[105] J. Song, "Complications of selective laser trabeculoplasty: A review," *Clin. Ophthalmol.*, vol. 10, pp. 137–143, 2016.

[106] C. I. Perez, S. Chansangpetch, Y. C. Hsia, and S. C. Lin, "Use of Nd:YAG laser to recanalize occluded Cypass Micro-Stent in the early post-operative period," *Am. J. Ophthalmol. Case Reports*, vol. 10, pp. 114–116, 2018.

[107] E. H. Koo, L. J. Haddock, N. Bhardwaj, and J. A. Fortun, "Cataracts induced by neodymium-yttrium-aluminium-garnet laser lysis of vitreous floaters," *Br. J. Ophthalmol.*, vol. 101, no. 6, pp. 709–711, 2017.

[108] P. Hahn, E. W. Schneider, H. Tabandeh, R. W. Wong, and G. G. Emerson, "Reported complications following laser vitreolysis," *JAMA Ophthalmol.*, vol. 135, no. 9, pp. 973–976, 2017.

[109] M. F. Smith and J. W. Doyle, "Use of tissue plasminogen activator to revive blebs following intraocular surgery.," *Arch. Ophthalmol.*, vol. 119, no. 6, pp. 809–12, 2001.

[110] D. Raczyńska, P. Lipowski, K. Zorena, A. Skorek, and P. Glasner, "Enzymatic vitreolysis with recombinant tissue plasminogen activator for vitreomacular traction," *Drug Des. Devel. Ther.*, vol. 9, pp. 6259–6268, 2015.

[111] A. H. Zalta, C. P. Sweeney, A. K. Zalta, and A. H. Kaufman, "Intracameral Tissue Plasminogen Activator Use in a Large Series of Eyes With Valved Glaucoma Drainage Implants," *Arch. Ophthalmol.*, vol. 120, no. 11, p. 1487, 2002.

[112] P. A. Sidoti, E. N. Morinelli, D. K. Heuer, D. C. Lundy, P. P. Lee, and D. S. Minckler, "Tissue Plasminogen Activator and Glaucoma Drainage," *J. Glaucoma*, vol. 4, no. 4, pp. 258–262, 1995.

[113] D. C. Lundy, P. Sidoti, T. Winarko, D. Minckler, and D. K. Heuer, "Intracameral tissue plasminogen activator after glaucoma surgery: Indications, effectiveness, and complications," *Ophthalmology*, vol. 103, no. 2, pp. 274–282, 1996.

[114] B. P. Leonard, "Based on Quadratic Upstream Interpolation," *Comput. Methods Appl. Mech. Eng.*, vol. 19, pp. 59–98, 1979.

[115] B. Alexandre and J. Chorin, "Numerical Solution of the Navier-Stokes Equations," *Math. Comput.*, vol. 22, no. 104, pp. 745–762, 1968.

[116] A. M. Ardekani, S. Dabiri, and R. H. Rangel, "Collision of multi-particle and general shape objects in a viscous fluid," *J. Comput. Phys.*, vol. 227, no. 24, pp. 10094–10107, 2008.

[117] W. C. Young and R. G. Budynas, *Roarks's Formulas for Stress and Strain*, 7th editio. New York: McGraw-Hill, 2002.

[118] J. W. Judy and R. S. Muller, "Magnetically Actuated, Addressable Microstructures," *IEEE J. Microelectromechanical Syst.*, vol. 6, pp. 249–256, 1997.

[119] D. J. Phares, G. T. Smedley, and R. C. Flagan, "The wall shear stress produced by the normal impingement of a jet on a flat surface," *J. Fluid Mech.*, vol. 418, pp. 351–375, 2000.

[120] J. W. Weisel, H. Shuman, and R. I. Litvinov, "Protein – protein unbinding induced by force : single-molecule studies," *Curr. Opin. Struct. Biol.*, vol. 13, pp. 227–235, 2003.

[121] P. Y. J. Yeh, J. N. Kizhakkedathu, J. D. Madden, and M. Chiao, "Electric field and vibration-assisted nanomolecule desorption and anti-biofouling for biosensor applications," *Colloids Surfaces B Biointerfaces*, vol. 59, no. 1, pp. 67–73, 2007.

[122] G. D. Meyer, J. M. Moran-Mirabal, D. W. Branch, and H. G. Craighead, "Nonspecific binding removal from protein microarrays using thickness shear mode resonators," *IEEE Sens. J.*, vol. 6, no. 2, pp. 254–261, 2006.

[123] X. Wang, J. Engel, and C. Liu, "Liquid crystal polymer for MEMS: processes and applications," *J. Micromechanics Microengineering*, vol. 13, pp. 628–633, 2003.

[124] K. Wang, C. Liu, S. Member, and D. M. Durand, "Oxide Sputtered on Liquid Crystal Polymer," *IEEE Trans. Biomed. Eng.*, vol. 56, no. 1, pp. 6–14, 2009.

[125] E. Y. Chow, A. L. Chlebowski, and P. P. Irazoqui, "A miniature-implantable RF-wireless active glaucoma intraocular pressure monitor," *IEEE Trans. Biomed. Circuits Syst.*, vol. 4, no. 6 PART 1, pp. 340–349, 2010.

[126] K. S. Min *et al.*, "A liquid crystal polymer-based neuromodulation system: An application on animal model of neuropathic pain," *Neuromodulation*, vol. 17, no. 2, pp. 160–169, 2014.

[127] S. Harkema *et al.*, "Effect of epidural stimulation of the lumbosacral spinal cord on voluntary movement, standing, and assisted stepping after motor complete paraplegia: A case study," *Lancet*, vol. 377, no. 9781, pp. 1938–1947, 2011.

[128] R. E. Ventura, L. J. Balcer, and S. L. Galetta, "The neuro-ophthalmology of head trauma," *Lancet Neurol.*, vol. 13, no. 10, pp. 1006–1016, 2014.

[129] A. Kral and A. Sharma, "Developmental neuroplasticity after cochlear implantation," *Trends Neurosci.*, vol. 35, no. 2, pp. 111–122, 2012.

[130] T. Cameron, "Safety and efficacy of spinal cord stimulation for the treatment of chronic pain: a 20-year literature review," *J Neurosurg*, vol. 100, no. 3 Suppl Spine, pp. 254–267, 2004.

[131] R. Fisher *et al.*, "Electrical stimulation of the anterior nucleus of thalamus for treatment of refractory epilepsy," *Epilepsia*, vol. 51, no. 5, pp. 899–908, 2010.

[132] V. Pikov, *Global market for implanted neuroprostheses*, 1st Editio., no. May. Sawston: Woodhead Publishing, 2015.

[133] J. D. Weiland and M. S. Humayun, "A biomimetic retinal stimulating array," *IEEE Eng. Med. Biol. Mag.*, vol. 24, no. 5, pp. 14–21, 2005.

[134] A. C. Patil and N. V Thakor, "Implantable neurotechnologies: a review of micro- and nanoelectrodes for neural recording," *Med. Biol. Eng. Comput.*, vol. 54, no. 1, pp. 23–44, 2016.

[135] P. J. Rossi *et al.*, "Proceedings of the Third Annual Deep Brain Stimulation Think Tank: A Review of Emerging Issues and Technologies," *Front. Neurosci.*, vol. 10, no. April, p. 119, 2016.

[136] Y. Jimbo and A. Kawana, "Electrical stimulation and recording from cultured neurons using a planar electrode array," *Bioelectrochemistry and Biioenergetics*, vol. 29, pp. 193–204, 1992.

[137] Y. Jimbo, N. Kasai, K. Torimitsu, T. Tateno, and H. P. C. Robinson, "A System for MEA-Based Multisite Stimulation," *IEEE Trans. Biomed. Eng.*, vol. 50, no. 2, pp. 241–248, 2003.

[138] L. Luan *et al.*, "Ultraflexible nanoelectronic probes form reliable , glial scar – free neural integration," *Sci. Adv.*, vol. 3, no. e1601966, pp. 1–10, 2017.

[139] C. Van Riesen, G. Tsironis, D. Gruber, and F. Klostermann, "Disease-specific longevity of impulse generators in deep brain stimulation and review of the literature," *J. Neural Transm.*, vol. 123, no. 6, pp. 621–630, 2016.

[140] X. Li, W. A. Serdijn, W. Zheng, Y. Tian, and B. Zhang, "The injectable neurostimulator : an emerging therapeutic device," *Trends Biotechnol.*, vol. 33, no. 7, pp. 388–394, 2015.

[141] T. J. Foutz, D. M. Ackermann, K. L. Kilgore, and C. C. McIntyre, "Energy Efficient Neural Stimulation: Coupling Circuit Design and Membrane Biophysics," *PLoS One*, vol. 7, no. 12, 2012.

[142] S. F. Cogan, "Neural stimulation and recording electrodes.," *Annu. Rev. Biomed. Eng.*, vol. 10, pp. 275–309, 2008.

[143] S. Negi, R. Bhandari, and F. Solzbacher, "Morphology and Electrochemical Properties of Activated and Sputtered Iridium Oxide Films for Functional Electrostimulation *," *J. Sens. Technol.*, vol. 2, no. September, pp. 138–147, 2012.

[144] S. Venkatraman *et al.*, "In Vitro and In Vivo Evaluation of PEDOT Microelectrodes for Neural Stimulation and Recording," *IEEE Trans. Neural Syst. Rehabil. Eng.*, vol. 19, no. 3, pp. 307–316, 2011.

[145] X. T. Cui and D. D. Zhou, "Poly (3,4-Ethylenedioxythiophene) for Chronic Neural Stimulation," *IEEE Trans. Neural Syst. Rehabil. Eng.*, vol. 15, no. December, pp. 502–508, 2007.

[146] C. De Haro, R. Mas, G. Abadal, J. Muñoz, F. Perez-Murano, and C. Domínguez, "Electrochemical platinum coatings for improving performance of implantable microelectrode arrays," *Biomaterials*, vol. 23, no. 23, pp. 4515–4521, 2002.

[147] S. Yamagiwa, A. Fujishiro, H. Sawahata, and R. Numano, "Chemical for low-voltage microscale electrode neurostimulation," *Sensors Actuators B. Chem.*, vol. 206, pp. 205–211, 2015.

[148] C. Boehler, T. Stieglitz, and M. Asplund, "Nanostructured platinum grass enables superior impedance reduction for neural microelectrodes," *Biomaterials*, vol. 67, pp. 346–353, 2015.

[149] X. F. Wei and W. M. Grill, "Analysis of high-perimeter planar electrodes for efficient neural stimulation.," *Front. Neuroeng.*, vol. 2, no. November, p. 15, 2009.

[150] B. Howell and W. M. Grill, "Evaluation of high-perimeter electrode designs for deep brain stimulation," *J. Neural Eng.*, vol. 11, no. 4, p. 46026, 2014.

[151] C. R. Butson, I. O. Miller, R. A. Normann, B. Howell, B. Huynh, and W. M. Grill, "Role of electrode design on the volume of tissue activated during deep brain stimulation," *J. Neural Eng.*, vol. 3, pp. 1–8, 2006.

[152] A. K. Ahuja, M. R. Behrend, J. J. Whalen, M. S. Humayun, and J. D. Weiland, "The dependence of spectral impedance on disc microelectrode radius," *IEEE Trans. Biomed. Eng.*, vol. 55, no. 4, pp. 1457–1460, 2008.

[153] W. M. Grill and X. F. Wei, "High efficiency electrodes for deep brain stimulation," *Eng. Med. Biol. Soc. 2009. EMBC 2009. Annu. Int. Conf. IEEE*, pp. 3298–3301, 2009.

[154] S. F. Cogan, J. Ehrlich, and T. D. Plante, "The effect of electrode geometry on electrochemical properties measured in saline," *Conf. Proc. ... Annu. Int. Conf. IEEE Eng. Med. Biol. Soc. IEEE Eng. Med. Biol. Soc. Annu. Conf.*, vol. 2014, pp. 6850–6853, 2014.

[155] C. Puente-Baliarda, J. Romeu, R. Pous, and A. Cardama, "On the behavior of the sierpinski multiband fractal antenna," *IEEE Trans. Antennas Propag.*, vol. 46, no. 4, pp. 517–524, 1998.

[156] C. Puente-Baliarda, J. Romeu, R.Pous, J. Ramis, and A. Hijazo, "Small but long Koch fractal monopole," *Electron. Lett.*, vol. 34, no. I, pp. 9–10, 1998.

[157] S. R. Best, "On the significance of self-similar fractal geometry in determining the multiband behavior of the sierpinski gasket antenna," *IEEE Antennas Wirel. Propag. Lett.*, vol. 1, pp. 22–25, 2002.

[158] S. Fuqi, G. Hongming, and G. Baoxin, “Analysis of a Vicsek Fractal Patch Antenna,” *4th Int. Conf. Microw. Millim. Wave Technol. Proc.*, pp. 98–101, 2004.

[159] L. Golestanirad, C. Pollo, and S. J. Graham, “Analysis of fractal electrodes for efficient neural stimulation,” *Front. Neuroeng.*, vol. 6, no. July, pp. 791–794, 2013.

[160] W. J. Watterson, R. D. Montgomery, and R. P. Taylor, “Fractal Electrodes as a Generic Interface for Stimulating Neurons,” *Publ.*, no. June, pp. 1–9, 2017.

[161] V. Tz. Krasteva and S. P. Pazov, “Estimation of current density distribution under electrodes for external defibrillation,” *Biomed. Eng. Online*, vol. 16, no. December, 2002.

[162] J. T. Rubinstein, F. A. Spelman, M. Soma, and M. F. Suesserman, “Current Density Profiles of Surface Mounted and Recessed Electrodes for Neural Prostheses,” *IEEE Trans. Biomed. Eng.*, vol. BME-34, no. 11, pp. 864–875, 1987.

[163] S. Xu *et al.*, “Stretchable batteries with self-similar serpentine interconnects and integrated wireless recharging systems,” *Nat. Commun.*, vol. 4, p. 1543, 2013.

[164] P. K. Yang *et al.*, “A Flexible, Stretchable and Shape-Adaptive Approach for Versatile Energy Conversion and Self-Powered Biomedical Monitoring,” *Adv. Mater.*, vol. 27, no. 25, pp. 3817–3824, 2015.

[165] J. a Fan *et al.*, “Fractal design concepts for stretchable electronics.,” *Nat. Commun.*, vol. 5, p. 3266, 2014.

[166] I. Vlassiouk, P. Takmakov, and S. Smirnov, “Sensing DNA hybridization via ionic conductance through a nanoporous electrode,” *Langmuir*, vol. 21, no. 11, pp. 4776–4778, 2005.

[167] C. Amatore and I. Svir, “A new and powerful approach for simulation of diffusion at microelectrodes based on overlapping sub-domains: Application to chronoamperometry at the microdisk,” *J. Electroanal. Chem.*, vol. 557, pp. 75–90, 2003.

[168] A. Lavacchi, U. Bardi, C. Borri, S. Caporali, A. Fossati, and I. Perissi, “Cyclic voltammetry simulation at microelectrode arrays with COMSOL Multiphysics,” *J. Appl. Electrochem.*, vol. 39, no. 11, pp. 2159–2163, 2009.

[169] N. Godino, X. Borrise, F. X. Muñoz, F. J. Del Campo, and R. G. Compton, “Mass transport to nanoelectrode arrays and limitations of the diffusion domain approach: theory and experiment,” *J. Phys. Chem. C*, vol. 113, no. 25, pp. 11119–11125, 2009.

[170] W. M. Grill and X. F. Wei, “High Efficiency Electrodes for Deep Brain Stimulation,” *Conf Proc IEEE Eng Med Biol Soc.*, 2013.

[171] R. Caldwell *et al.*, “Neural electrode resilience against dielectric damage may be improved by use of highly doped silicon as a conductive material,” *J. Neurosci. Methods*, vol. 293, pp. 210–225, 2018.

[172] S. F. Cogan, T. D. Plante, and J. Ehrlich, “Sputtered iridium oxide films (SIROFs) for low-impedance neural stimulation and recording electrodes,” *26th Annu. Int. Conf. IEEE Eng. Med. Biol. Soc.*, vol. 4, pp. 4153–4156, 2004.

[173] S. Zeitler, E. Wendler-Kalsch, W. Preidel, and V. Tegeder, “Corrosion of platinum electrodes in phosphate buffered saline solution,” *Mater. Corros. und Korrosion*, vol. 48, no. 5, pp. 303–310, 1997.

[174] D. B. Hibbert, K. Weitzner, B. Tabor, and P. Carter, “Mass changes and dissolution of platinum during electrical stimulation in artificial perilymph solution.,” *Biomaterials*, vol. 21, no. 21, pp. 2177–2182, 2000.

[175] D. Kumsa *et al.*, “Electrical neurostimulation with imbalanced waveform mitigates dissolution of platinum electrodes,” *J. Neural Eng.*, vol. 13, no. 5, p. 054001, 2016.

[176] J. S. Lockard, W. C. Congdon, and L. L. DuCharme, “Feasibility and Safety of Vagal Stimulation In Monkey Model,” *Epilepsia*, vol. 31, pp. S20–S26, 1990.

[177] S. Tesfaye, J. Watt, S. J. Benbow, K. A. Pang, J. Miles, and I. A. MacFarlane, “Electrical spinal-cord stimulation for painful diabetic peripheral neuropathy,” *Lancet*, vol. 348, no. 9043, pp. 1698–1701, 1996.

[178] C. Haberler *et al.*, “No tissue damage by chronic deep brain stimulation in Parkinson’s disease,” *Ann. Neurol.*, vol. 48, no. 3, pp. 372–376, 2000.

[179] H. S. Mayberg *et al.*, “Deep Brain Stimulation for Treatment-Resistant Depression,” *Neuron*, vol. 45, no. 5, pp. 651–660, 2005.

[180] J. M. Huston *et al.*, “Transcutaneous vagus nerve stimulation reduces serum high mobility group box 1 levels and improves survival in murine sepsis,” *Crit. Care Med.*, vol. 35, no. 12, pp. 2762–2768, 2007.

[181] R. Fuentes, P. Petersson, W. B. Siesser, M. G. Caron, and M. A. L. Nicolelis, “Spinal Cord Stimulation Restores Locomotion in Animal Models of Parkinson ’ s Disease,” *Science (80-.).*, vol. 323, no. 2009, pp. 1578–1582, 2009.

[182] P. E. K. Donaldson, N. d. N. Donaldson, and G. S. Brindley, “Life of Pt and Pt-Ir stimulating electrodes in neurological prostheses,” *Med. Biol. Eng. Comput.*, vol. 23, pp. 84–86, 1985.

[183] G. Benke and W. Gnot, “The electrochemical dissolution of platinum,” *Hydrometallurgy*, vol. 64, no. 3, pp. 205–218, 2002.

[184] A. Gencoglu and A. Minerick, “Chemical and morphological changes on platinum microelectrode surfaces in AC and DC fields with biological buffer solutions.,” *Lab Chip*, vol. 9, no. 13, pp. 1866–1873, 2009.

[185] C. De Haro, R. Mas, G. Abadal, J. Muñoz, F. Perez-Murano, and C. Domínguez, "Electrochemical platinum coatings for improving performance of implantable microelectrode arrays," *Biomaterials*, vol. 23, no. 23, pp. 4515–4521, 2002.

[186] V. S. Polikov, P. A. Tresco, and W. M. Reichert, "Response of brain tissue to chronically implanted neural electrodes," *J. Neurosci. Methods*, vol. 148, no. 1, pp. 1–18, 2005.

[187] K. M. Kovach *et al.*, "High-throughput in vitro assay to evaluate the cytotoxicity of liberated platinum compounds for stimulating neural electrodes," *J. Neurosci. Methods*, vol. 273, pp. 1–9, 2016.

[188] K. Wissel *et al.*, "Platinum corrosion products from electrode contacts of human cochlear implants induce cell death in cell culture models," *PLoS One*, vol. 13, no. 5, p. e0196649, 2018.

[189] L. Xu *et al.*, "Materials and fractal designs for 3D multifunctional integumentary membranes with capabilities in cardiac electrotherapy," *Adv. Mater.*, vol. 27, no. 10, pp. 1731–1737, 2015.

[190] W. J. Watterson, R. D. Montgomery, and R. P. Taylor, "Fractal Electrodes as a Generic Interface for Stimulating Neurons," *Sci. Rep.*, vol. 7, no. June, pp. 1–9, 2017.

[191] H. Park, P. Takmakov, and H. Lee, "Electrochemical Evaluations of Fractal Microelectrodes for Energy Efficient Neurostimulation," *Sci. Rep.*, vol. 8, no. 4375, pp. 1–11, 2018.

[192] Group GBD 2015 Neurological Disorders Collaborator, "Global, regional, and national burden of neurological disorders during 1990-2015: a systematic analysis for the Global Burden of Disease Study 2015," *Lancet Neurol.*, vol. 16, pp. 877–97, 2017.

[193] A. MJ, T. VC, and K. RB, "Honeycomb carbon: a review of graphene," *Chem Rev*, vol. 110, pp. 132–145, 2010.

[194] F. Torrisi *et al.*, "Inkjet-printed graphene electronics," *ACS Nano*, vol. 6, no. 4, pp. 2992–3006, 2012.

[195] H. Chen, M. B. Müller, K. J. Gilmore, G. G. Wallace, and D. Li, "Mechanically strong, electrically conductive, and biocompatible graphene paper," *Adv. Mater.*, vol. 20, no. 18, pp. 3557–3561, 2008.

[196] A. Deji, T. L, Y. Q, L. X, P. P, and K. D, "Large-Area Graphene Electrodes: Using CVD to facilitate applications in commercial touchscreens, flexible nanoelectronics, and neural interfaces," *IEEE Nanotechnol. Mag.*, vol. 9, no. July, pp. 6–14, 2015.

[197] M. A. Brown, L. Barker, L. Semprini, and E. D. Minot, "Graphene biotransistor interfaced with a nitrifying biofilm," *Environ. Sci. Technol. Lett.*, vol. 2, no. 4, pp. 118–122, 2015.

[198] S. R. Shin *et al.*, "Graphene-based materials for tissue engineering," *Adv. Drug Deliv. Rev.*, vol. 105, pp. 255–274, 2016.

[199] N. Liu *et al.*, "Ultratransparent and stretchable graphene electrodes," *Sci. Adv.*, vol. 3, no. September, p. e1700159, 2017.

[200] H. Ya-Ping *et al.*, "Complete corrosion inhibition through graphene defect passivation," *ACS Nano*, vol. 8, no. 1, p. 443, 2014.

[201] N. T. Kirkland, T. Schiller, N. Medhekar, and N. Birbilis, "Exploring graphene as a corrosion protection barrier," *Corros. Sci.*, vol. 56, pp. 1–4, 2012.

[202] D. Prasai, J. C. Tuberquia, R. R. Harl, G. K. Jennings, and K. I. Bolotin, "Graphene: Corrosion-Inhibiting Coating," *ACS Nano*, vol. 6, no. 2, pp. 1102–1108, 2012.

[203] W. Zhang *et al.*, "Use of graphene as protection film in biological environments," *Sci. Rep.*, vol. 4, pp. 1–8, 2014.

[204] A. J. Stapleton, C. J. Shearer, C. T. Gibson, A. D. Slattery, and J. G. Shapter, "Accurate thickness measurement of graphene," *Nanotechnology*, vol. 27, no. 12, p. 125704, 2016.

[205] S. B. Brummer and M. J. Turner, "Electrical Stimulation with Pt Electrodes: II–Estimation of Maximum Surface Redox (Theoretical Non-Gassing) Limits," *IEEE Trans. Biomed. Eng.*, vol. BME-24, no. 5, pp. 440–443, 1977.

[206] A. K. Ahuja and M. R. Behrend, "The Argus^{TM} II retinal prosthesis: Factors affecting patient selection for implantation," *Prog. Retin. Eye Res.*, vol. 36, pp. 1–23, 2013.

[207] F. Zhou, Z. Li, G. J. Shenoy, L. Li, and H. Liu, "Enhanced room-temperature corrosion of copper in the presence of graphene," *ACS Nano*, vol. 7, no. 8, pp. 6939–6947, 2013.

[208] M. Schriver, W. Regan, W. J. Gannett, A. M. Zaniewski, M. F. Crommie, and A. Zettl, "Graphene as a long-term metal oxidation barrier: worse than nothing.," *ACS Nano*, vol. 7, no. 7, pp. 5763–8, 2013.

[209] R. S. Weatherup *et al.*, "Long-Term Passivation of Strongly Interacting Metals with Single-Layer Graphene," *J. Am. Chem. Soc.*, vol. 137, no. 45, pp. 14358–14366, 2015.

[210] C. Cui, A. T. O. Lim, and J. Huang, "A cautionary note on graphene anti-corrosion coatings," *Nat. Nanotechnol.*, vol. 12, no. 9, pp. 834–835, 2017.

[211] X. Feng, S. Maier, and M. Salmeron, "Water Splits Epitaxial Graphene and Intercalates," *J. Am. Chem. Soc.*, vol. 134, pp. 5662–5668, 2012.

[212] P. Sutter, J. T. Sadowski, and E. A. Sutter, "Chemistry under Cover : Tuning Metal - Graphene Interaction by Reactive Intercalation," *J. Am. Chem. Soc.*, vol. 132, pp. 8175–8179, 2010.

[213] R. Mu *et al.*, "Visualizing chemical reactions confined under graphene," *Angew. Chemie - Int. Ed.*, vol. 51, pp. 4856–4859, 2012.

[214] J. Wintterlin and M. L. Bocquet, "Graphene on metal surfaces," *Surf. Sci.*, vol. 603, pp. 1841–1852, 2009.

[215] M. Batzill, "The surface science of graphene: Metal interfaces, CVD synthesis, nanoribbons, chemical modifications, and defects," *Surf. Sci. Rep.*, vol. 67, pp. 83–115, 2012.

[216] Y. Yao *et al.*, "Graphene cover-promoted metal-catalyzed reactions," *Proc. Natl. Acad. Sci.*, vol. 111, no. 48, pp. 17023–17028, 2014.

[217] J. Knoch, Z. Chen, and J. Appenzeller, "Properties of Metal – Graphene Contacts," *IEEE Trans. Nanotechnol.*, vol. 11, no. 3, pp. 513–519, 2012.

[218] F. B. Diniz *et al.*, "Impedimetric evaluation for diagnosis of Chagas' disease: Antigen-antibody interactions on metallic eletrodes," *Biosens. Bioelectron.*, vol. 19, no. 2, pp. 79–84, 2003.

[219] M. A. Macdonald and H. A. Andreas, "Method for equivalent circuit determination for electrochemical impedance spectroscopy data of protein adsorption on solid surfaces," *Electrochim. Acta*, vol. 129, pp. 290–299, 2014.

[220] A. Héduit, I. Quinio, D. Stadmuller, D. R. Thévenot, A. Héduit, and D. R. Thévenot, "Modified platinum electrodes : electrochemical characteristics and behaviour in activated sludge," *Water Sci. Technol.*, vol. 34, no. 3–4, pp. 143–150, 1996.

[221] C. Parra *et al.*, "A nanomolecular approach to decrease adhesion of biofouling‐producing bacteria to graphene‐coated material," *J. Nanobiotechnology*, vol. 13, no. 82, pp. 1–10, 2015.

[222] R. Li, Z. Wu, Y. Wangb, L. Ding, and Y. Wang, "Role of pH-induced structural change in protein aggregation in foam fractionation of bovine serum albumin," *Biotechnol. Reports*, vol. 9, pp. 46–52, 2016.